



2  
2001



This is to certify that the

dissertation entitled

ANGLE RESOLVED PHOTOEMISSION STUDIES  
OF TRANSITION METAL DICHALCOGENIDES

presented by

WAYNE C. TONJES

has been accepted towards fulfillment  
of the requirements for

PH. D. degree in PHYSICS

A handwritten signature in cursive script, appearing to read "R. Liu".

Major professor  
R. Liu

Date 06/12/01

**PLACE IN RETURN BOX** to remove this checkout from your record.  
**TO AVOID FINES** return on or before date due.  
**MAY BE RECALLED** with earlier due date if requested.

DATE DUE	DATE DUE	DATE DUE

**ANGLE RESOLVED PHOTOEMISSION STUDIES OF  
TRANSITION METAL DICHALCOGENIDES**

**By**

**Wayne C. Tonjes**

**A DISSERTATION**

**Submitted to  
Michigan State University  
in partial fulfillment requirements  
for the degree of**

**DOCTOR OF PHILOSOPHY**

**Department of Physics and Astronomy**

**2001**

## ABSTRACT

### Angle Resolved Photoemission Studies of Transition Metal Dichalcogenides

By

Wayne C. Tonjes

High resolution angle resolved photoelectron spectroscopy was used to study the electronic structures of several transition metal dichalcogenides. These materials are of interest as quasi-two-dimensional layered materials which undergo charge density wave (CDW) phase transitions. Five specific transition metal dichalcogenides were studied: 2H-TaSe<sub>2</sub>, 2H-TaS<sub>2</sub>, 2H-NbSe<sub>2</sub>, 1T-TaS<sub>2</sub>, and 1T-TiSe<sub>2</sub>. The band dispersions and Fermi surfaces of each material were investigated. Results were compared to those of band structure calculations. Comparing spectra taken in the high temperature states and the lower temperature CDW state, information about the CDW energy gaps and the CDW mechanisms were obtained.

For the 2H polytype materials, the normal state electronic structures have the same basic characteristics. Their Fermi surface consists of a pocket around  $\Gamma$  and another one around K. They all exhibit a saddle band near  $E_F$  along  $\Gamma$ -K. In the CDW phases, a finite energy gap is observed in the saddle band region and on the Fermi surface around K in 2H-TaS<sub>2</sub> and 2H-TaSe<sub>2</sub>. Gapping on the Fermi surface around  $\Gamma$  is not observed. Thus, the charge density waves in this family of materials originate from a combination of the partial nesting of the Fermi surface around K and the saddle band.

For 1T-TaS<sub>2</sub>, a Fermi surface was observed in the quasi-commensurate CDW phase. In addition to the pockets around the M points as predicted by earlier non-relativistic non-self-consistent band structure calculations for the normal state, a small electron pocket around  $\Gamma$  was observed. The latter pocket is consistent with results of recent self-consistent band structure calculations including spin-orbit interaction. In the commensurate CDW phase, a  $k$ -independent energy gap of approximately 120 meV magnitude opens at the Fermi level as a result of a CDW-induced Mott transition.

1T-TiSe<sub>2</sub> shows significant three-dimensional electronic structure despite its layered morphology. It also shows interesting photoelectron spectroscopy effects, such as emission from thermally populated states above the Fermi level. The CDW formation seems to result from coupling of hole and electron states in an excitonic insulator transition.

**Copyright by**

**Wayne C. Tonjes**

**2001**

## **ACKNOWLEDGEMENTS**

Thanks are given to Dr. C. G. Olson and Dr. S. D. Mahanti for helpful discussions. This work was partially supported by the Center for Fundamental Materials Research, Michigan State University, and by the NSF under Award No. DMR-9801776. This work is based upon research conducted at the Synchrotron Radiation Center, University of Wisconsin-Madison, which is supported by the NSF under Award No. DMR-95-31009. Ames Laboratory was operated for the U. S. DOE by Iowa State University under Contract No. W-7405-ENG-82. Support of the Natural Sciences and Engineering Research Council of Canada is also acknowledged.

## Table of Contents

List of Tables .....	ix
List of Figures .....	x
Abbreviations .....	xv
Chapter 1 Introduction .....	1
Chapter 2 Angle Resolved Photoelectron Spectroscopy .....	3
2.1 Photoemission Process .....	3
2.1.1 Photoexcitation .....	4
2.1.2 Transport to the Surface .....	5
2.1.3 Escape From the Crystal .....	6
2.2 Energy Distribution Curves .....	7
2.3 Angle Resolved Photoemission .....	10
2.3.1 Momentum Relations .....	10
2.3.2 Band Mapping .....	13
2.3.3 Fermi Surface Mapping .....	13
2.3.4 Measurement of the Energy Gap .....	14
Chapter 3 Charge Density Waves .....	15
3.1 Electronic Susceptibility and Fermi Surface Nesting .....	15
3.2 The Energy Gap and the Kohn Anomaly .....	17
3.3 Other Physical Properties Related to CDW .....	20
3.3.1 Resistivity .....	21
3.3.2 Magnetic Susceptibility .....	21
3.3.3 Hall Coefficient .....	21
3.3.4 Seebeck Coefficient .....	22
Chapter 4 Transition-Metal Dichalcogenides .....	23

4.1 Structure.....	23
4.2 Electronic Structures .....	24
4.2.1 2H-TaSe <sub>2</sub> , 2H-TaS <sub>2</sub> , and 2H-NbSe <sub>2</sub> .....	25
4.2.2 1T-TaS <sub>2</sub> .....	27
4.2.3 1T-TiSe <sub>2</sub> .....	29
4.3 Charge Density Wave Transitions.....	30
4.3.1 2H-TaSe <sub>2</sub> , 2H-TaS <sub>2</sub> , and 2H-NbSe <sub>2</sub> .....	31
4.3.1.1 Resistivity .....	33
4.3.1.2 Magnetic Susceptibility .....	35
4.3.1.3 Hall and Seebeck Coefficients.....	36
4.3.2 1T-TaS <sub>2</sub> .....	38
4.3.2.1 Resistivity .....	39
4.3.2.2 Magnetic Susceptibility.....	40
4.3.2.3 Hall and Seebeck Coefficients.....	41
4.3.3 1T-TiSe <sub>2</sub> .....	42
4.3.3.1 Resistivity .....	43
4.3.3.2 Magnetic Susceptibility.....	44
4.3.3.3 Hall and Seebeck Coefficients.....	44
Chapter 5     Experimental Details.....	46
5.1 Sample Preparation.....	46
5.2 Photon Source .....	48
5.3 Electron Energy Analyzer.....	50
Chapter 6     2H-TaSe <sub>2</sub> , 2H-TaS <sub>2</sub> , and 2H-NbSe <sub>2</sub> .....	52
6.1 Band Dispersions and the Saddle Band .....	53
6.1.1 2H-TaSe <sub>2</sub> .....	53
6.1.2 2H-TaS <sub>2</sub> .....	56
6.1.3 2H-NbSe <sub>2</sub> .....	56
6.2 Fermi Surfaces .....	58

6.2.1 2H-TaSe <sub>2</sub> .....	58
6.2.2 2H-TaS <sub>2</sub> .....	61
6.2.3 2H-NbSe <sub>2</sub> .....	62
6.3 Energy Gap in the CDW State .....	63
6.3.1 2H-TaSe <sub>2</sub> .....	63
6.3.2 2H-TaS <sub>2</sub> .....	68
6.3.3 2H-NbSe <sub>2</sub> .....	70
6.4 Summary and Discussion.....	70
Chapter 7 1T-TaS <sub>2</sub> .....	74
7.1 Band Dispersions.....	74
7.2 Fermi Surfaces .....	79
7.3 Energy Gap in the Commensurate CDW State .....	81
7.4 Summary and Discussion.....	83
Chapter 8 1T-TiSe <sub>2</sub> .....	86
8.1 Band Dispersions.....	86
8.2 Fermi Surfaces .....	89
8.3 Energy Gap in the CDW State .....	93
8.4 Summary .....	96
Chapter 9 Summary .....	97
References .....	100

## List of Tables

Table 4-1 .....	31
-----------------	----

## List of Figures

Figure 2-1: In the photoexcitation process an electron in some initial state $i$ below the Fermi level is excited to some final state $f$ above it. In the process, energy and momentum are conserved. $E_K$ is the measurable kinetic energy of the excited electron after it escapes through the work function $e\phi$ of the material into vacuum. ....	5
Figure 2-2: The universal curve for the scattering length of electrons as a function of kinetic energy. The data are taken from numerous materials. At kinetic energies of interest to a photoemission experiment, the escape depth is of the order of $10 \text{ \AA}$ . ....	6
Figure 2-3: A sample EDC from an angle resolved experiment.....	7
Figure 2-4: The parallel component of the electron wavevector $k_f$ is conserved as it passes from the material into vacuum with momentum $K$ . By measuring $\Theta$ , the parallel components of $K$ and $k_f$ can be determined. ....	10
Figure 2-5: The energy levels of a free electron material. The inner potential $V_0$ is simply the distance from the minimum of the free electron parabola to the vacuum level.....	12
Figure 3-1: The electronic band structure opens a gap, $\Delta$ , when the material goes from a) the normal state to b) the CDW state. The solid and dashed vertical lines define the normal state and PLD Brillouin zone respectively. ....	15
Figure 3-2: Examples of Fermi nesting for a) one-dimensional free electrons, b) arbitrary two-dimensional material and c) closed, two-dimensional cylinder. In a) and b), the nesting is perfect, but c) shows very imperfect nesting. ....	17
Figure 3-3: Electronic susceptibility for a free electron gas normalized to the undisturbed system as a function of disturbance wavevector $q$ . Depending on the dimensionality of the material, a disturbance of $Q=2k_F$ can create a singularity, a sharp step or a weak shoulder. ....	18
Figure 3-4: The temperature dependence of the CDW gap in the weak coupling limit. ..	19
Figure 3-5: Longitudinal acoustic phonon dispersion relation of a one-dimensional metal at various temperatures above the mean field transition temperature $T_0$ .....	20
Figure 4-1: Basic TMD sandwich structures of a) octahedral and b) trigonal prismatic coordination. The octahedral has the two chalcogen layers offset by $1/2a_0$ , while the trigonal prismatic has them aligned. ....	23
Figure 4-2: The unit cells of polytypes a) 2H and b) 1T. The stacking arrangement of the chalcogen-metal-chalcogen sandwiches and relative orientation are shown. ....	24

Figure 4-3: The hexagonal Brillouin zone in a) two- and b) three-dimensions.....	25
Figure 4-4: Band calculations for a) 2H-NbSe <sub>2</sub> , b) 2H-TaS <sub>2</sub> , and c) 2H-TaSe <sub>2</sub> from Wexler and Woolley <sup>14</sup> .....	26
Figure 4-5: Fermi surfaces of a) 2H-TaSe <sub>2</sub> , b) 2H-TaS <sub>2</sub> , and c) 2H-NbSe <sub>2</sub> . Curves A and B are at equivalent height in the conventional zone. The middle, unlabeled curve is at the top of zone. ....	26
Figure 4-6: Fermi surface of 1T-TaS <sub>2</sub> extrapolated from calculations without relativistic spin orbit corrections.....	27
Figure 4-7: 1T-TaS <sub>2</sub> band calculations a) with and b) without relativistic spin orbit corrections along the $\Gamma M$ and $\Gamma K$ symmetry lines. ....	28
Figure 4-8: 1T-TiSe <sub>2</sub> band calculation by Benesh et. al. <sup>23</sup> with valence bands and the top most core levels.....	29
Figure 4-9: Schematic Fermi surface of 1T-TiSe <sub>2</sub> based on carrier concentrations and the measured CDW wavevector by Wilson <sup>24</sup> .....	30
Figure 4-10: The 3 x 3 superlattice effect on a) the real space cell and b) the reciprocal space Brillouin zone. The lattice change generates three inequivalent atomic sites <i>a</i> , <i>b</i> , and <i>c</i> as labeled in ratios of 1::6::2. ....	32
Figure 4-11: Resistivity data parallel to the layers versus temperature for 2H polytypes a) 2H-TaSe <sub>2</sub> and 2H-TaS <sub>2</sub> from Di Salvo and Rice <sup>10</sup> (log plot) and b) 2H-NbSe <sub>2</sub> from Edwards and Frindt (log-log plot).....	33
Figure 4-12: The schematic Fermi surface Rice and Scott <sup>28</sup> used. The real system shows a Fermi surface similar to the thick solid curves shown in the lower right K region. The saddle point is the crossing of the dashed lines. ....	34
Figure 4-13: Magnetic susceptibility of 2H-TaSe <sub>2</sub> (squares), 2H-TaS <sub>2</sub> (triangles), and 2H-NbSe <sub>2</sub> (circles) normalized at T= 300K by Ayache et. al. <sup>29</sup> .....	35
Figure 4-14: The Hall coefficient versus temperature for a) 2H-TaSe <sub>2</sub> by Lee et. al. <sup>30</sup> and b) 2H-TaS <sub>2</sub> by Thompson et. al. <sup>31</sup> .....	36
Figure 4-15: The Hall coefficient versus temperature for 2H-NbSe <sub>2</sub> at 28.6 kG (empty squares) and 150 kG (solid squares) from Whitney et. al. <sup>32</sup> .....	37
Figure 4-16: Seebeck coefficient plotted against the log of temperature for two samples of 2H-NbSe <sub>2</sub> from Huntley and Frindt. ....	38
Figure 4-17: The $\sqrt{13} \times \sqrt{13}$ superlattice effects on a) the real space cell and b) the reciprocal space Brillouin zone of the CDW in 1T-TaS <sub>2</sub> . The reconstruction generates three inequivalent atomic sites <i>a</i> , <i>b</i> , and <i>c</i> in the ratios of 1::6::6.....	39

Figure 4-18: Parallel resistivity of 1T-TaS <sub>2</sub> from Manzke et. al. ....	40
Figure 4-19: Temperature dependence of the magnetic susceptibility for 1T-TaS <sub>2</sub> by Wilson et. al. ....	40
Figure 4-20: Hall coefficient versus temperature for 1T-TaS <sub>2</sub> by Mutka et. al. <sup>36</sup> The vertical scale above zero is 1000 times larger than the scale below zero to bring out details.....	41
Figure 4-21: The reciprocal space reconstruction caused by a 2x2x2 superlattice.....	42
Figure 4-22: Resistivity data for 1T-TiSe <sub>2</sub> by R. V. Coleman et. al.....	43
Figure 4-23: Magnetic susceptibility of 1T-TiSe <sub>2</sub> versus temperature, taken by Salvo et. al.....	44
Figure 4-24: Hall and Seebeck coefficient by Salvo et al. <sup>39</sup> . They both become negative as the CDW develops with temperature decrease. The Hall scale is on the left axis; the Seebeck coefficient on the right.....	45
Figure 5-1: Synchrotron Radiation Center electron storage ring Aladdin. Focussed light is emitted past the bending magnets and employed along beam lines. The beamlines are labeled by the type of monochromator used upon them. ....	49
Figure 5-2: ERG-Seya combined monochromators. The metal flat is a mirror inserted into the photon beam to select the Seya (top) over the ERG (bottom). ....	50
Figure 5-3: Hemispherical electron energy analyzer with focussing lenses. The inner and outer potential shells are set to specific voltages to allow only electrons with a desired energy to reach the electron multiplier to be pulse counted. The entrance aperture limits the accepted electrons to a small angle for angular resolution. ....	51
Figure 6-1: a) Normal state EDCs (solid lines) for the $\Gamma$ -K line of 2H-TaSe <sub>2</sub> with modeled fits (dashed curve). The tick marks indicate the peak positions. b) The extracted band dispersions from a). ....	54
Figure 6-2: Energy distribution curves (EDCs) in the normal state (T=125 K), for $k$ -points along two lines parallel to $\Gamma$ -K at a) $k_y = -0.07$ and b) $-0.15 \text{ \AA}^{-1}$ . The inset of the Brillouin zone's irreducible wedge (top) shows the amount of $k_z$ -dispersion of the Fermi surfaces predicted by band calculations <sup>14</sup> (A: $k_z = 0$ ; B: $k_z = 2\pi/c$ ; C: $k_z = \pi/c$ .) and the lines of a) and b).....	55
Figure 6-3: EDCs for 2H-NbSe <sub>2</sub> for $k$ -points a) along $\Gamma$ -K and b) along a line perpendicular to $\Gamma$ -K intersecting it at approximately the midpoint, as shown in the insets. c) and d) Band dispersions (symbols) determined by modeling the spectra in a) and b), respectively. ....	57

Figure 6-4: The Fermi surface cylinders (shaded and open circles) of 2H-TaSe <sub>2</sub> determined from the EDCs. The open triangle is the second wall seen along $\Gamma$ -K. Points <i>a</i> , <i>b</i> , and <i>c</i> are shown in Figure 6-10. Point <i>d</i> (diamond) was used for the temperature dependence of the gap shown in Figure 6-11. ....	59
Figure 6-5: Fermi level intensity map of 2H-TaSe <sub>2</sub> . Bright regions indicate greater intensity. The data between the dashed wedge were actually measured and symmetrized to give the rest of the Brillouin zone. ....	60
Figure 6-6: Fermi level intensity map of 2H-TaS <sub>2</sub> . The data were measured on one sixth of the Brillouin zone, rotated to give a comparable orientation to the other materials, and then symmetrized. ....	61
Figure 6-7: Fermi level intensity map of 2H-NbSe <sub>2</sub> . The arrow indicates a nesting vector of the same direction and magnitude as the CDW wavevector. ....	63
Figure 6-8: EDCs in the commensurate CDW state (T=20 K, solid curves) of 2H-TaSe <sub>2</sub> , for <i>k</i> -points along $\Gamma$ -K. The EDCs in the normal state are superimposed as dashed curves for comparison. ....	64
Figure 6-9: The energy shift vs. <i>k<sub>x</sub></i> along $\Gamma$ -K of 2H-TaSe <sub>2</sub> . The energy shift is taken as the binding energy difference of the leading edge midpoints in the normal and CDW state spectra. ....	65
Figure 6-10: EDCs for three FS crossing points of 2H-TaSe <sub>2</sub> , labeled as <i>a</i> , <i>b</i> , and <i>c</i> in Figure 6-4. The solid and dashed lines are spectra measured in the CDW (T=20 K) and normal (T=125 K) states respectively. ....	66
Figure 6-11: a) EDCs for point <i>d</i> in Figure 6-4 in the vicinity of the extended saddle band of 2H-TaSe <sub>2</sub> , measured at various temperatures. The normal state spectrum is superimposed on each curve as dashed lines for comparison. b) The energy shifts of the leading edge midpoint (solid squares) as a function of temperature. The solid line is the BCS relation. ....	68
Figure 6-12: a) EDCs for 2H-TaS <sub>2</sub> measured in the normal (T=80 K, dashed lines) and CDW (T=20 K, solid lines) states, along a line at approximately 36° with respect to $\Gamma$ -K, as shown (inset). Enlarged spectra at point A and B are reproduced in c) and b) respectively. ....	69
Figure 6-13: EDCs for 2H-NbSe <sub>2</sub> along $\Gamma$ -K measured in the normal (T=40 K, dashed lines) and CDW (T=13 K, solid lines) states. The bottom curve is for a <i>k</i> -point on the Fermi surface around $\Gamma$ while the other spectra are in the saddle band region. ....	71
Figure 7-1: EDCs of the QC-CDW (T= 250 K) state for the a) $\Gamma$ -M and b) $\Gamma$ -K lines of 1T-TaS <sub>2</sub> . The arrows indicate Fermi crossings. ....	75

Figure 7-2: Second derivative of the spectral intensity plotted versus energy and wavevector along a) $\Gamma$ -M and b) $\Gamma$ -K of 1T-TaS <sub>2</sub> . Darker regions indicate peak positions. ....	76
Figure 7-3: Band dispersions in the normal state from new band structure calculation, a) without, and b) and c) both with spin-orbit corrections included. Second derivatives of EDCs along $\Gamma$ -M and $\Gamma$ -K in the QC-CDW phase (see text for details) are also shown in c).....	78
Figure 7-4: Fermi level intensity maps of 1T-TaS <sub>2</sub> . The data between the dashed wedge were actually measured and symmetrized to give the rest of the Brillouin zone. Bright regions correspond to high intensity. ....	80
Figure 7-5: EDCs in the C-CDW state (T=20 K, solid curves), for the same set of $k$ -points along $\Gamma$ -M as in Figure 7-1 a). The EDCs in the QC-CDW state are superimposed as the dashed curves for comparison.....	82
Figure 8-1: Normal state EDCs for the projections along a) $\Gamma$ -M and b) $\Gamma$ -K lines of 1T-TiSe <sub>2</sub> . ....	87
Figure 8-2: EDCs along the normal emission directions of a) $\Gamma$ -A and b) M-L of 1T-TiSe <sub>2</sub> . The EDCs of a) are labeled with the $k_z$ ( $\text{\AA}^{-1}$ ) distance from $\Gamma$ . The EDCs of b) are labeled with their $(k_x, k_z)$ $\text{\AA}^{-1}$ values. ....	88
Figure 8-3: Fermi level intensity maps of 1T-TiSe <sub>2</sub> taken with 21eV photons. The data between the dashed lines were actually measured and rotated to give the rest of the Brillouin zone. ....	90
Figure 8-4: EDCs taken near apparent Fermi crossing in the normal state of 1T-TiSe <sub>2</sub> near a) the L point and b) midway between A and $\Gamma$ '. The $(k_x, k_z)$ points are in $\text{\AA}^{-1}$ .....	92
Figure 8-5: The temperature dependence in 1T-TiSe <sub>2</sub> of bands close in energy to the Fermi level near a) the L-M line and b) the A point. The normal state EDCs are shown in dashed lines and the CDW state in solid lines. ....	95

## Abbreviations

ARPES	Angle Resolved Photoelectron Spectroscopy
BCS	Bardeen-Cooper-Shriffer
BZ	Brillouin zone
CDW	Charge density wave
C-CDW	Commensurate charge density wave
DOS	Density of states
EDC	Energy distribution curve
EELS	Electron energy loss spectroscopy
ERG	Extended range grasshopper monochromator
FLAPW	Full-potential linearized augmented plane-wave
FS	Fermi surface
GGA	Generalized gradient approximation
I-CDW	Incommensurate charge density wave
LDA	Local density approximation
LEED	Low energy electron diffraction
PES	Photoelectron spectroscopy
PLD	Periodic lattice distortion
QC-CDW	Quasi-commensurate charge density wave
SRC	Synchrotron Radiation Center
STM	Scanning tunneling microscopy

T-CDW

Triclinic charge density wave

TMD

Transition metal dichalcogenide

## Chapter 1 Introduction

Quasi-low-dimensional materials have anisotropic structures that inhibit transport in one or two directions. They exhibit a rich variety of interesting physical phenomena. Many of them adopt new phases with lowered temperature such as superconductivity, periodic lattice distortions (PLDs), Peierls transitions that drive a metal to an insulating phase, and charge density waves (CDWs). One group of quasi-two-dimensional materials that has attracted tremendous attention in recent years is the high temperature superconducting cuprates, such as  $\text{YBa}_2\text{Cu}_3\text{O}_{7-\delta}$ <sup>1</sup>,  $\text{Bi}_2\text{Sr}_2\text{CaCu}_2\text{O}_{8+\delta}$ <sup>2</sup>, and  $\text{La}_2\text{-(Sr,Ba)}_x\text{CuO}_4$ <sup>3</sup>. Despite intense studies for more than ten years, high temperature superconductivity, though, is still not thoroughly understood. Another interesting group of quasi-two-dimensional materials is the transition metal dichalcogenides (TMDs), such as  $\text{TaSe}_2$  and  $\text{TaS}_2$ . A variety of CDWs have been observed in their various polytypes. Many aspects of CDWs are similar to those of superconductivity and they are not well understood either. The electronic structure near the Fermi energy plays an important role in the CDW formation. Therefore, understanding the electronic structure in these materials is important for understanding their CDW mechanisms.

Angle resolved photoelectron spectroscopy (ARPES) is a powerful tool for studying the electronic structure of solids. This technique is especially straightforward when applied to quasi-two-dimensional materials. Layered materials are also ideal for ARPES studies because they can be cleaved easily *in situ*. The cleavages occur between weakly bonded layers usually resulting in minimal surface disruptions.

This thesis describes high resolution ARPES studies of five TMDs. They are:  $2\text{H-TaSe}_2$ ,  $2\text{H-TaS}_2$ ,  $2\text{H-NbSe}_2$ ,  $1\text{T-TaS}_2$ , and  $1\text{T-TiSe}_2$ . The three 2H-polytype

compounds have very similar CDW properties. The transitions are weak and are of second order. 1T-TaS<sub>2</sub> has a very complicated CDW phase diagram. It undergoes a series of strong first order transitions when cooled. 1T-TiSe<sub>2</sub> exhibits yet another type of CDW with a single broad phase transition. In the ARPES experiments, band dispersions near the Fermi energy and the Fermi surfaces were investigated. The results are compared with band structure calculations. The CDW energy gaps were studied by comparing spectra taken in high and low temperature states. Important insights about the CDW mechanisms in these materials are obtained.

The thesis is organized as follows. Chapter 2 describes the ARPES technique in detail. Chapter 3 outlines the theory and properties of CDWs. Chapter 4 reviews the crystal structure, electronic structure and CDW properties of the five materials. Chapter 5 describes the specifics of the experimental system used in this work. Chapters 6, 7, and 8 present the ARPES results and discussions on the five materials. Chapter 9 concludes with a general summary.

## **Chapter 2 Angle Resolved Photoelectron Spectroscopy**

The photoelectric effect was first considered as an experimental tool by Einstein in 1905 in one of the three papers<sup>4</sup> that he published that revolutionized physics. In this paper, Einstein proposed the photon model of light that could be proven by quantitative measurements of the photoelectric effect. In 1914, R. A. Millikan performed such experiments and determined that the photoelectron effect had a frequency dependence, fully confirming Einstein's proposed photon model of light.

In the 1950s, it was found that the photoelectric effect could be used as a powerful tool to probe the electronic structure of matter through the simple relations of momentum and energy conservation. During the 1960s, this technique of photoelectron spectroscopy (PES) was used as a probe of the density of states (DOS) of materials. During the 1970s, the development of angular resolved electron energy analyzers allowed this technique to be used to map the energy bands in materials. With the refinement of these instruments and the development of synchrotron light sources, angle resolved photoelectron spectroscopy (ARPES) has become a key tool to understanding the electronic properties of solids.

### **2.1 Photoemission Process**

There are several explanations of photoemission, one being the one step model. It explains the photoemission in terms of an inverse low energy electron diffraction (LEED) process. Here we follow the three step model suggested by Berglund and Spicer<sup>5</sup>. Although this approach lacks rigor, it provides an intuitive phenomenological model. The three step model designates the three steps of the photoemission process as:

- 1) **Excitation:** An electron in some initial state absorbs a photon and is excited to a final state.
- 2) **Transport:** The photoexcited electron migrates to the surface of the material.
- 3) **Escape:** The photoexcited electron overcomes the work function of the material to escape.

Further details of the three steps are considered below.

### 2.1.1 Photoexcitation

In the photoexcitation process, both momentum and energy have to be conserved as shown in Figure 2-1. For a bound electron, the conservation of momentum is met by the crystal lattice, which can absorb or provide momentum to the electron in units of the reciprocal lattice vectors. The initial and final states are constrained to wavevectors related by:

$$\hbar\mathbf{k}_f = \hbar(\mathbf{k}_i + \mathbf{G}) \quad (2.1)$$

where  $\mathbf{k}_f$  and  $\mathbf{k}_i$  are the final and initial state wavevectors and  $\mathbf{G}$  is a reciprocal lattice vector. The photon momentum is negligible in comparison to the electron momenta. For a reduced Brillouin zone scheme, this means that only direct, vertical transitions of the electrons are of consideration.

The conservation of energy requires:

$$E_f = E_i + \hbar\omega \quad (2.2)$$

where  $E_i$  and  $E_f$  are the initial and final state energies respectively and  $\hbar\omega$  is the photon energy. The initial states must be occupied and the final states must be empty for photoemission to occur.

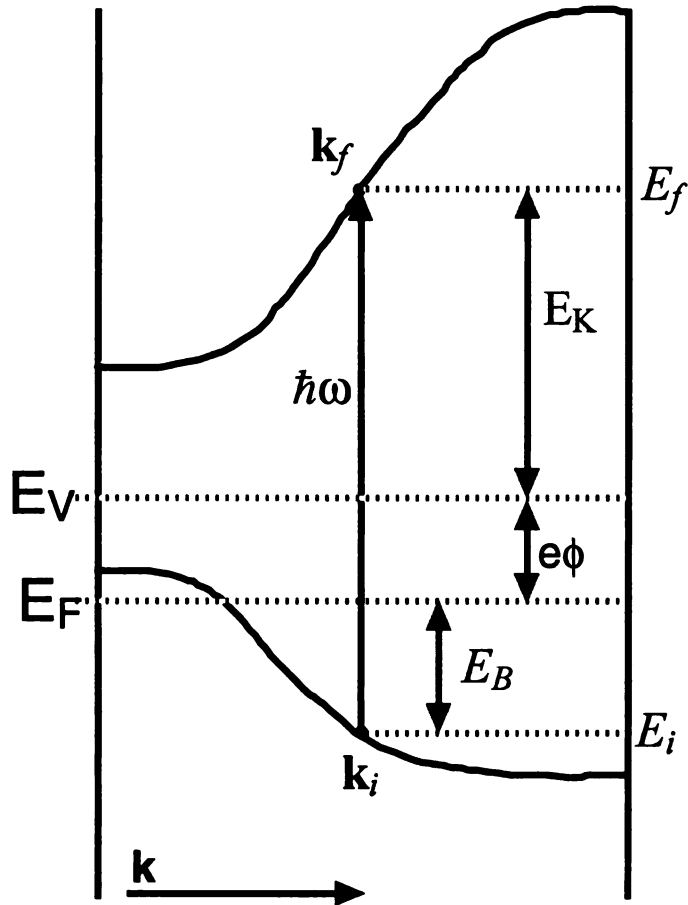


Figure 2-1: In the photoexcitation process an electron in some initial state  $i$  below the Fermi level is excited to some final state  $f$  above it. In the process, energy and momentum are conserved.  $E_K$  is the measurable kinetic energy of the excited electron after it escapes through the work function  $e\phi$  of the material into vacuum.

### 2.1.2 Transport to the Surface

As the excited electron migrates to the surface, it can be inelastically scattered by other electrons, phonons and plasmons. The mean free path between scattering events is nearly material independent as shown in Figure 2-2. For the kinetic energy range normally encountered in a photoemission experiment, the mean free path is in the range of 10-15Å. This makes the photoemission technique inherently surface sensitive. The inelastic scattering also introduces a smooth background of secondary electrons that adds to the primary electron signal.

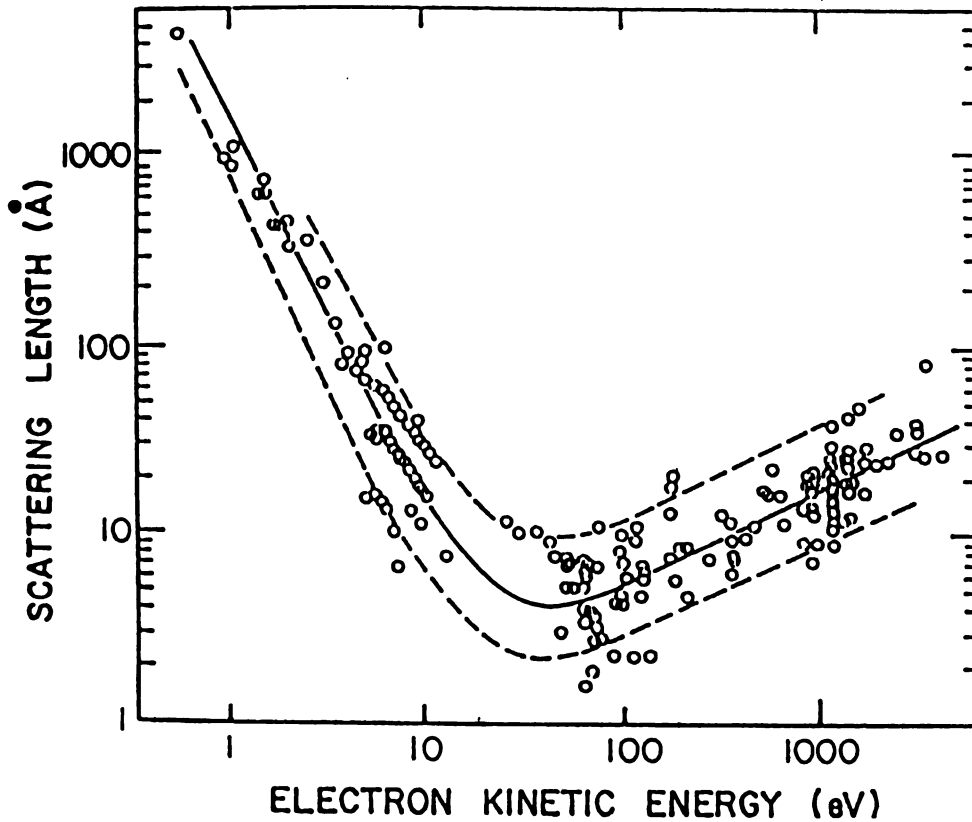


Figure 2-2: The universal curve for the scattering length of electrons as a function of kinetic energy<sup>6</sup>. The data are taken from numerous materials. At kinetic energies of interest to a photoemission experiment, the escape depth is of the order of 10 Å.

### 2.1.3 Escape From the Crystal

The excited electrons that reach the surface of the material have to overcome the work function to escape and be detected. Therefore, the measured kinetic energy of the photoelectron,  $E_K$ , is:

$$E_K = \hbar\omega - E_B - e\phi \quad (2.3)$$

where  $E_B$  is the binding energy of the initial state and  $e\phi$  is the work function of the material.

As the electron escapes the sample, its momentum changes. There is an effective refraction effect at the surface due to the work function. The normal component of the

electron's momentum is not conserved, whereas the parallel component is conserved. As a result, the electron's direction of travel is bent as it exits the material.

## 2.2 Energy Distribution Curves

In a photoemission experiment, the photoelectrons are collected and energy analyzed by an electron energy analyzer. By measuring the photoelectron yield as a function of  $E_K$  at fixed photon energy, one gets an energy distribution curve (EDC).

Figure 2-3 shows an example of an EDC. Usually, the kinetic energy is converted to binding energy, using (2.3).

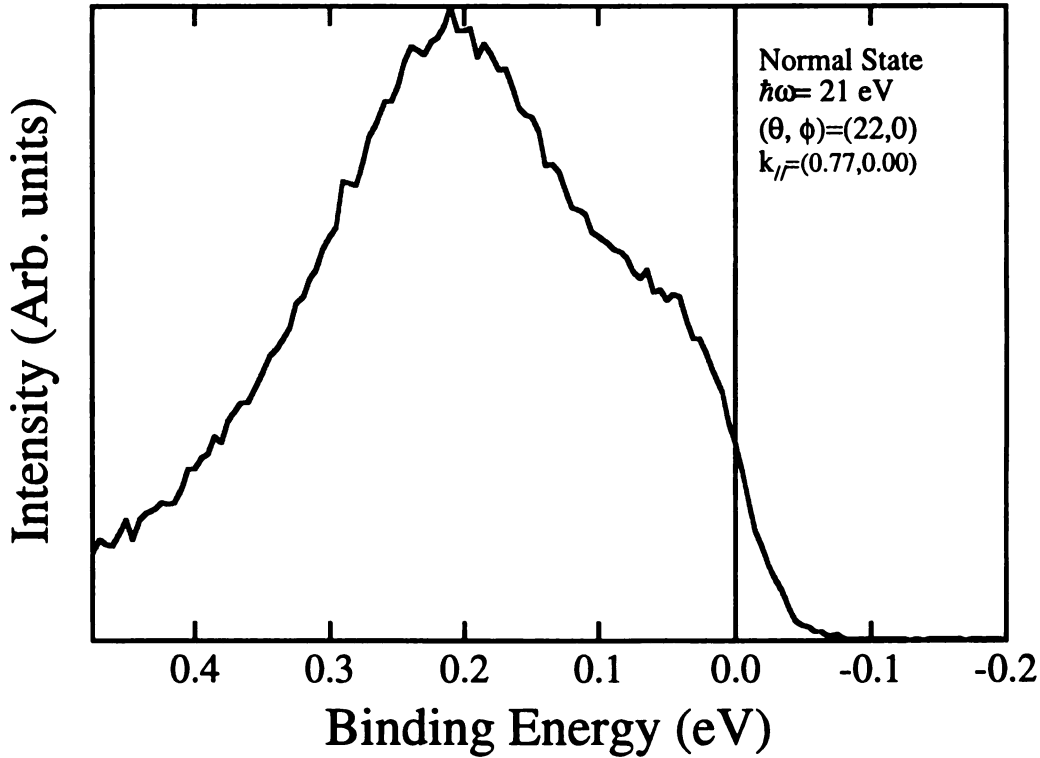


Figure 2-3: A sample EDC from an angle resolved experiment.

The incident photon and the electron interaction is governed by the Hamiltonian:

$$\mathbf{H} = \frac{\hbar}{2mc} (\mathbf{A} \cdot \mathbf{k} + \mathbf{k} \cdot \mathbf{A}) \quad (2.4)$$

where  $\mathbf{A}$  is the vector potential of the photon and  $\mathbf{k}$  is the momentum operator:

$$\mathbf{k} = -i\nabla \quad (2.5)$$

In the Coulomb gauge, the momentum operator acting upon the vector potential is zero. Since  $\mathbf{A}$  is discontinuous at the surface of the material, the second term of (2.4) leads to a specific surface photoelectric effect. It is usually ignored, as it does not contribute any sharp features to the photoemission spectrum. The transition probability of some electron being excited by this interaction is governed by the matrix element:

$$\begin{aligned} M_{fi} &= \langle f, \mathbf{k}_f | \mathbf{H} | i, \mathbf{k}_i \rangle \\ &= \langle f, \mathbf{k}_f | \frac{-i\hbar}{2mc} \mathbf{A} \cdot \nabla | i, \mathbf{k}_i \rangle \end{aligned} \quad (2.6)$$

where  $|i, \mathbf{k}_i\rangle$  and  $|f, \mathbf{k}_f\rangle$  are the initial and final state wavefunctions of the electron respectively. The photocurrent at a specific photon energy  $\hbar\omega$  is given by:

$$\sum_{f,i} |M_{fi}|^2 \delta(E_f - E_i - \hbar\omega) \delta(\mathbf{k}_i + \mathbf{G} - \mathbf{k}_f) \quad (2.7)$$

where the  $\delta$  functions ensure energy and momentum conservation.

The energy distribution curve that results from this photocurrent is given by:

$$\begin{aligned} N(E_K, \hbar\omega) &\propto \sum_{f,i} |M_{fi}|^2 \delta(E_f - E_i - \hbar\omega) \delta(\mathbf{k}_i + \mathbf{G} - \mathbf{k}_f) \\ &\quad \times d(E_f, \mathbf{k}_f) \theta(\mathbf{k}_{f\perp}) \\ &\quad \times T(E_f, \mathbf{K}_{\parallel}) \delta(E_K - E_f + e\phi) \delta(\mathbf{K}_{\parallel} - \mathbf{k}_{f\parallel}) \end{aligned} \quad (2.8)$$

where  $d$  is the transport coefficient and  $T$  is the transmission function of the surface. The terms are organized by row according to the process of the three step model which generates them with the energy and momentum constraints explicitly included as  $\delta$ -

functions and the  $\theta$  step-function. The transport coefficient  $d$  can be written as:

$$d(E_f, \mathbf{k}_f) = \frac{\alpha\lambda}{1 + \alpha\lambda} \approx \alpha\lambda = \alpha\tau \left( \frac{1}{\hbar} \frac{dE_f}{d\mathbf{k}_f} \right) \quad (2.9)$$

where  $\alpha$  is the optical absorption coefficient of light for the material,  $\lambda$  is the electron inelastic mean free path,  $\tau$  is the isotropic mean period between scattering, and the last term in parenthesis is the electron's average group velocity. The approximation is made because  $\lambda$  is on the order of 10-20Å and  $\alpha$  is on the order of  $10^{-3} \text{ \AA}^{-1}$  for typical photoemission energies. The transmission function through the material surface can be written as:

$$T(E_f, \mathbf{K}_{//}) = \theta \left( E_f - E_V - \frac{\hbar^2}{2m} \mathbf{K}_{//}^2 \right) \theta(\mathbf{k}_{f\perp} + \mathbf{G}'_{\perp}) \quad (2.10)$$

where  $E_V$  is the vacuum energy.

Electrons that scatter inelastically at least once as they migrate to the surface are called secondary electrons. They have lower kinetic energy than the primary electrons and contribute a smooth background intensity to the measured intensity. There are different ways to estimate this background. Electron energy loss spectroscopy (EELS) can be used to estimate the background directly. The Tougaard method uses a generalized form of the scattering function extracted from EELS<sup>7</sup> to fit the background instead. Finally, the proportional "Shirley" procedure<sup>8</sup>, used here, assumes that the background at any given kinetic energy is proportional to the primary intensity at higher kinetic energies.

## 2.3 Angle Resolved Photoemission

In an angle resolved photoemission (ARPES) experiment, an analyzer with a small entrance aperture is used to select a specific emission direction of electrons of  $N(E_K, \hbar\omega)$ . Thus, both the kinetic energy and the momentum of the photoelectrons are determined. Because of the energy and momentum conservation relations, ARPES can be used to study the initial state of the electron before it was excited.

### 2.3.1 Momentum Relations

The magnitude of the wavevector of the photoelectron is given by:

$$K = \sqrt{\frac{2mE_K}{\hbar^2}} \quad (2.11).$$

The parallel and perpendicular components of this wavevector can be written as:

$$\begin{aligned} K_{//} &= \sqrt{\frac{2mE_K}{\hbar^2}} \sin \Theta \\ K_{\perp} &= \sqrt{\frac{2mE_K}{\hbar^2}} \cos \Theta \end{aligned} \quad (2.12)$$

where  $\Theta$  is the polar angle in the geometry shown in Figure 2-4. Since the parallel component is conserved in the escape process, this allows the determination of the parallel components of the  $\mathbf{k}_f$ . Since the momentum is also conserved for the excitation process, this gives:

$$k_{i//} = K_{//} = \sqrt{\frac{2mE_K}{\hbar^2}} \sin \Theta \quad (2.13).$$

The perpendicular component of the momentum, however, is not conserved due to the surface potential. This implies that the wavevector component  $k_{i\perp}$  is indeterminate.

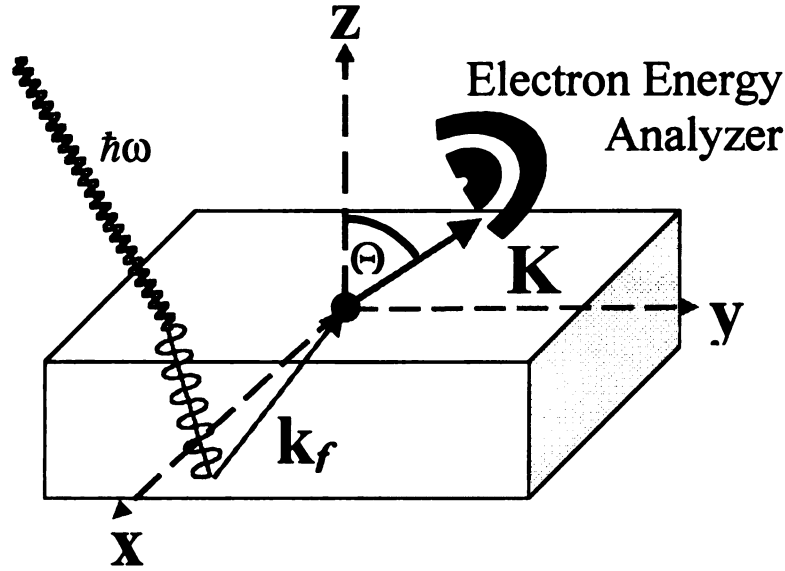


Figure 2-4: The parallel component of the electron wavevector  $k_f$  is conserved as it passes from the material into vacuum with momentum  $K$ . By measuring  $\Theta$ , the parallel components of  $K$  and  $k_f$  can be determined.

For a two-dimensional material, the band dispersions are completely determined by the parallel component of the momentum. Thus, the indeterminacy of  $k_{i\perp}$  is not a problem. Most of the work in this thesis deals with quasi-two-dimensional materials. The data interpretation is therefore particularly simple.

For three-dimensional materials, there are ways to overcome this problem. One of them is to take spectra at normal emission. In this geometry, the parallel component is zero. One can probe the band dispersion as a function of  $k_{i\perp}$  by changing the photon energy. The effective value of  $k_{i\perp}$  can be determined from the symmetries of the bands seen in the spectra.

For off normal emission,  $k_{i\perp}$  can also be determined if one makes the free electron approximation for the final state:

$$E_K = \frac{\hbar^2 k_f^2}{2m} - V_0 \quad (2.14)$$

where  $V_0$  is the inner potential. For a real material,  $V_0$  is the potential an electron has to overcome to reach the vacuum level and may have spatial or angular dependence. In the free electron approximation, the determination of this potential is simply the difference between the bottom of the free electron parabola and the vacuum level as shown in Figure 2-5. With this approximation, the normal component of the initial state's momentum is given by:

$$k_{i\perp} = \sqrt{\left(\frac{2m}{\hbar^2}(E_K + V_0) - k_{i\parallel}^2\right)} \quad (2.15).$$

$V_0$  is material specific and can be estimated from the normal emission data as mentioned previously. The free electron approximation is valid for photon energies above 100 eV. However, it has been shown that it can also be applied as a guide for much lower energies.

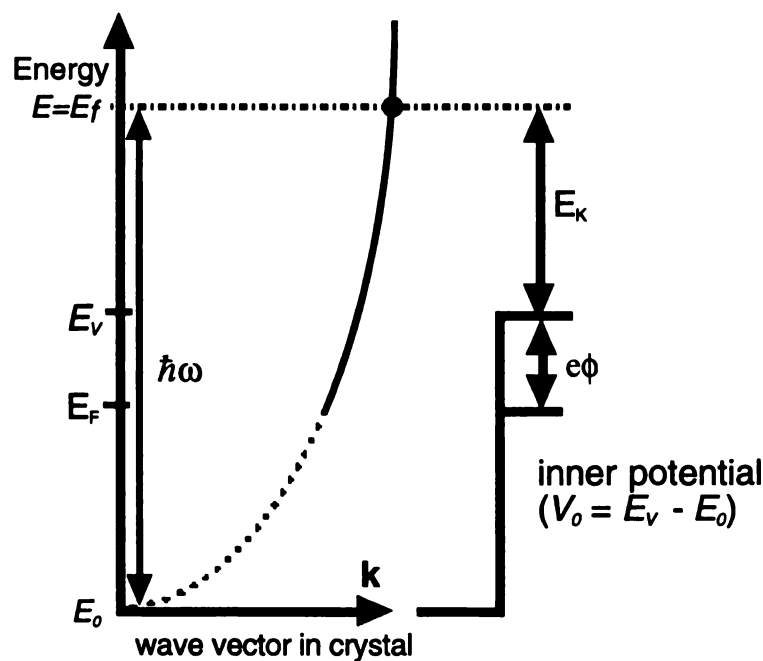


Figure 2-5: The energy levels of a free electron material. The inner potential  $V_0$  is simply the distance from the minimum of the free electron parabola to the vacuum level.

### 2.3.2 Band Mapping

Band mapping is done by taking EDCs at various  $K$ -points. The binding energy of an electronic state is determined from the peak position in the spectrum. For a quasi-two-dimensional material,  $\mathbf{K}_{\parallel}$  is varied by changing the analyzer angle. The corresponding  $\mathbf{k}_{\parallel}$  values can be calculated using (2.13). For a three-dimensional material,  $\mathbf{K}$  can be varied by changing both the analyzer angle and the photon energy.

### 2.3.3 Fermi Surface Mapping

Since the Fermi surface is crucial to most physical properties of a material, its determination is important. High resolution ARPES can be used to determine the Fermi surface by observing band dispersions near the Fermi level. The Fermi level is usually determined by measuring the EDC of a good metal, such as a Pt foil which is in electrical contact with the sample. Fermi wavevectors can be determined by observing locations where bands disperse across the Fermi level. Due to the Fermi function, the true binding energy of a peak near  $E_F$  is often not its apparent peak position. Therefore, spectra modeling is sometimes required to determine the Fermi crossings. The Fermi wavevector can be further confirmed by checking the slope of the spectral leading edge. At a Fermi crossing, the slope should have a local maximum.

Another technique for determining the Fermi surface is to make an intensity map at the Fermi level. In this technique, intensity is measured as a function of wavevector while the kinetic energy is fixed at the Fermi level. The contour of high intensity should correspond to the two-dimensional Fermi surface. The Fermi intensity map gives an overall picture of the intensity distribution in  $k$ -space. This technique is complimentary to the EDC method.

### **2.3.4 Measurement of the Energy Gap**

As a material undergoes certain phase transitions, such as a superconducting or charge density wave transition, an energy gap often opens at the Fermi level. The property of the gap is important for understanding the phase transition. High resolution ARPES is a very powerful tool for studying the gap properties.

A gap opening can be observed by measuring the spectra at a  $k$ -point where there is a Fermi crossing in the normal state at temperatures above and below the phase transition. The gap suppresses the spectral intensity at the Fermi level. As a result, the leading edge of the spectrum would appear shifted toward higher binding energy. The shift of the leading edge mid-point gives a good approximation to the size of a gap.

## Chapter 3 Charge Density Waves

Some metals, when cooled, undergo phase transitions to a new type of state. One of the possible states is a charge density wave (CDW). A CDW is a modulation of the conduction electron density and an associated modulation of the lattice atom positions into a periodic lattice distortion (PLD). A one-dimensional case is shown in Figure 3-1. In the CDW state, the charge density  $\rho(x)$  in the crystal is given by:

$$\rho(x) = \rho_0 [1 + p \cos(Q \cdot x)] \quad (3.1)$$

where  $\rho_0$  is the mean electron density,  $p$  is the amplitude of the charge modulation, and  $Q$  is the modulation wavevector.

The modulation of charge causes each ion to experience a different potential. The resulting forces cause each ion to be displaced to a new equilibrium position. Electron, x-ray, or neutron diffraction can detect this PLD effect. New diffraction satellites appear in addition to the Bragg spots from the underlying lattice. The charge modulation can be detected by x-ray spectroscopy, nuclear magnetic resonance, and scanning tunneling microscopy (STM).

The CDW wavevector  $Q$  may be incommensurate with the spacing of the underlying lattice. This alters the material so that it is no longer truly periodic, having two unrelated periods. For some materials, the wavevector  $Q$  may become commensurate with the lattice at lower temperatures. When this occurs, the modulation of the charge and atomic lattice positions simply gives the crystal a larger unit cell.

### 3.1 Electronic Susceptibility and Fermi Surface Nesting

The onset of a CDW is caused by the instability of the metallic Fermi surface resulting from the electron-phonon interactions. The response of an electron gas to an

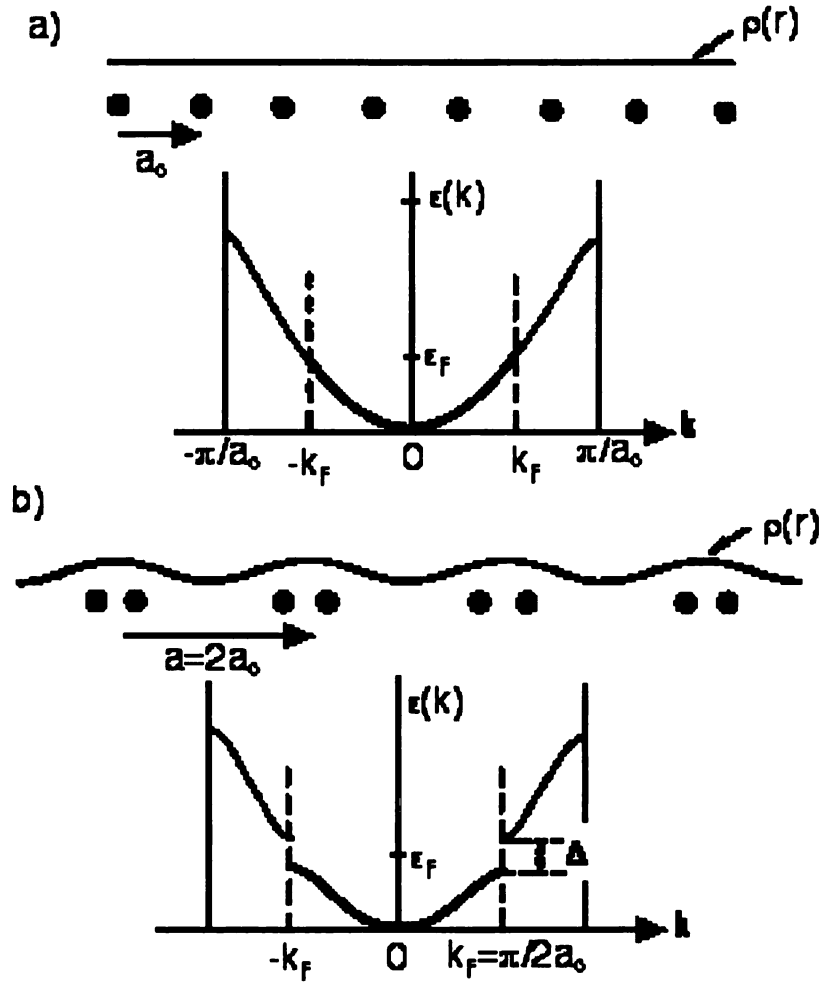


Figure 3-1: The electronic band structure opens a gap,  $\Delta$ , when the material goes from a) the normal state to b) the CDW state. The solid and dashed vertical lines define the normal state and PLD Brillouin zone respectively.

external perturbation is described by the electronic susceptibility:

$$\chi_{\mathbf{q}} = \sum_{\mathbf{k}} \frac{f_{\mathbf{k}} - f_{\mathbf{k}+\mathbf{q}}}{\epsilon_{\mathbf{k}+\mathbf{q}} - \epsilon_{\mathbf{k}}} \quad (3.2)$$

where  $f_{\mathbf{k}}$  is the Fermi-Dirac function,  $\epsilon_{\mathbf{k}}$  is the energy and  $\mathbf{k}$  indicates the wavevector of the state. The system becomes unstable when  $\chi_{\mathbf{q}}$  diverges. From equation (3.2), the most significant contributions to  $\chi_{\mathbf{q}}$  come from states whose wavevectors differ by  $\mathbf{Q}=2\mathbf{k}_F$ , the distance between two points of the Fermi surface where the states have the same energy. For a one dimensional electron gas, the Fermi surface consists of two parallel planes, as

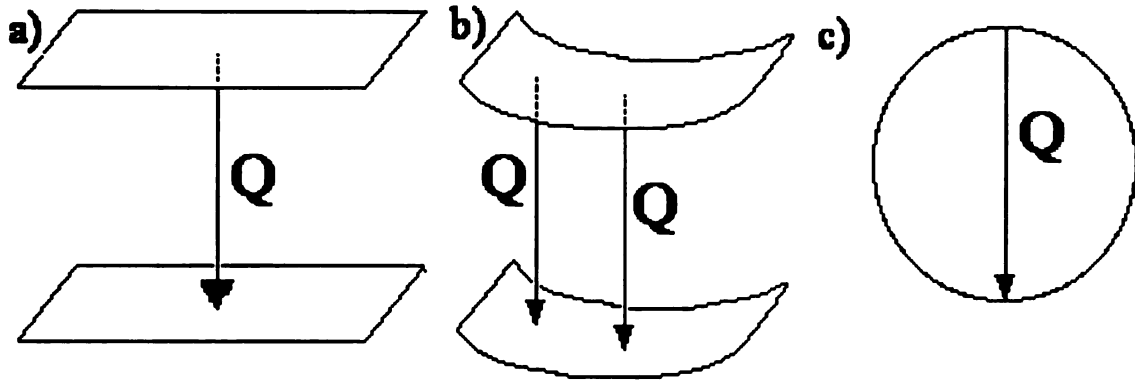


Figure 3-2: Examples of Fermi nesting for a) one-dimensional free electrons, b) arbitrary two-dimensional material and c) closed, two-dimensional cylinder. In a) and b), the nesting is perfect, but c) shows very imperfect nesting.

shown in Figure 3-2 a). All states on one sheet of the Fermi surface are related to the states on the other sheet by the same wavevector  $\mathbf{Q}=2\mathbf{k}_F$ . Such Fermi surface topology is called perfect nesting. In this case,  $\chi_q$  diverges at  $\mathbf{q} = \mathbf{Q}$  as shown in Figure 3-3. In higher dimensions, the number of nesting states is significantly reduced. This leads directly to a weakening of the singularity as indicated.

In a real material, the shape of the Fermi surface is distorted from that of a free electron gas by the periodic potential. It is possible to have a large number of states paired by the same connecting wavevector  $\mathbf{Q}=2\mathbf{k}_F$ . Figure 3-2 b) shows a hypothetical example for a two-dimensional case. In such cases,  $\chi_q$  still develops a singularity at  $\mathbf{Q}=2\mathbf{k}_F$ . In most systems, there is only imperfect, partial nesting of the Fermi surface as shown in Figure 3-2 c). Some systems can still be driven into new states by even this moderate nesting.

### 3.2 The Energy Gap and the Kohn Anomaly

The microscopic theory of CDW<sup>9</sup> formation can be approached by using the

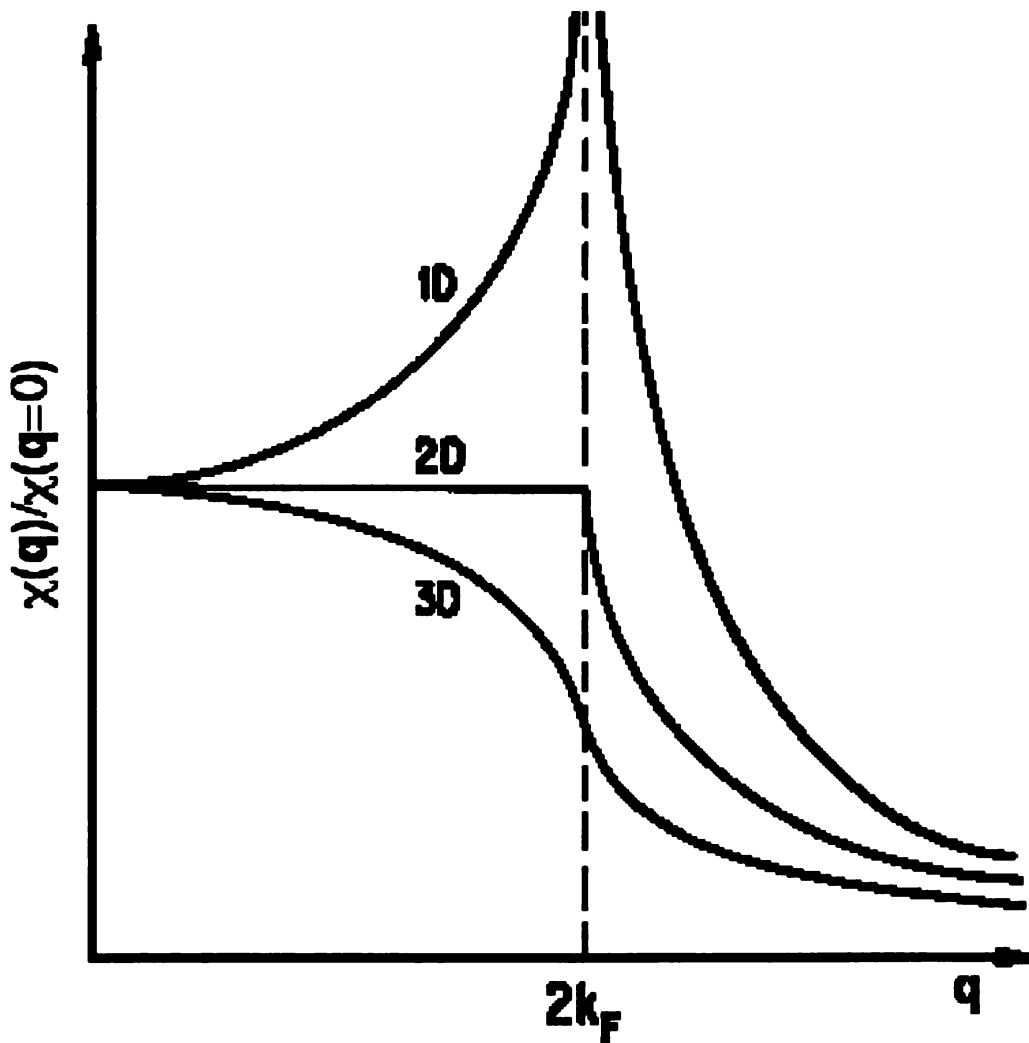


Figure 3-3: Electronic susceptibility for a free electron gas normalized to the undisturbed system as a function of disturbance wavevector  $q$ <sup>10</sup>. Depending on the dimensionality of the material, a disturbance of  $Q=2k_F$  can create a singularity, a sharp step or a weak shoulder.

mean-field approximation. The formalism is very similar to that of the Bardeen-Cooper-Schriffer (BCS) theory of superconductivity. The simplest model is that of Peierls<sup>11</sup> and Fröhlich<sup>12</sup> who considered noninteracting electrons in a one-dimensional metal.

Electrons moving among a chain of equally spaced atoms with wavevector  $k$  have an energy  $\epsilon(k)$  as shown in Figure 3-1 a). At zero temperature, the states are filled up to the Fermi energy  $\epsilon_F$  and the states above  $\epsilon_F$  are empty. Applying a periodic potential with wavevector  $Q=2k_F$  creates an energy gap at the Fermi surface as shown in Figure 3-1 b).

The energies of the occupied states below  $\epsilon_F$  are lowered and the empty states above it are raised. The electronic energy of the system, which only depends on the occupied states, is thereby reduced. If this electronic energy reduction is larger than the energy cost of the lattice distortion, a CDW will spontaneously develop. For a true one-dimensional system at zero temperature, this must always occur. As the temperature increases, thermally excited electrons will reduce the gap at the Fermi level until at some transition temperature  $T_0$  it closes entirely. The dependence of the gap on temperature is the same as the BCS relation for superconductivity shown in Figure 3-4. In the weak

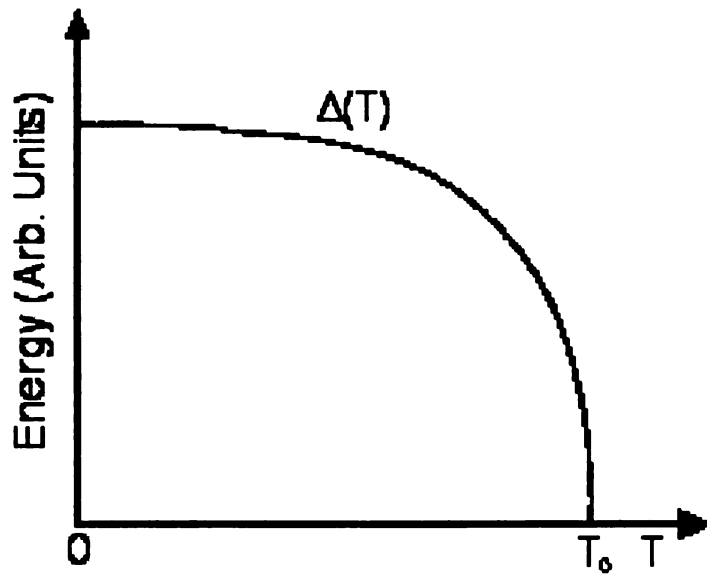


Figure 3-4: The temperature dependence of the CDW gap in the weak coupling limit.

coupling limit, the gap can be related to the onset temperature by the BCS relation:

$$2\Delta_{\max} = 3.5k_b T_0 \quad (3.3)$$

where  $T_0$  is the onset temperature of the CDW. In a strong coupling limit, this relationship may not hold. Therefore, the gap size can be used in some degree to probe the coupling strengths in a CDW material.

It can be shown that the electron-phonon interaction leads to a renormalized phonon frequency spectrum. Due to the divergence of the susceptibility at  $Q = 2k_F$  at low temperature, the phonon frequency is reduced or softened at this wavevector as shown in Figure 3-5. This phenomenon is called the Kohn anomaly. With decreasing temperature, the renormalized phonon frequency goes to zero and this defines a transition

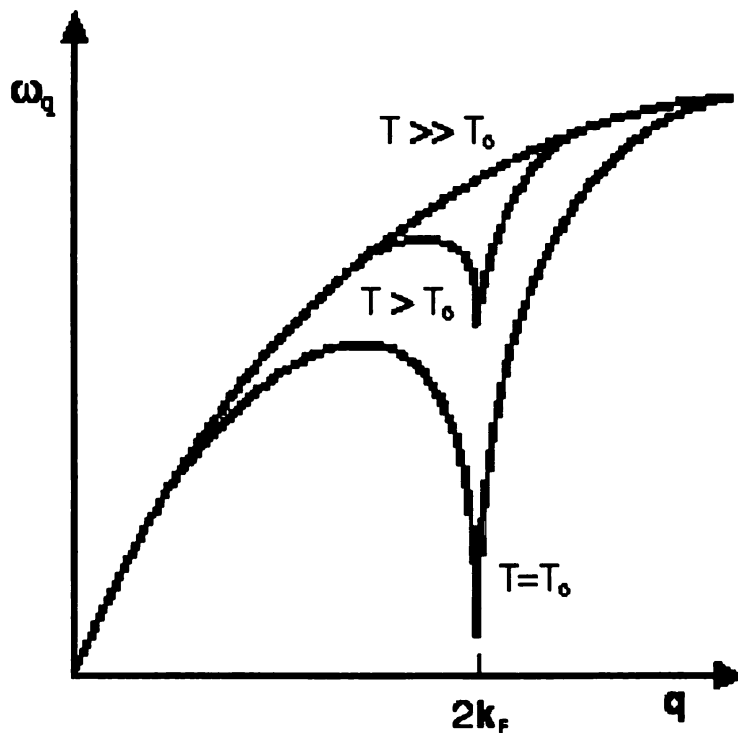


Figure 3-5: Longitudinal acoustic phonon dispersion relation of a one-dimensional metal at various temperatures above the mean field transition temperature  $T_0$ <sup>10</sup>.

temperature, where a frozen-in distortion occurs. In many systems, the incommensurate CDW sets in before the phonon energy goes entirely to zero and the commensurate CDW phase results when the phonon energy reaches zero.

### 3.3 Other Physical Properties Related to CDW

The development of a CDW affects other physical properties of the material such as the resistivity, magnetic susceptibility, Hall coefficients, and Seebeck coefficient.

### 3.3.1 Resistivity

The resistivity usually shows an anomaly at the CDW transition temperature. Since the CDW opens an energy gap on the Fermi surface, normally the resistivity increases at the onset of the CDW. However, there are exceptions, such as the resistivity decrease in some 2H-polytypes of the transition metal dichalcogenides. These will be discussed in the next chapter.

### 3.3.2 Magnetic Susceptibility

The magnetic susceptibility indicates how the system responds to an external magnetic field. As such, it is sensitive to the rearrangement of the electron density by the CDW and the underlying ionic lattice by the PLD. Thus, it shows anomalies at CDW transitions, either as a discontinuity or a change in slope.

### 3.3.3 Hall Coefficient

The Hall coefficient depends on the difference of hole and electron carrier concentration and their respective mobilities. Thus, it is sensitive to the removal of the Fermi surface in limited regions. Only a rough qualitative approximation of the Hall coefficient,  $R_H$ , is necessary to highlight the likely effects of the change in relative concentrations of electron and hole carriers. For this purpose, the simplified two-carrier model equation from Wilson<sup>13</sup>:

$$R_H = \frac{p - n(\mu_n/\mu_p)^2}{[p + n(\mu_n/\mu_p)]^2} \quad (3.4)$$

where  $p$  indicates the concentration of the positive hole carriers,  $n$  the concentration of the negative electron carriers, and  $\mu_p$  and  $\mu_n$  their respective mobilities. The opening of an

energy gap in the CDW phase causes a change in  $R_H$ . If the carrier concentrations or mobilities are altered by the CDW significantly enough,  $R_H$  can even change sign.

### 3.3.4 Seebeck Coefficient

Probing the thermopower, or the Seebeck coefficient, gives further information on the carrier concentrations of a material. The Seebeck coefficient,  $S$ , also depends on the hole and electron carrier concentrations. A qualitative two carrier model from Wilson<sup>13</sup> is given by:

$$S = \frac{p|S_p| - n|S_n|}{p + n} \quad (3.5)$$

where  $S_p$  and  $S_e$  are the Seebeck coefficients of the  $p$ - and  $n$ -type carriers respectively.

## Chapter 4 Transition-Metal Dichalcogenides

The transition-metal dichalcogenides (TMDs) have the chemical formula  $\text{MX}_2$ , where M is a transition metal such as V, Ti, Ta, Nb, Hf or Mo, and X is a chalcogen atom of S, Se, or Te. This group of materials is interesting because they are simple compounds but show a broad variety of properties. For example, many of them show superconducting and CDW transitions at low temperatures.

### 4.1 Structure

The basic crystal structure of the TMDs consists of a sheet of hexagonally packed metal atoms sandwiched between two sheets of hexagonally packed chalcogen atoms. The atoms within a sandwich are covalently bonded. These covalently bonded sandwiches can have one of two types of coordination as shown in Figure 4-1 depending on the relative orientation of the chalcogen layers. In the octahedral coordination shown in Figure 4-1 a), the two chalcogen layers are oriented  $180^\circ$  with respect to each other. In

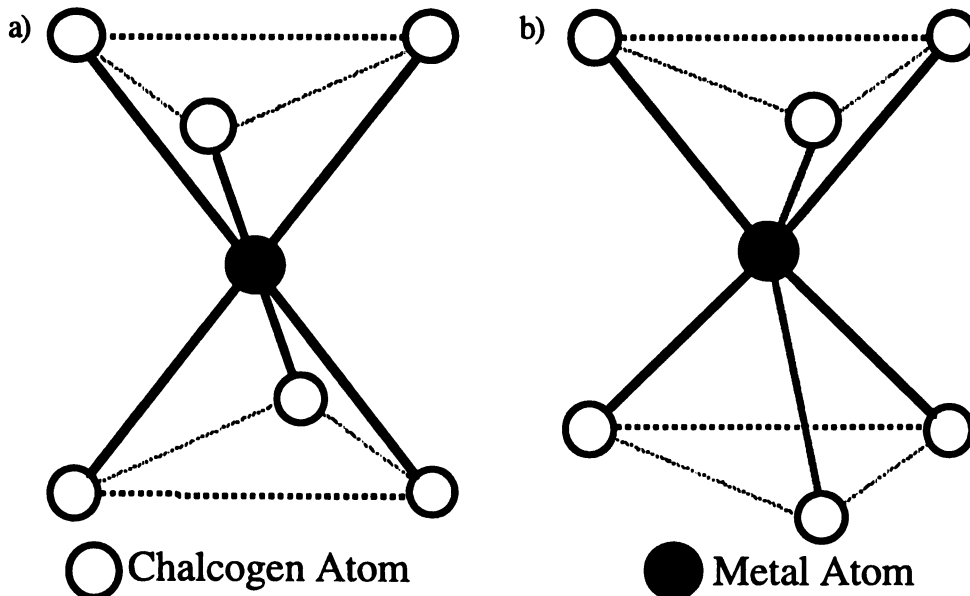


Figure 4-1: Basic TMD sandwich structures of a) octahedral and b) trigonal prismatic coordination. The octahedral has the two chalcogen layers offset by  $1/2a_0$ , while the trigonal prismatic has them aligned.

the trigonal prismatic coordination shown in Figure 4-1 b), they are oriented in the same orientation. The sandwiches are stacked along the  $c$ -axis via van der Waals forces. Various stacking sequences and registries of the sandwich layers give rise to a large number of polytypes.

The 2H and 1T polytypes, shown in the (110) plane in Figure 4-2 a) and b) respectively, are the simplest of the stacking orders. They have trigonal prismatic and octahedral coordination respectively. The 2H polytype has two trigonal prismatic coordinated sandwiches per unit cell. There are three variants of the 2H stacking order, but only the  $2H_a$  polytype was under study here. All references to the 2H polytype are therefore of the  $2H_a$  variant. The 1T polytype has a single octahedral coordinated sandwich per unit cell.

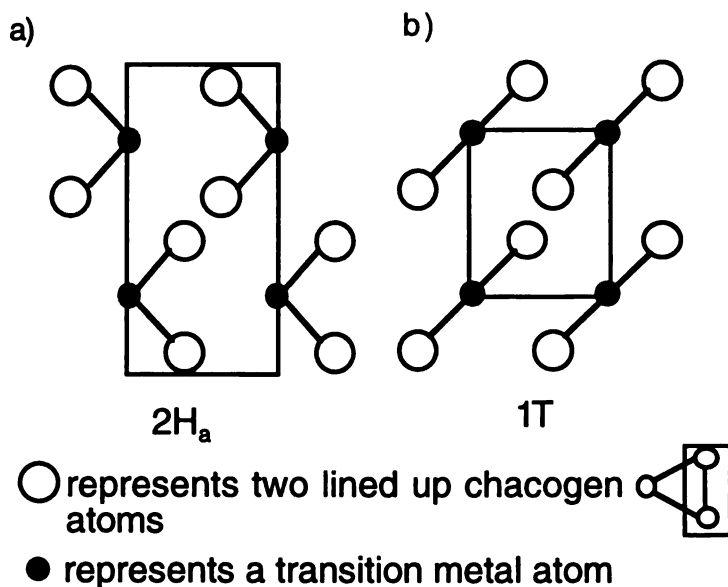


Figure 4-2: The unit cells of polytypes a) 2H and b) 1T. The stacking arrangement of the chalcogen-metal-chalcogen sandwiches and relative orientation are shown.

## 4.2 Electronic Structures

For both 2H and 1T polytypes, the Brillouin zone (BZ) is hexagonal as shown in

Figure 4-3 with the major symmetry points indicated. All polytypes have a hexagonal Brillouin zone, although they have slightly different symmetries depending on their coordination. The flat projection of the zone can be used in quasi-two-dimensional cases where the  $k_z$ -dispersion is of no concern.

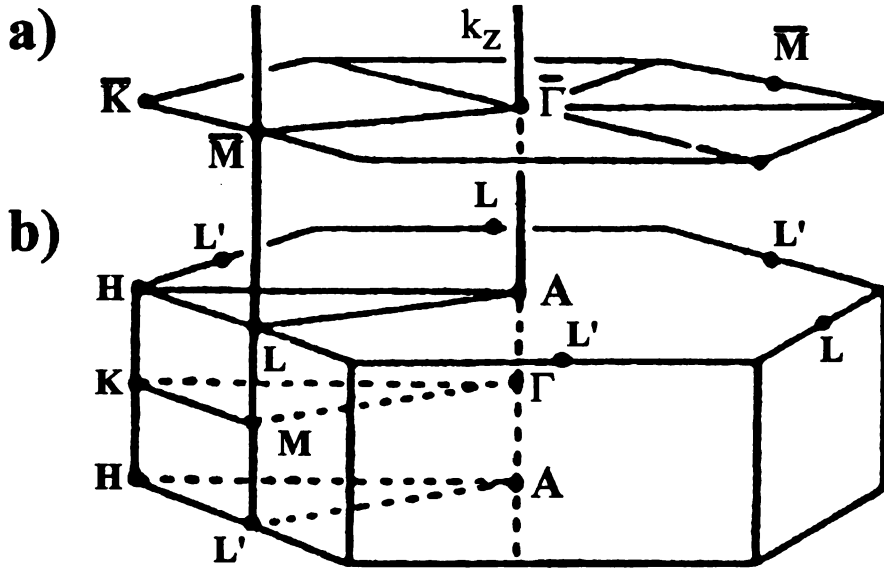


Figure 4-3: The hexagonal Brillouin zone in a) two- and b) three-dimensions.

#### 4.2.1 2H-TaSe<sub>2</sub>, 2H-TaS<sub>2</sub>, and 2H-NbSe<sub>2</sub>

Figure 4-4 shows the band dispersions near  $E_F$  for a) 2H-NbSe<sub>2</sub>, b) 2H-TaS<sub>2</sub> and c) 2H-TaSe<sub>2</sub> calculated by Wexler and Woolley<sup>14</sup> using the layer method. They are all very similar, with two bands crossing  $E_F$  along the  $\Gamma M$  line and two bands briefly dispersing below and then above the Fermi level along  $\Gamma K$ . The two bands are not degenerate due to the interlayer coupling. The location where the bands have maximum binding energies along  $\Gamma K$  is identified as a saddle point.

Figure 4-5 shows the Fermi surfaces of a) 2H-TaSe<sub>2</sub>, b) 2H-TaS<sub>2</sub>, and c) 2H-NbSe<sub>2</sub> from the same calculations. Because of their layered structures, the Fermi surfaces are highly two-dimensional in that they are cylinders slightly corrugated along the  $k_z$ -direction. The three contours, A, B, and unlabelled, in Figure 4-5 correspond to

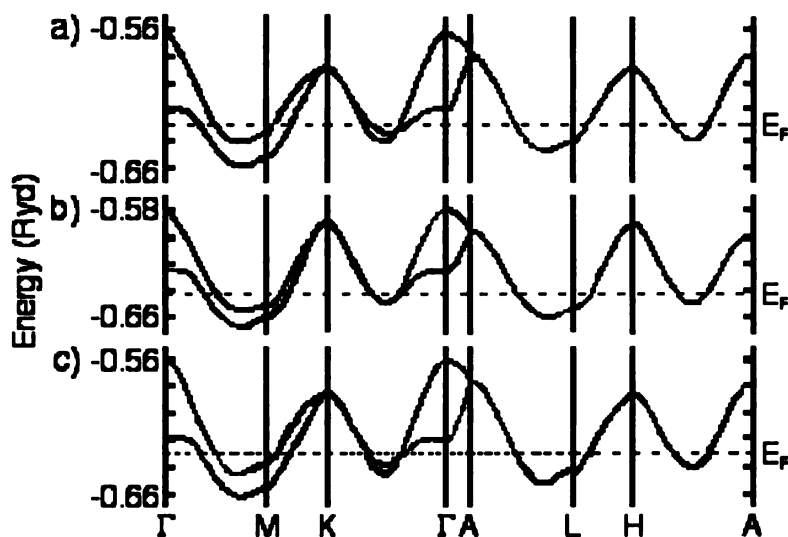


Figure 4-4: Band calculations for a) 2H-NbSe<sub>2</sub>, b) 2H-TaS<sub>2</sub>, and c) 2H-TaSe<sub>2</sub> from Wexler and Woolley<sup>14</sup>.

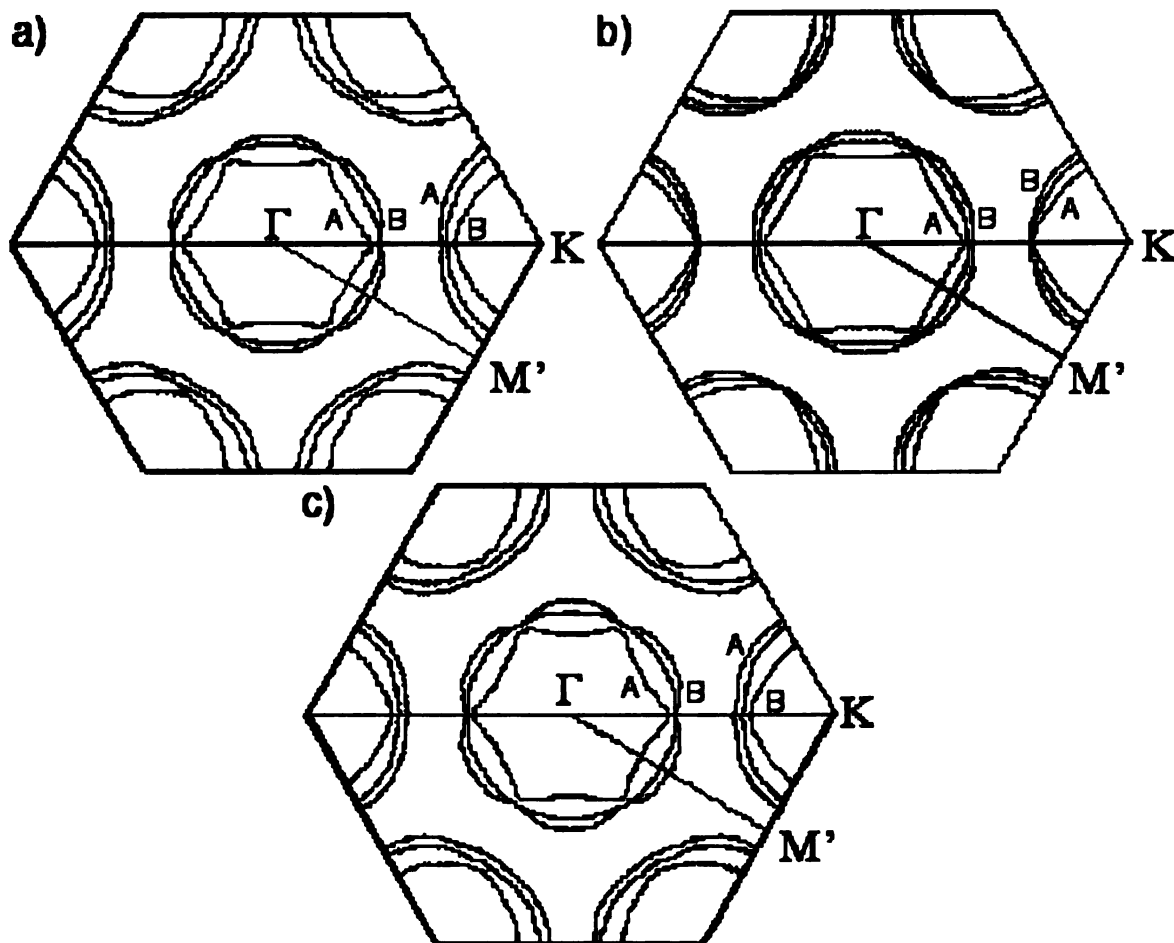


Figure 4-5: Fermi surfaces of a) 2H-TaSe<sub>2</sub>, b) 2H-TaS<sub>2</sub>, and c) 2H-NbSe<sub>2</sub>. Curves A and B are at equivalent height in the conventional zone. The middle, unlabeled curve is at the top of zone.

Fermi surfaces at  $k_z = 0, 2\pi/c$  and  $\pi/c$  respectively. The separations between these contours indicate the amount of  $k_z$ -dispersion. As can be seen, the Fermi surfaces for these three materials all consist of a cylinder around  $\Gamma A$  and another cylinder around  $KH$ . The cylinders are double walled except at the top of the BZ because there are two sandwiches per unit cell. It can be shown that the double walled cylinder can be unfolded into a single walled cylinder in the double-zone scheme along  $k_z$ <sup>14</sup>.

#### 4.2.2 1T-TaS<sub>2</sub>

Figure 4-6 shows the Fermi surface of 1T-TaS<sub>2</sub> in the normal state extracted from the non-self consistent non-relativistic band structure calculation by Mattheiss<sup>15</sup>. It is comparable to other band calculations<sup>16,17,18</sup>. The FS is also highly two-dimensional, consisting of elliptical cylinders around  $ML$ .

Recently, Larson and Mahanti<sup>19</sup> performed self-consistent band structure calculations using the full-potential linearized augmented plane-wave (FLAPW) method<sup>20</sup> within the density functional theory<sup>21</sup>. The generalized gradient approximation (GGA) of Perdew et. al.<sup>22</sup> was used for the exchange and correlation potential. The band

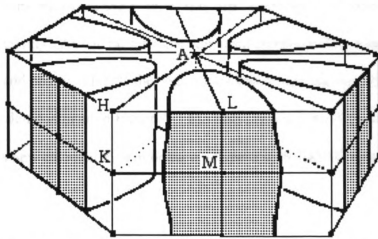


Figure 4-6: Fermi surface of 1T-TaS<sub>2</sub> extrapolated from calculations without relativistic spin orbit corrections.

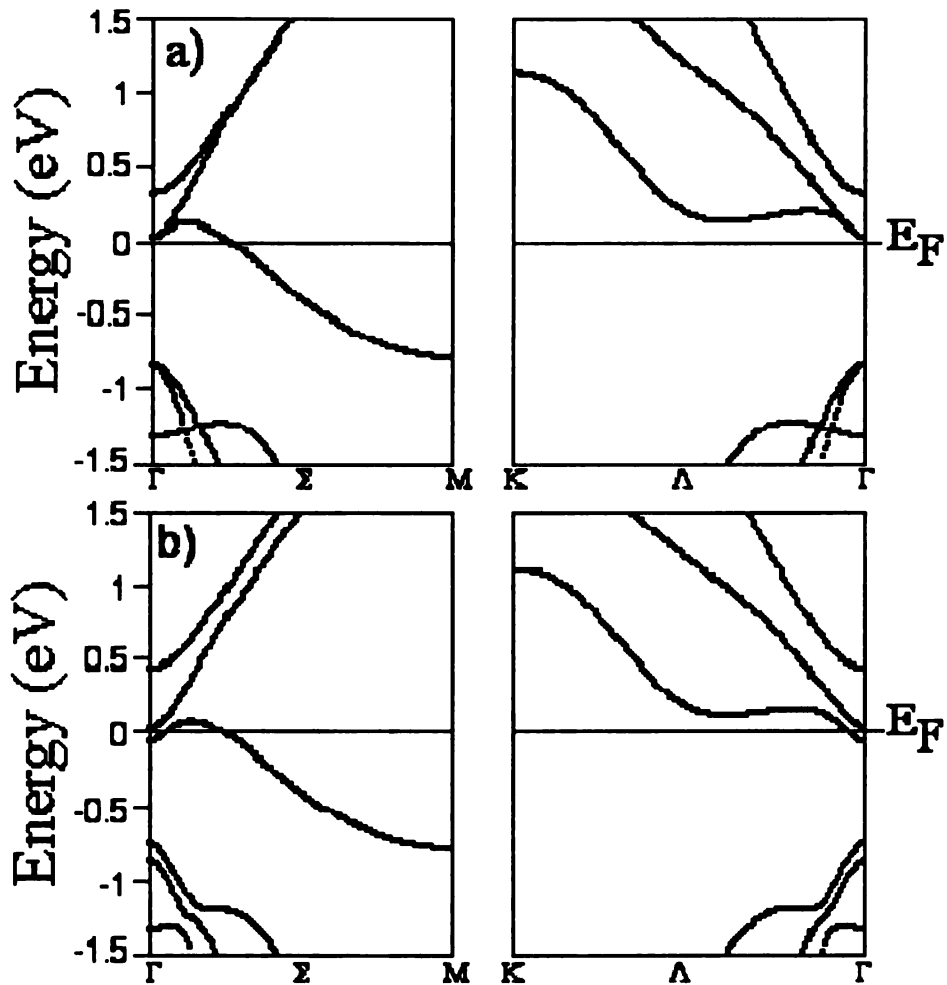


Figure 4-7: 1T-TaS<sub>2</sub> band calculations a) with and b) without relativistic spin orbit corrections along the  $\Gamma$ M and  $\Gamma$ K symmetry lines.

dispersions near  $E_F$  both with and without spin orbit corrections are shown in Figure 4-7 a) and b) respectively. As can be seen, the spin orbit corrections have an important affect on the Ta  $5d$ -band near  $E_F$ . It lifts the degeneracy and brings one band below the Fermi level near  $\Gamma$  as demonstrated in Figure 4-7 b). This creates a small electron pocket around  $\Gamma$ . This new calculation is in better agreement with ARPES results as will be shown later.

### 4.2.3 1T-TiSe<sub>2</sub>

A band calculation by Benesh et. al.<sup>23</sup> of 1T-TiSe<sub>2</sub> is shown in Figure 4-8. As can be seen, bands briefly cross the Fermi level near the  $\Gamma$  and L points. These would lead to small hole and electron Fermi surface pockets respectively. Also, there is significant dispersion along the  $\Gamma$ A line, the direction perpendicular to the layers indicating three-dimensional electronic structure.

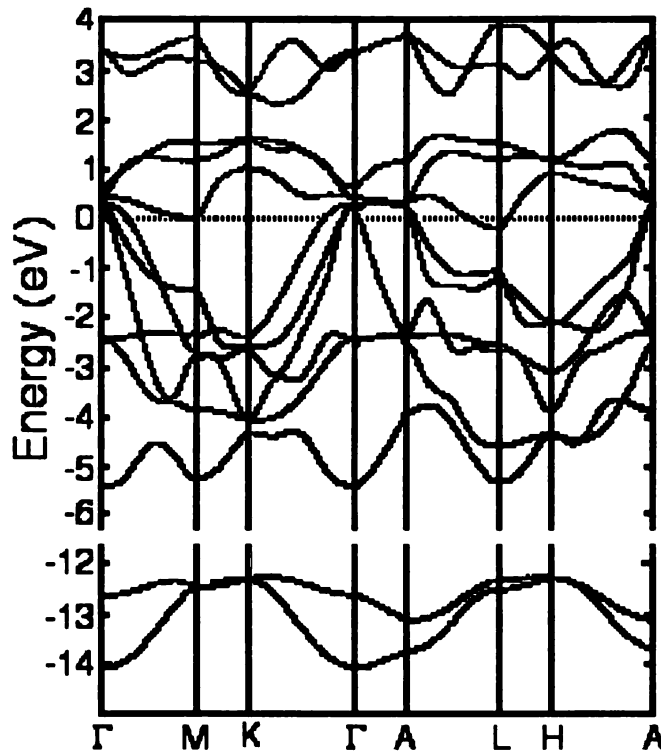


Figure 4-8: 1T-TiSe<sub>2</sub> band calculation by Benesh et. al.<sup>23</sup> with valence bands and the top most core levels.

Wilson<sup>24</sup> proposed a schematic Fermi surface as shown in Figure 4-9, with the relative size of the Fermi pockets based upon carrier concentrations. The dotted cylinder about the LM-line is the case for a Fermi surface consisting solely of electrons. The solid ellipsoids around  $\Gamma$  and L are the Fermi surface expected for hole and electron carriers respectively. Later band structure calculations performed after Wilson's proposal predict the hole and electron Fermi surface pockets.

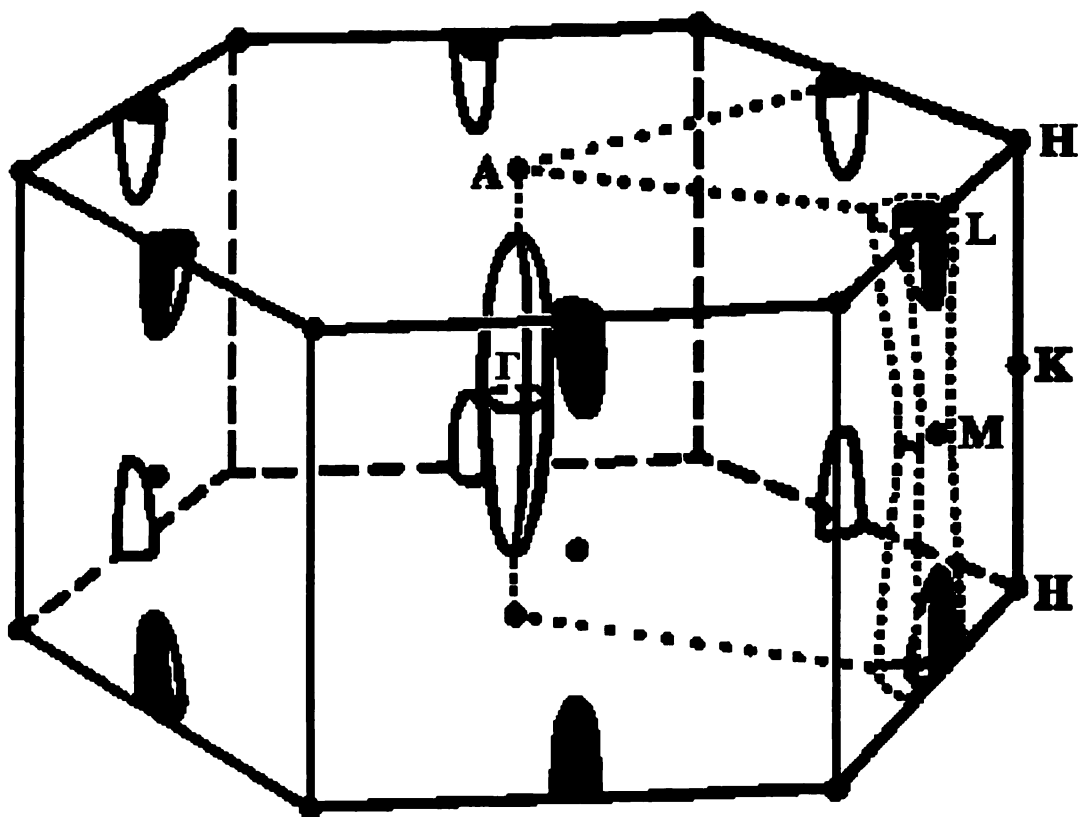


Figure 4-9: Schematic Fermi surface of 1T-TiSe<sub>2</sub> based on carrier concentrations and the measured CDW wavevector by Wilson<sup>24</sup>.

### 4.3 Charge Density Wave Transitions

A variety of CDW phase transitions have been observed in the various polytypes of the TMDs. The structural distortions accompanied by the CDW transitions have been extensively studied by electron diffraction, x-ray diffraction, neutron scattering and scanning tunneling microscopy. In general, the 2H compounds have weak second-order CDW transitions and the 1T compounds have stronger first-order CDW transitions. The 1T materials have greater material specific variations, as seen in 1T-TaS<sub>2</sub> which has a very complicated CDW phase diagram and 1T-TiSe<sub>2</sub> which has a single transition as will be discussed below in detail.

Listed in Table 4-1 are the CDW transition temperatures, superlattice structure of the commensurate CDW and crystal lattice dimensions of 2H-TaSe<sub>2</sub>, 2H-TaS<sub>2</sub>, 2H-

NbSe<sub>2</sub>, 1T-TaS<sub>2</sub>, and 1T-TiSe<sub>2</sub>. The following sections will review the CDW properties and other relevant physical properties such as resistivity, magnetic susceptibility, the Hall coefficient and the Seebeck coefficient of each material.

**Table 4-1**

Material	T <sub>0</sub> (K)	T <sub>1</sub> (K)	Superlattice	Lattice Constants (Å)
2H-TaSe <sub>2</sub>	122.3	~90	3a <sub>0</sub> x 3a <sub>0</sub>	a <sub>0</sub> = 3.436, c <sub>0</sub> = 12.696
2H-TaS <sub>2</sub>	75.3	~14 <sup>1</sup>	3a <sub>0</sub> x 3a <sub>0</sub>	a <sub>0</sub> = 3.315, c <sub>0</sub> = 12.104
2H-NbSe <sub>2</sub>	33	<5 <sup>2</sup>	3a <sub>0</sub> x 3a <sub>0</sub>	a <sub>0</sub> = 3.444, c <sub>0</sub> = 12.552
1T-TaS <sub>2</sub>	552 <sup>3</sup>	180 or 240 <sup>4</sup>	√13 a <sub>0</sub> x √13 a <sub>0</sub>	a <sub>0</sub> = 3.346, c <sub>0</sub> = 5.859
1T-TiSe <sub>2</sub>	--	315	2a <sub>0</sub> x 2a <sub>0</sub> x 2c <sub>0</sub>	a <sub>0</sub> = 3.542, c <sub>0</sub> = 6.015

T<sub>0</sub> is the onset temperature of the incommensurate CDW phase. T<sub>1</sub> is the commensurate CDW lock-in temperature.

1. The commensuration below this transition may be only local, broken by regions of discommensuration forming a quasi-commensurate phase.
2. The incommensurate phase clearly exists until this temperature. Below this temperature, the incommensuration is too small to be detected within scanning tunneling microscopy resolution.
3. Between the incommensurate transition and the commensurate lock-in temperature, 1T-TaS<sub>2</sub> exhibits a quasi-commensurate phase transition at 360K and a triclinic phase on warming up above the commensurate phase to 280K.
4. The first temperature is for cooling; the second is on the warming cycle.

#### 4.3.1 2H-TaSe<sub>2</sub>, 2H-TaS<sub>2</sub>, and 2H-NbSe<sub>2</sub>

For the 2H materials considered here, the CDW phase transitions occur well below room temperature. In the case of 2H-TaSe<sub>2</sub>, the weak second-order transition to the I-CDW phase occurs at 122.3 K followed by the C-CDW transition at 90 K. 2H-TaS<sub>2</sub> undergoes a weak second-order transition to the I-CDW phase at 75.3 K. Evidence for a

locally commensurate phase below 14 K is suggested by nuclear magnetic resonance (NMR) studies<sup>25</sup> taken at 4.2 K. 2H-NbSe<sub>2</sub> has the lowest I-CDW transition temperature of 33 K. The CDW remains incommensurate down to at least 5 K, where the incommensuration is nearly undetectable by scanning tunneling microscopy (STM) measurements. The incommensuration does decrease with temperature, so there may be a C-CDW phase below 5 K that is just undetected presently. All three compounds have a near 3 x 3 superlattice in the CDW phases. The lattice reconstruction in the transition metal layer is shown in Figure 4-10. The enlargement of the real space unit cell causes an inversely proportional reduction of the reciprocal space Brillouin zone.

2H-TaSe<sub>2</sub>, 2H-TaS<sub>2</sub>, and 2H-NbSe<sub>2</sub> also become superconducting at 0.14 K, 0.7 K, and 7.4 K respectively<sup>26</sup>. The apparent correlation between higher superconducting transition temperature and lower CDW transition temperature suggests competition between superconductivity and CDW in these materials.

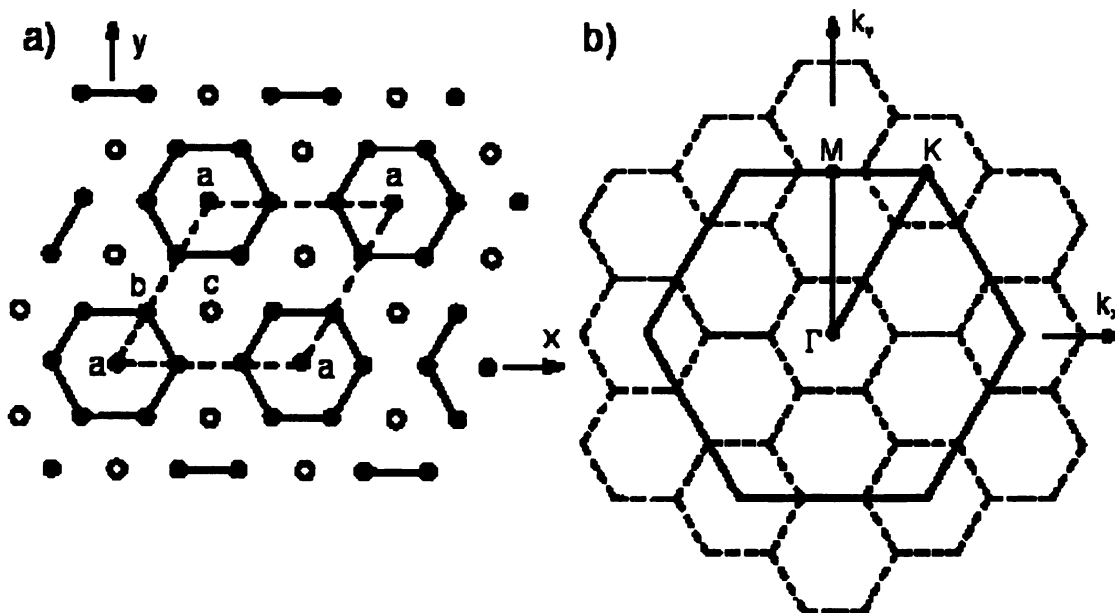


Figure 4-10: The 3 x 3 superlattice effect on a) the real space cell and b) the reciprocal space Brillouin zone. The lattice change generates three inequivalent atomic sites  $a$ ,  $b$ , and  $c$  as labeled in ratios of 1::6::2.

### 4.3.1.1 Resistivity

Figure 4-11 shows the in-plane resistivity as a function of temperature for 2H-TaSe<sub>2</sub> and 2H-TaS<sub>2</sub> and 2H-NbSe<sub>2</sub>. As can be seen, all three materials exhibit a resistivity decrease at the onset of the CDW transition. This is rather unusual because normally a CDW should cause a resistivity increase due to gapping at the Fermi level. Because of this unusual behavior, the CDW mechanism for this group of materials has been a subject of debate for decades. Several models were proposed to explain the resistivity decrease.

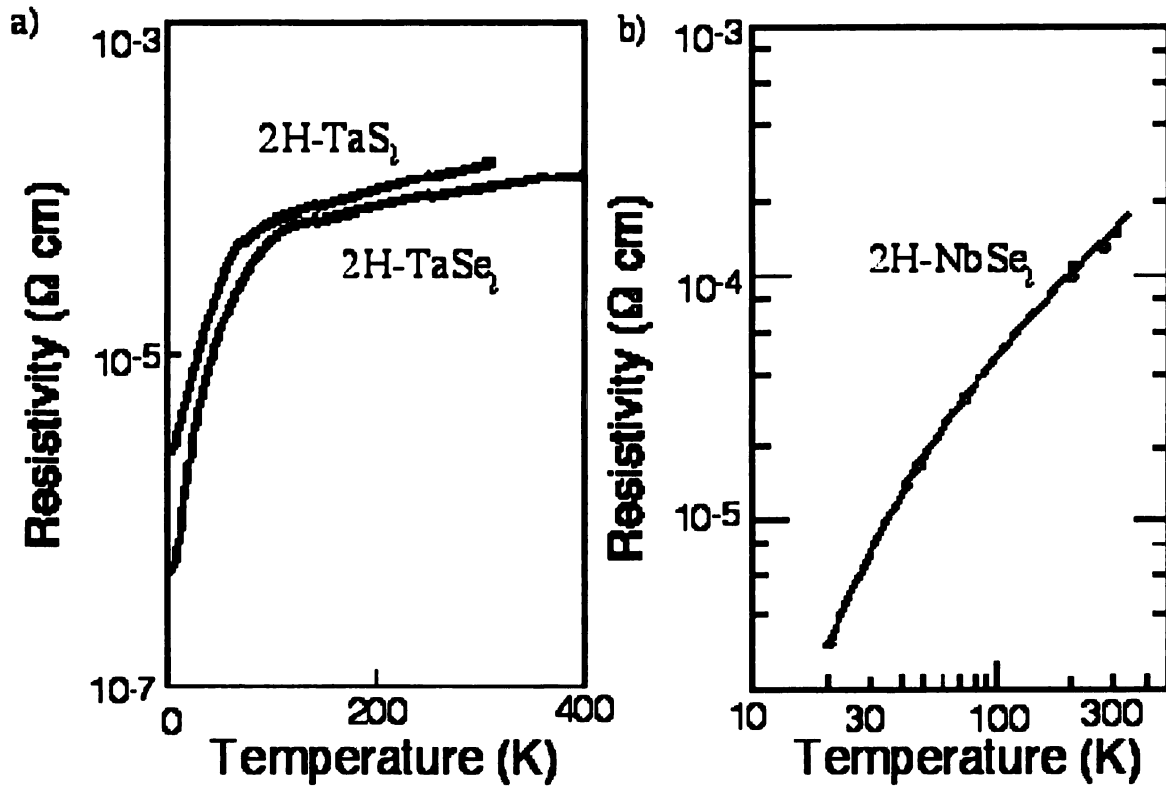


Figure 4-11: Resistivity data parallel to the layers versus temperature for 2H polytypes a) 2H-TaSe<sub>2</sub> and 2H-TaS<sub>2</sub> from Di Salvo and Rice<sup>7</sup> (log plot) and b) 2H-NbSe<sub>2</sub> from Edwards and Frindt<sup>27</sup> (log-log plot).

Rice and Scott<sup>28</sup> proposed a saddle band model. It was based on a schematic FS shown in Figure 4-12 derived from band calculations by Mattheis<sup>15</sup>. On this FS, there are a set of six saddle points at approximately the midpoints of  $\Gamma K$  symmetry lines of the

Brillouin zone. Using susceptibility arguments, they concluded that if the saddle point was within  $\sim k_B T_0 = 0.01$  eV of the Fermi level, then a CDW would result. They further argued that the saddle points act as scattering sinks in the normal state. Therefore, their removal in the CDW state would lead to the resistivity decrease observed experimentally.

However, later band calculations were made with improved techniques that indicated the saddle point was not close enough in energy to the Fermi level. Furthermore, the newer band calculations suggested the saddle point was not at the midpoint of the  $\Gamma$ K symmetry line. These predictions removed support for the Rice-Scott

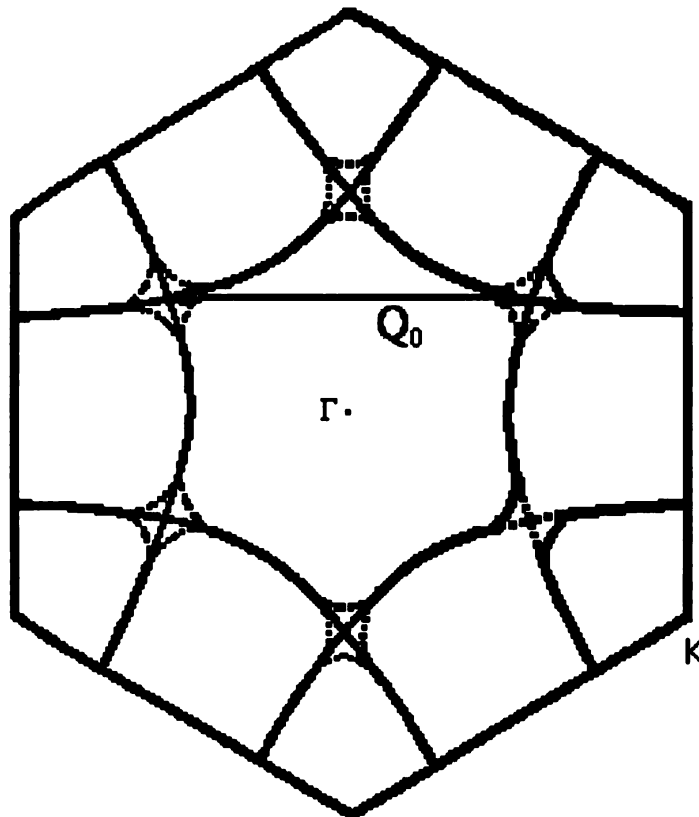


Figure 4-12: The schematic Fermi surface Rice and Scott<sup>28</sup> used. The real system shows a Fermi surface similar to the thick solid curves shown in the lower right K region. The saddle point is the crossing of the dashed lines.

model. An alternative model was suggested by Wilson<sup>13</sup>. He suggested that the CDW is caused by nesting of region of the Fermi surface with heavy effective carrier masses.

Gapping on those parts of the Fermi surface can also lead to a resistivity decrease by removing carriers that worsen the conduction of the 2H polytypes. As will be shown in Chapter 6, direct measurements of the band dispersions and the CDW energy gap using high resolution ARPES clarify if either of these theories is applicable.

#### 4.3.1.2 Magnetic Susceptibility

The magnetic susceptibility gives information on the density of state near the Fermi level. From the relative strength of the raw data, which is not shown here, these materials have moderately high concentrations of carriers near the Fermi level, which agrees with the predictions of band structure calculations. In Figure 4-13, magnetic susceptibility data, normalized at 300K for comparison, of 2H-TaSe<sub>2</sub>, 2H-TaS<sub>2</sub>, and 2H-NbSe<sub>2</sub> by Ayache et. al.<sup>29</sup> is shown. Each material shows a distinct downturn with decreasing temperature near the CDW transition temperatures.

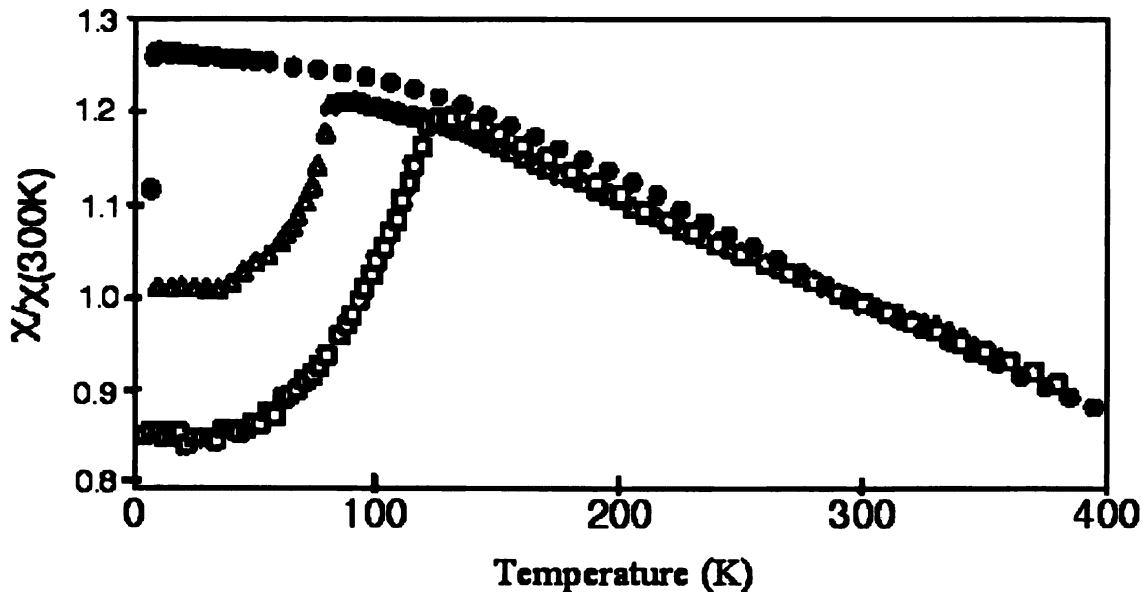


Figure 4-13: Magnetic susceptibility of 2H-TaSe<sub>2</sub> (squares), 2H-TaS<sub>2</sub> (triangles), and 2H-NbSe<sub>2</sub> (circles) normalized at T= 300K by Ayache et. al.<sup>29</sup>

### 4.3.1.3 Hall and Seebeck Coefficients

The Hall coefficient is plotted versus temperature for the three materials<sup>30,31,32</sup> in Figure 4-14, and Figure 4-15. As can be seen in all three cases, the Hall coefficient undergoes a sharp decrease and a change in sign near the CDW onset transitions. The

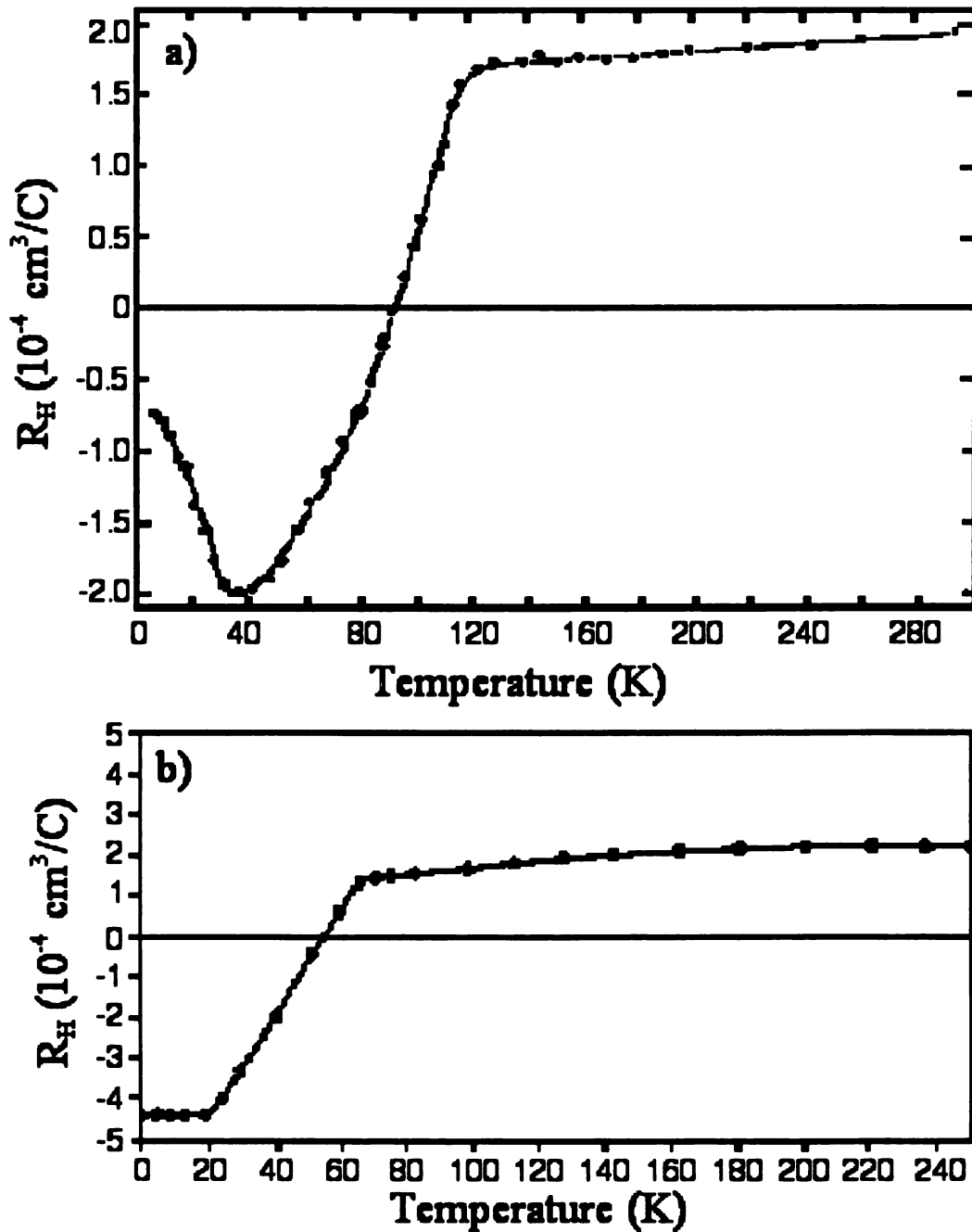


Figure 4-14: The Hall coefficient versus temperature for a) 2H-TaSe<sub>2</sub> by Lee et. al.<sup>30</sup> and b) 2H-TaS<sub>2</sub> by Thompson et. al.<sup>31</sup>.

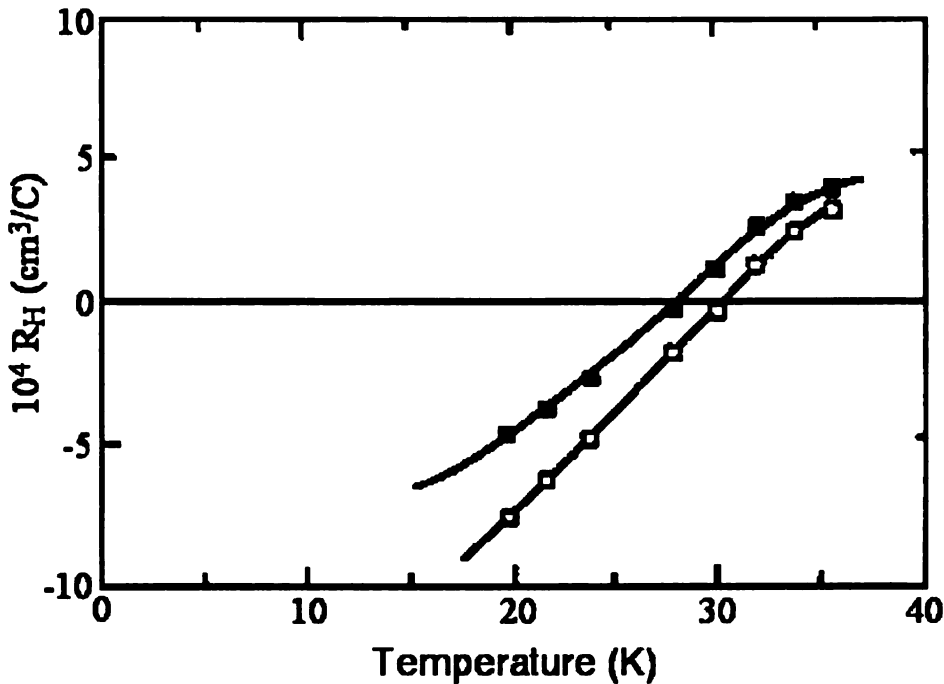


Figure 4-15: The Hall coefficient versus temperature for 2H-NbSe<sub>2</sub> at 28.6 kG (empty squares) and 150 kG (solid squares) from Whitney et. al.<sup>32</sup>

change in sign from positive to negative indicates that there is an improvement in the electron carrier term in comparison to the hole carrier term in the CDW state.

The Seebeck coefficient is negative for all three materials at room temperature, approximately  $-10 \mu\text{V/K}$  for 2H-TaSe<sub>2</sub>,  $-7 \mu\text{V/K}$  for 2H-TaS<sub>2</sub>, and  $-10 \mu\text{V/K}$  for 2H-NbSe<sub>2</sub>. The Seebeck coefficient also undergoes a sign change as the CDW forms as demonstrated in example Figure 4-16 for 2H-NbSe<sub>2</sub> from Huntley and Frindt<sup>33</sup>. For a one-band system, the Seebeck and Hall coefficients are expected to have the same sign. Since their Hall coefficients have the sign opposite of the Seebeck coefficients in both states, this indicates that there is an overlapping two-band model. In the normal state, there are more electrons than holes, but a greater mobility for the holes than the electrons. The opposite sign of the Seebeck coefficients at room temperature indicates that there is more than just a change in relative carrier concentrations since it still has the sign opposite to the Hall coefficient in the CDW state.

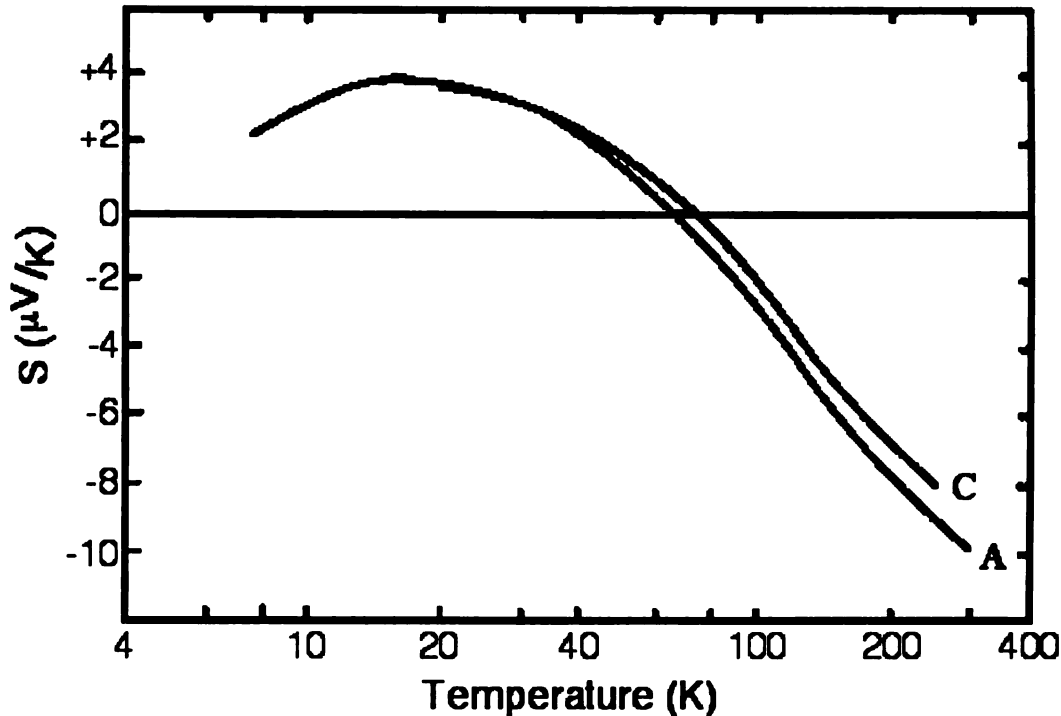


Figure 4-16: Seebeck coefficient plotted against the log of temperature for two samples of 2H-NbSe<sub>2</sub> from Huntley and Frindt<sup>33</sup>.

#### 4.3.2 1T-TaS<sub>2</sub>

1T-TaS<sub>2</sub> can be obtained by quenching it from at least 1023 K to room temperature. It remains in the normal state down to 552 K, but it tends to destabilize into the 2H polytype much above this transition. Below 552 K, the material forms an I-CDW. At 360 K, the material enters a quasi-commensurate phase (QC-CDW) with commensurate domains. Another phase, the triclinic CDW (T-CDW) phase, is seen between 280 K and 360 K on warming. The transition from the QC-CDW to the C-CDW shows a hysteresis, shifting at 180 K on cooling and at 240 K on warming. The QC-CDW to C-CDW phase transition occurs at 180 K on cooling and at 240 K on warming. In the C-CDW phase, it forms a  $\sqrt{13} \times \sqrt{13}$  superlattice rotated 13.54° to the original lattice which generates three inequivalent sites of *a*, *b*, and *c*. The reconstructed structure is shown in Figure 4-17. The ring of six *b* atoms around each *a* shift straight towards *a*.

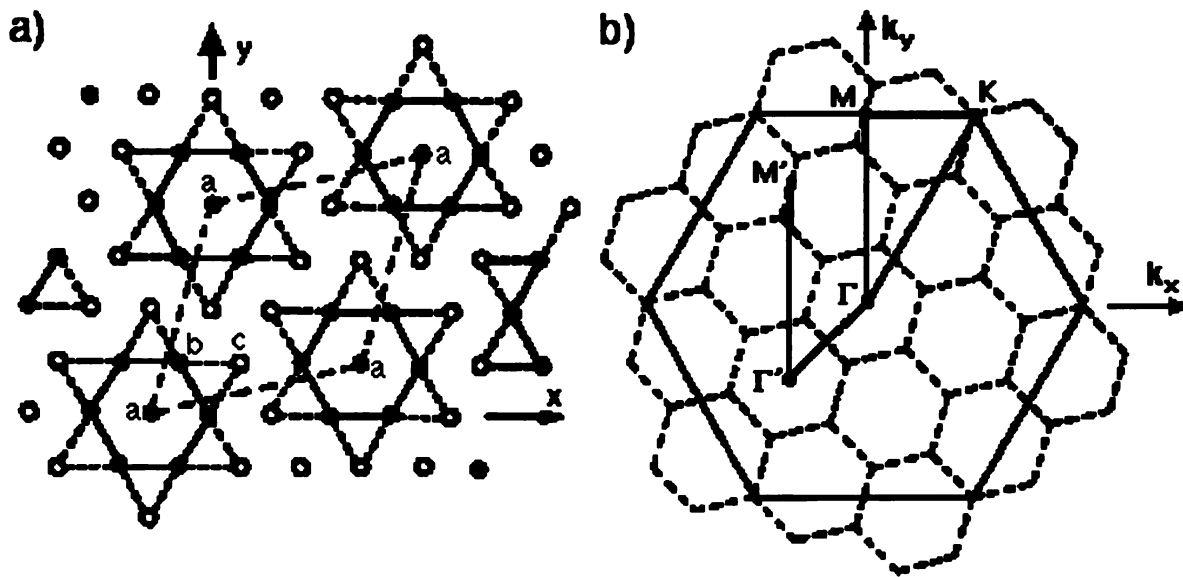


Figure 4-17: The  $\sqrt{13} \times \sqrt{13}$  superlattice effects on a) the real space cell and b) the reciprocal space Brillouin zone of the CDW in 1T-TaS<sub>2</sub>. The reconstruction generates three inequivalent atomic sites *a*, *b*, and *c* in the ratios of 1::6::6.

The next ring of six *c* atoms around *a* are both drawn inwards and rotated slightly around *a*. This produces the pattern of a Star of David.

#### 4.3.2.1 Resistivity

Figure 4-18 shows the in-plane resistivity as a function of temperature for 1T-TaS<sub>2</sub>. As can be seen, there is a discontinuous resistivity increase upon cooling through each CDW transition, indicating that the transitions are of first order. In particular, the resistivity increases by nearly a factor of five at the onset of the C-CDW phase, exceeding the metallic limit. The formation of the C-CDW is not enough to explain this dramatic change. It has been suggested a combination of a Mott localization and an Anderson localization concurrently occurs in the C-CDW phase. The Mott localization could drive the system into an insulator state at the QC-C transition. The Anderson localization is more important at 60 K (not shown) where the resistivity starts to increase somewhat sharply with temperature.

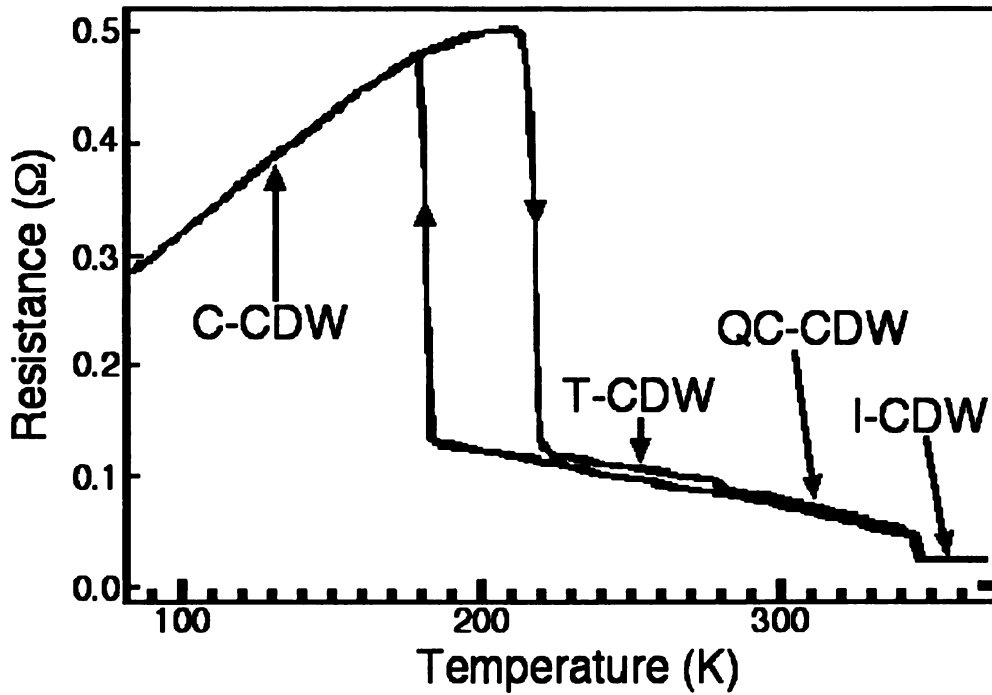


Figure 4-18: Parallel resistivity of 1T-TaS<sub>2</sub> from Manzke et. al.<sup>34</sup>

#### 4.3.2.2 Magnetic Susceptibility

The magnetic susceptibility of 1T-TaS<sub>2</sub>, as shown in Figure 4-19, shows discontinuous changes and hysteresis at the I-CDW to QC-CDW and QC-CDW to C-

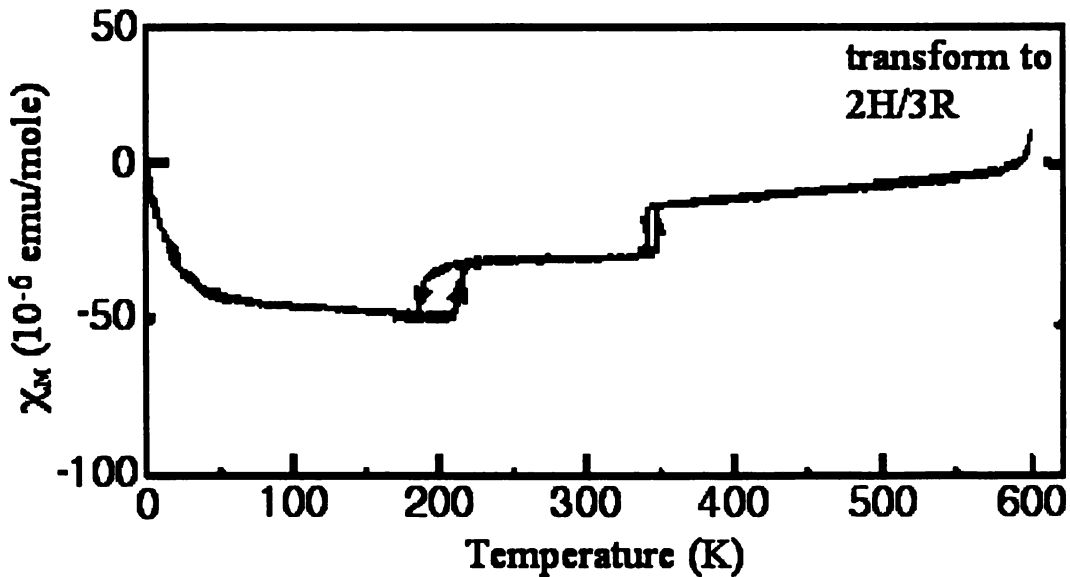


Figure 4-19: Temperature dependence of the magnetic susceptibility for 1T-TaS<sub>2</sub> by Wilson et. al.<sup>35</sup>

CDW transitions. The T-CDW phase is not resolved in this set of measurements as the transition is rather subtle. The data are also cut off at high temperature because the material tends to change polytype above 552 K.

#### 4.3.2.3 Hall and Seebeck Coefficients

The Hall coefficient for 1T-TaS<sub>2</sub> also shows a change of sign as the CDW develops. Figure 4-20 shows the Hall coefficient versus temperature as measured by Mutka et. al.<sup>36</sup> At 200 K, there is a sign reversal and a very sharp change in scale. The sign reversal indicates a change from electron like carriers to hole carriers. The change in scale indicates a decrease of carrier concentration on the order of two magnitudes. The subsequent low temperature behavior of the Hall coefficient is similar to that of an

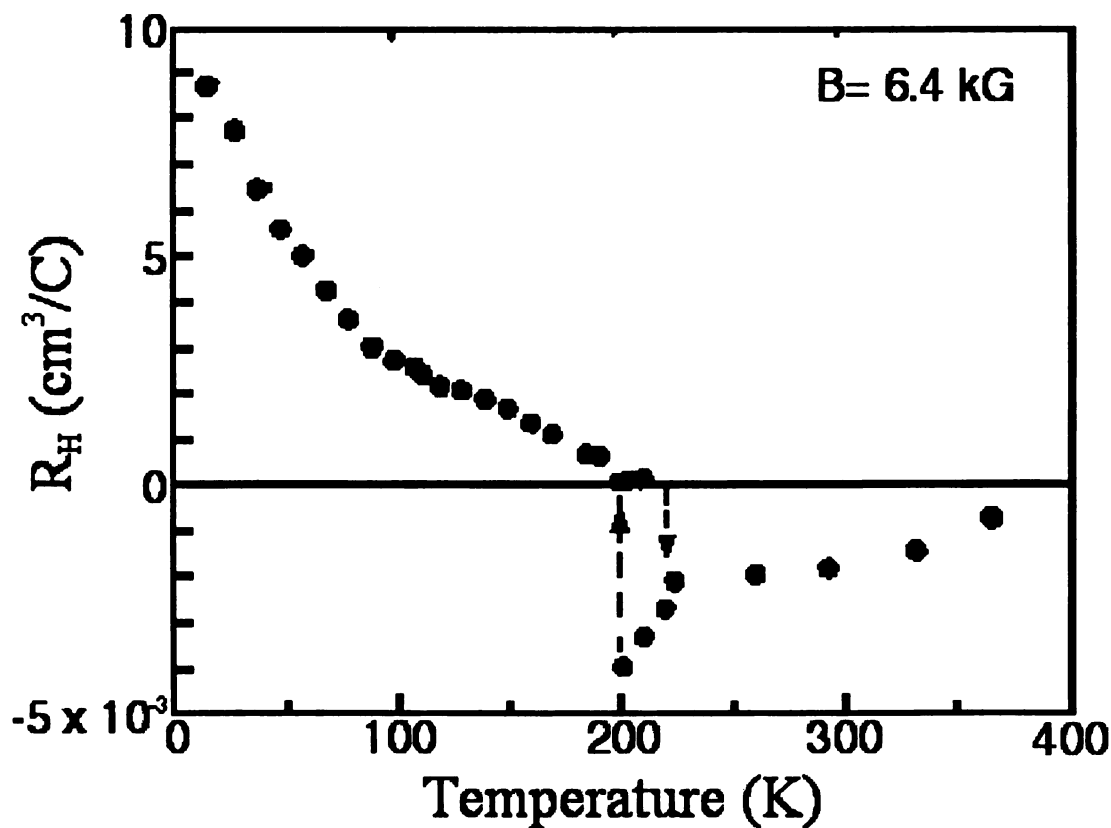


Figure 4-20: Hall coefficient versus temperature for 1T-TaS<sub>2</sub> by Mutka et. al.<sup>36</sup> The vertical scale above zero is 1000 times larger than the scale below zero to bring out details.

extrinsic semiconductor with impurity doping. This supports the view that more than a simple CDW is responsible for the low temperature ground state.

### 4.3.3 1T-TiSe<sub>2</sub>

The physical properties of 1T-TiSe<sub>2</sub> are very different from those of its Ta counterpart because Ti has one less *d*-electron. This has significant effects on the electronic structure. There has been much debate on whether 1T-TiSe<sub>2</sub> is a semi-metal or a small gap semiconductor and subsequent questions on the nature of the CDW mechanism<sup>24</sup>. 1T-TiSe<sub>2</sub> has only one commensurate CDW transition around 202 K. The CDW is of particular interest as it has a three dimensional characteristic of forming a 2x2x2 superlattice. The effect upon the reciprocal space Brillouin zone is shown in Figure 4-21. Under this reconstruction, the Brillouin zone is reduced to one eighth its former size.

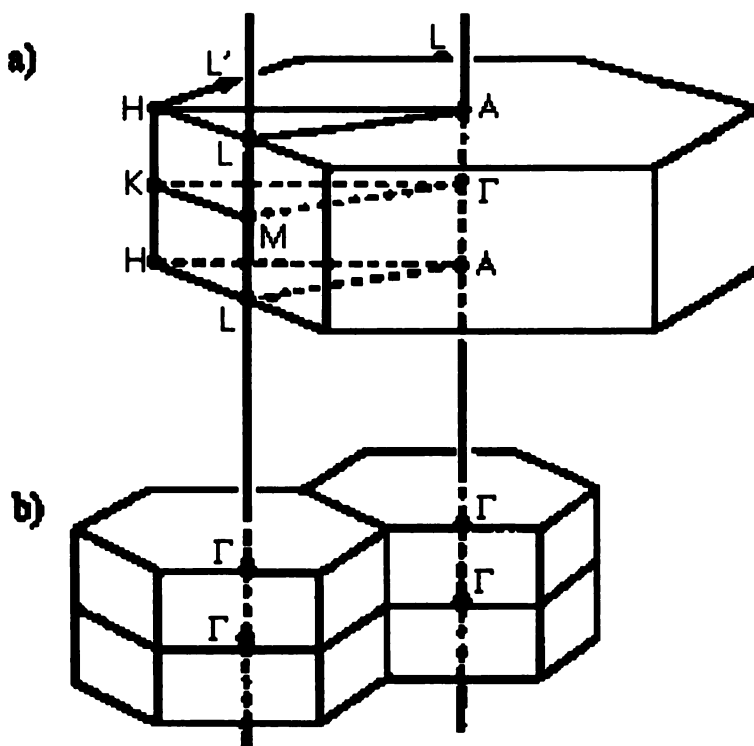


Figure 4-21: The reciprocal space reconstruction caused by a 2x2x2 superlattice.

### 4.3.3.1 Resistivity

Figure 4-22 shows the resistivity of 1T-TiSe<sub>2</sub> as a function of temperature.

Unlike 1T-TaS<sub>2</sub>, the transition is not a sharp, first order transition. This suggests a more complicated CDW mechanism than the Fermi surface nesting mechanism. An excitonic insulator model involving electron-hole interactions has been proposed for this material by Wilson and Mahajan<sup>37</sup>. This mechanism can cause a metallic material to become insulating under a CDW transition. Instead of the nesting of Fermi surfaces, this mechanism arises from a coupling of hole states to electron states to form excitons. This can occur as a specialized case of the Fermi surface nesting mechanism, if the nested surfaces are of opposite sort.

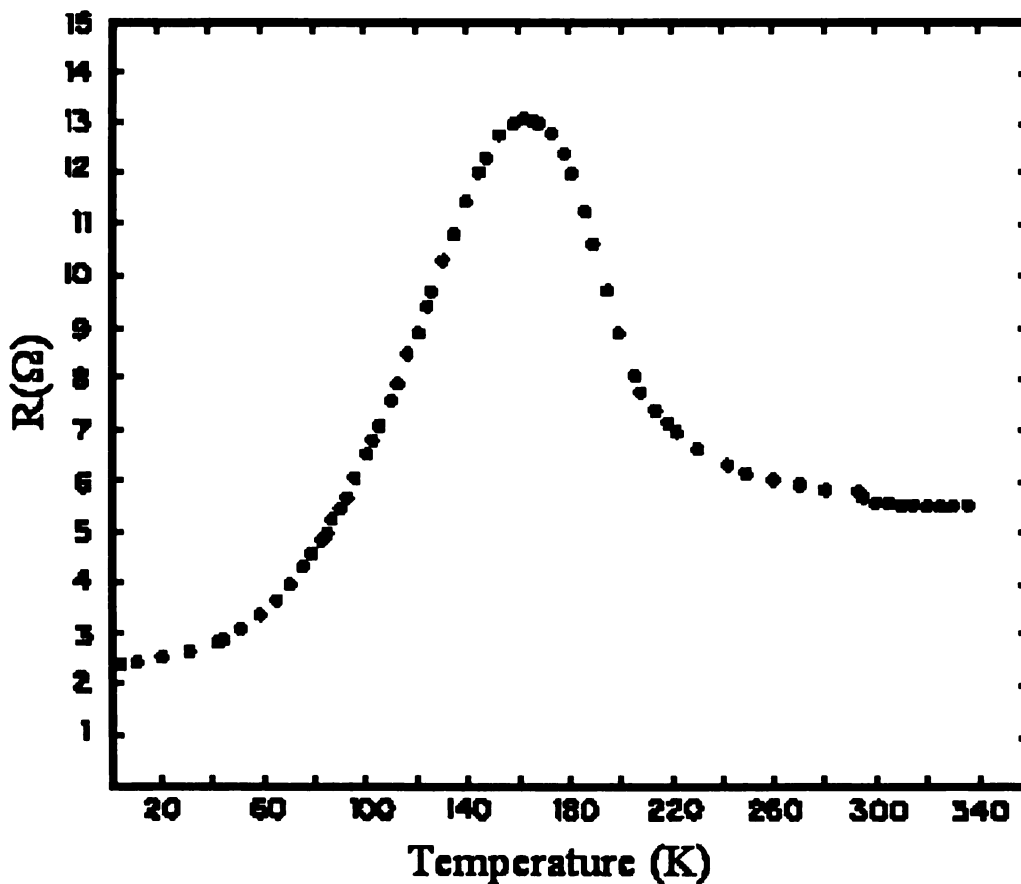


Figure 4-22: Resistivity data for 1T-TiSe<sub>2</sub> by R. V. Coleman et. al.<sup>38</sup>

### 4.3.3.2 Magnetic Susceptibility

The magnetic susceptibility for 1T-TiSe<sub>2</sub>, as shown in Figure 4-23, indicates the of the CDW transition clearly by a sharp change in slope. The maximum in this slope change is at 203K, at the detected transition temperature of 1T-TiSe<sub>2</sub>.

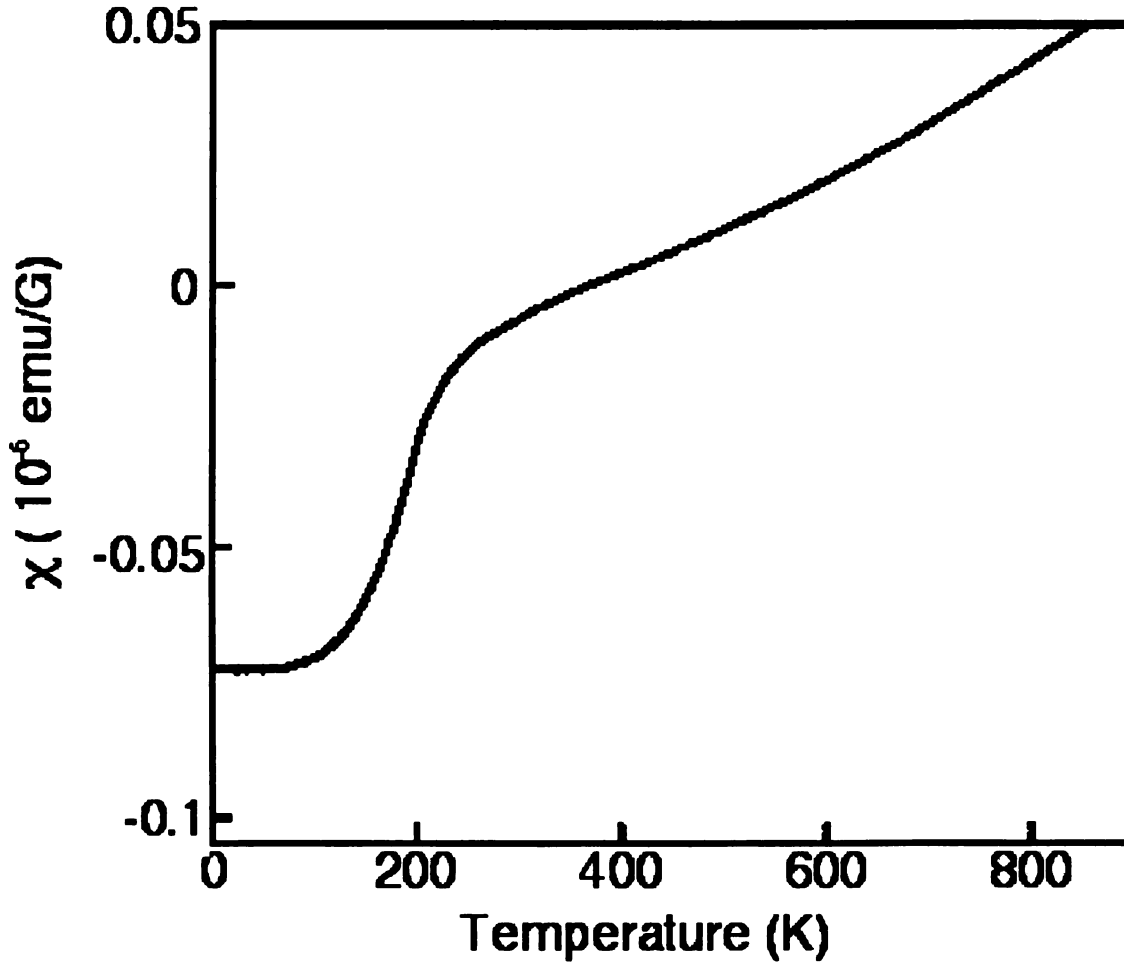


Figure 4-23: Magnetic susceptibility of 1T-TiSe<sub>2</sub> versus temperature, taken by Salvo et. al.<sup>39</sup>

### 4.3.3.3 Hall and Seebeck Coefficients

Both the Hall and Seebeck coefficients show a sign reversal near the onset of the CDW as seen in Figure 4-24. However, unlike the 2H materials, the signs are the same for both coefficients. Both coefficients change from positive to negative as the CDW transition is approached. This indicates a shift from hole like to electron like carriers.

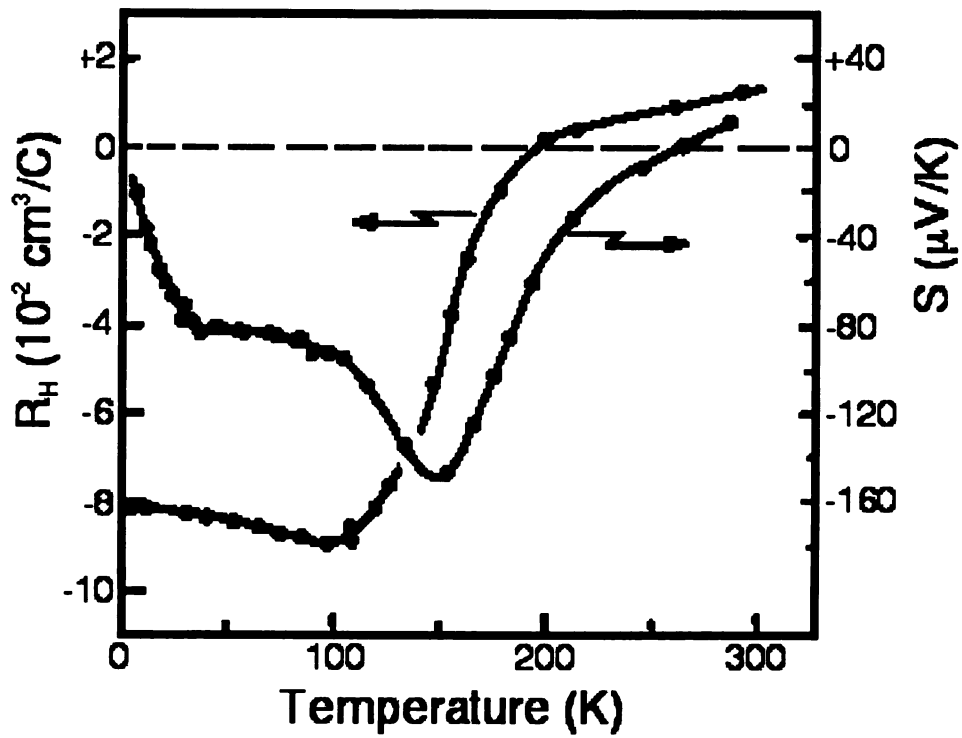


Figure 4-24: Hall and Seebeck coefficient by Salvo et al.<sup>39</sup>. They both become negative as the CDW develops with temperature decrease. The Hall scale is on the left axis; the Seebeck coefficient on the right.

## Chapter 5 Experimental Details

### 5.1 Sample Preparation

The 2H-TaSe<sub>2</sub> samples were provided by Professor Frindt from Simon Fraser University. The other samples were provided by Dr. Molinié at Nantes cedex in France. All samples were grown using the iodine vapor transport method. In general, the samples have a thin flake like morphology.

Single crystals of the 2H-TaSe<sub>2</sub>, 2H-TaS<sub>2</sub>, and 2H-NbSe<sub>2</sub> were grown from powder material directly synthesized from elements (99.95% pure Nb and Ta, 99.9995% pure Se, and 99.999% pure S). The samples were allowed to cool normally from the growth temperature of 1100 K to room temperature to solidify. Electrical resistivity measurements indicate incommensurate CDW transition temperatures of 122 K, 75.3 K, and 33.5 K<sup>40</sup> respectively. 2H-TaSe<sub>2</sub> undergoes a second transition into a commensurate CDW phase at 90 K, as expected from good quality samples.

Single crystals of 1T-TaS<sub>2</sub> were grown at 1100 K and quenched to room temperature to preserve the 1T polytype<sup>36</sup>. The starting powder material was directly synthesized from elements (99.95% pure Ta and 99.9999% pure S). Electrical resistivity measurements indicate an incommensurate CDW (I-CDW) to quasi-commensurate CDW (QC-CDW) transition temperatures of 352K. There is a hysteresis at the QC-CDW to commensurate CDW (C-CDW) transition. On cooling the transition is at 191 K and on warming it is at 209 K. Measurements of the Hall effect show the same transitions. The measured transition temperatures match the expectations for stoichiometric samples.

Single crystals of the material were grown using iodine vapor transport around 800 K. 1T-TiSe<sub>2</sub> does not need to be quenched to room temperature to preserve the 1T

polytype, since it only forms in the one polytype. The starting powder material was directly synthesized from elements with an excess of Se to provide a pure stoichiometry. Any impurities of off-stoichiometric samples are usually additional Ti atoms that occupy interstitial sites between layers. Electrical resistivity measurements indicate a broad commensurate CDW transition around 200 K.

X-ray Laue diffraction pictures were taken from the mounted samples prior to being entered into the chamber. The Laue diffraction pattern indicates the sample orientation, which can be used to mount the samples inside the chamber with a desired orientation. For hexagonal lattices, the Laue diffraction patterns give preferential emission from the  $\Gamma$ M line, allowing for direct determination of the sample orientation. The quality of the Laue diffraction patterns gives some information on sample quality.

Clean surfaces were obtained by cleaving the samples in a vacuum better than  $3 \times 10^{-11}$  Torr just before measurements. The samples were cut and mounted to sample holders using high vacuum epoxy, with a pin epoxied to the opposite face. Cleaving was achieved by knocking off the pin epoxied. Since the TMDs are layered materials, this usually results in a smooth surface.

The samples were attached to a copper arm, which was connected to a closed cycle helium refrigerator. This allowed the samples to be cooled to 20 K as needed. A resistor was used to heat the samples to as high as 250 K to attain the high temperature phases for some samples. The thermal expansion of the copper arm had to be accounted for when raising the temperature from 20 K. For the 1T-TaS<sub>2</sub> and 1T-TiSe<sub>2</sub> samples, the temperatures had to be raised to between 250 K and room temperature producing a thermal expansion of approximately 0.7 mm. For the 2H materials, the highest

temperature required was 130 K for 2H-TaSe<sub>2</sub>, producing only a 0.2 mm thermal expansion. Comparably, the photon spot was about 0.6 mm in diameter. Measurements were made both with and without the sample height adjusted to compensate the thermal expansion. The spectra were qualitatively similar but did show some intensity difference, part of which may be due to sample inhomogeneity and part of which may be due to slightly different surface alignment.

## 5.2 Photon Source

These ARPES measurements were carried out at the Ames-Montana ERG-Seya beam line at the Synchrotron Radiation Center (SRC), in Stoughton, Wisconsin. A schematic of the Aladdin storage ring and the beamline layout is shown in Figure 5-1. Electrons orbit around the storage ring at 800 MeV energy travelling at nearly the speed of light. Each time that the electrons' trajectory is bent by bending magnets, they emit light along the tangential direction of the trajectory. The emitted light contains a continuous spectrum of wavelengths. Monochromators are built at ports along the tangential emission directions to allow selection of photon energies for experiments. The ability to select photon energy in a continuous range is the main advantage of using a synchrotron light source versus using other lab sources such as a He lamp. In particular, probing the band dispersion along  $k_{\perp}$  direction in the normal emission geometry is only possible if a synchrotron light source is used. The light from a synchrotron source also has an advantage of being 60-70% linearly polarized.

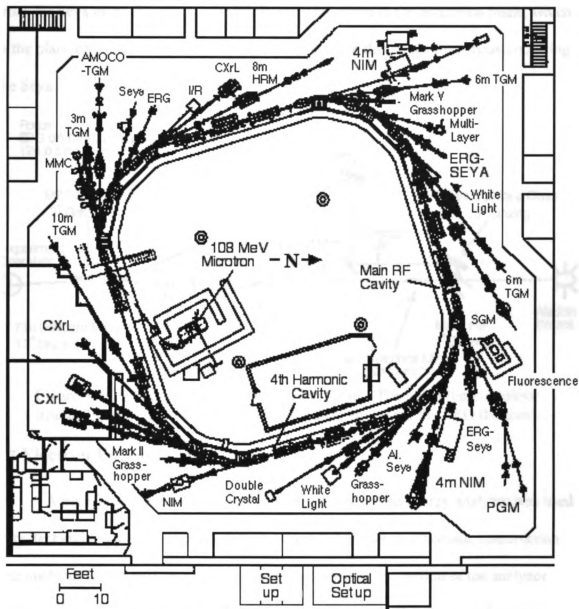


Figure 5-1: Synchrotron Radiation Center electron storage ring Aladdin. Focused light is emitted past the bending magnets and employed along beam lines. The beamlines are labeled by the type of monochromator used upon them.

The beamline primarily used in these experiments is the Ames/Montana's ERG-Seya, designed by C. G. Olson<sup>41</sup>. As shown in Figure 5-2, it combines an Extended Range Grasshopper (ERG) monochromator for high energy photons of 40-1500 eV with a Seya monochromator for 5-40 eV photons. Both monochromators use spherical gratings, with a design based on the focussing property of a Rowland's circle. The light

from the Seya monochromator is nearly linearly polarized in the horizontal plane, which is the plane of incidence. Most of the spectra present in this thesis were measured using the Seya.

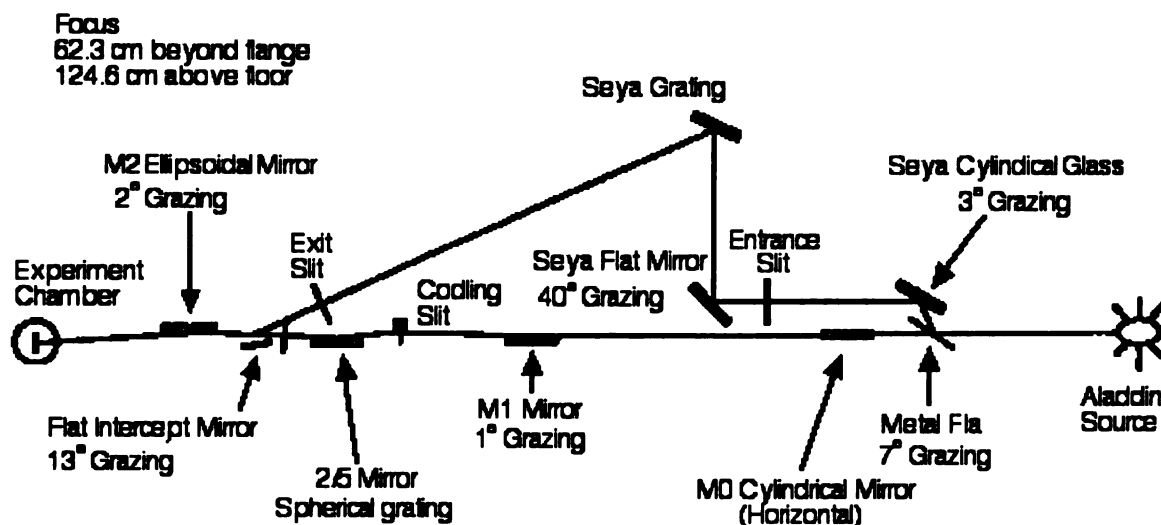


Figure 5-2: ERG-Seya combined monochromators. The metal flat is a mirror inserted into the photon beam to select the Seya (top) over the ERG (bottom).

### 5.3 Electron Energy Analyzer

A movable 50-mm mean radius hemispherical electron energy analyzer was used to collect and analyze the photoelectrons. Figure 5-3 shows its schematic construction. The analyzer is mounted on a goniometer that allows precise rotation of the analyzer about its focal point horizontally  $\sim 340^\circ$  and vertically  $\sim 40^\circ$ . The electrons first pass through a few focussing lenses at the entrance slit. They are then filtered by the electrostatic potential formed between the inner and outer spheres. The electrons that pass through the exit slit are collected by an electron multiplier. The electron and photon combined energy resolution of the spectrometer was 30 meV at 1.5 eV pass energy and 21 eV photon energy. The angular resolution of the electron analyzer was  $\pm 1^\circ$ , which

corresponds to a momentum resolution of  $0.07 \text{ \AA}^{-1}$  for measurements near the Fermi level at 21 eV photon energy.

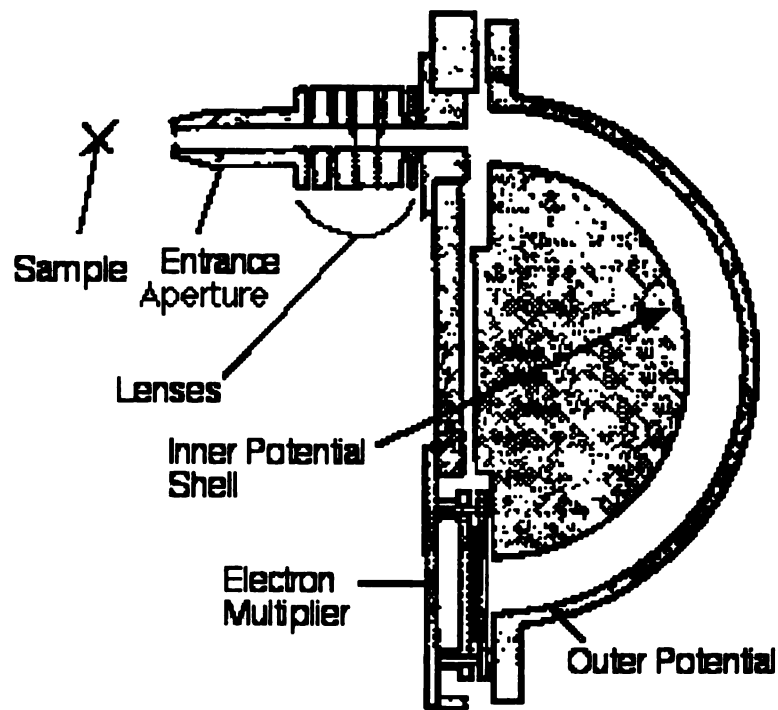


Figure 5-3: Hemispherical electron energy analyzer with focussing lenses. The inner and outer potential shells are set to specific voltages to allow only electrons with a desired energy to reach the electron multiplier to be pulse counted. The entrance aperture limits the accepted electrons to a small angle for angular resolution.

## Chapter 6 2H-TaSe<sub>2</sub>, 2H-TaS<sub>2</sub>, and 2H-NbSe<sub>2</sub>

As has been discussed, ARPES is a very useful tool for studying the electronic phase transitions in solids. In particular, high resolution ARPES studies of the high  $T_c$  superconducting cuprates have been very fruitful<sup>42</sup>. In contrast, the CDW materials have not been studied as thoroughly and need to be explored. Although there has been some ARPES study of 2H-TaSe<sub>2</sub> by Smith et al.<sup>43</sup> and Dardel et al.<sup>44</sup> with moderate energy and moderate angular resolution respectively, there were no high resolution studies of this group of materials prior to this work.

As discussed in Chapter 4, the CDW mechanism in 2H-TaSe<sub>2</sub>, 2H-NbSe<sub>2</sub> and 2H-TaS<sub>2</sub> is still not well understood<sup>45,46</sup>. Two different viewpoints have been put forward to explain the CDW. One of them is the Fermi surface (FS) nesting mechanism, either involving the FS around  $\Gamma$ <sup>47</sup> or the FS around K<sup>13</sup>. However, the FS nesting around  $\Gamma$  cannot explain the resistivity decrease in the CDW phase. In contrast, Rice and Scott<sup>28</sup> proposed a CDW mechanism which invokes saddle points on the FS. They showed that the susceptibility  $\chi(\mathbf{Q}_0)$ , where  $\mathbf{Q}_0$  is a wavevector connecting two saddle points, diverges logarithmically leading to a CDW instability. These saddle points act as scattering sinks in the normal state and their removal can reduce the resistivity.

In these high resolution ARPES experiments<sup>48,49,50</sup>, the band dispersions and Fermi surfaces were studied of 2H-TaSe<sub>2</sub>, 2H-NbSe<sub>2</sub> and 2H-TaS<sub>2</sub> in the normal and CDW states. The following results provide important insights on the CDW mechanism in this group of materials.

## 6.1 Band Dispersions and the Saddle Band

### 6.1.1 2H-TaSe<sub>2</sub>

Figure 6-1 a) shows the EDCs (solid lines) for  $k$ -points along  $\Gamma$ -K in the normal state at a temperature of 125 K for 2H-TaSe<sub>2</sub>. Note that, as  $k_x$  is increased from 0.34 to 0.42  $\text{\AA}^{-1}$ , the spectral weight at  $E_F$  increases significantly. This indicates that an energy band has just dispersed from above  $E_F$  to below  $E_F$ . Therefore,  $k_x=0.42 \text{\AA}^{-1}$  is a FS crossing point. As  $k_x$  is further increased, this band splits into two bands. One disperses below  $E_F$ ; the other stays very close to  $E_F$  for an extended region as illustrated by the vertical tick marks in Figure 6-1 a). As  $k_x$  is increased from 0.87 to 0.90  $\text{\AA}^{-1}$ , the spectral weight at  $E_F$  decreases, suggesting that  $k_x=0.87 \text{\AA}^{-1}$  is another FS crossing point. However, this FS crossing is not so obvious and it is also obscured by the deeper binding energy band approaching  $E_F$ . To determine the FS crossing points more accurately, the spectra were modeled by Lorentzian peaks multiplied by the Fermi-Dirac function and convolved with a Gaussian instrument resolution term. The best fits are shown as dashed lines in Figure 6-1 a). As can be seen, the modeled spectra reproduce the measured ones very well. The corresponding band dispersions are shown as the solid circles in Figure 6-1 b). In order to obtain a good fit at the higher binding energy region, an additional weak feature, whose binding energies are indicated by the crosses in Figure 6-1 b), is needed. The modeling shows that the two bands cross  $E_F$  at  $k_x = 0.87 \text{\AA}^{-1}$  and  $1.08 \text{\AA}^{-1}$  respectively. Because of the splitting of the two bands, the FS of 2H-TaSe<sub>2</sub> is double walled. As pointed out by Wexler and Woolley<sup>14</sup>, due to time-reversal symmetry, the double walled FS can be folded out into a single continuous FS in a double Brillouin zone scheme along the  $c$ -axis. Note that the low binding energy band is extremely close to  $E_F$ .

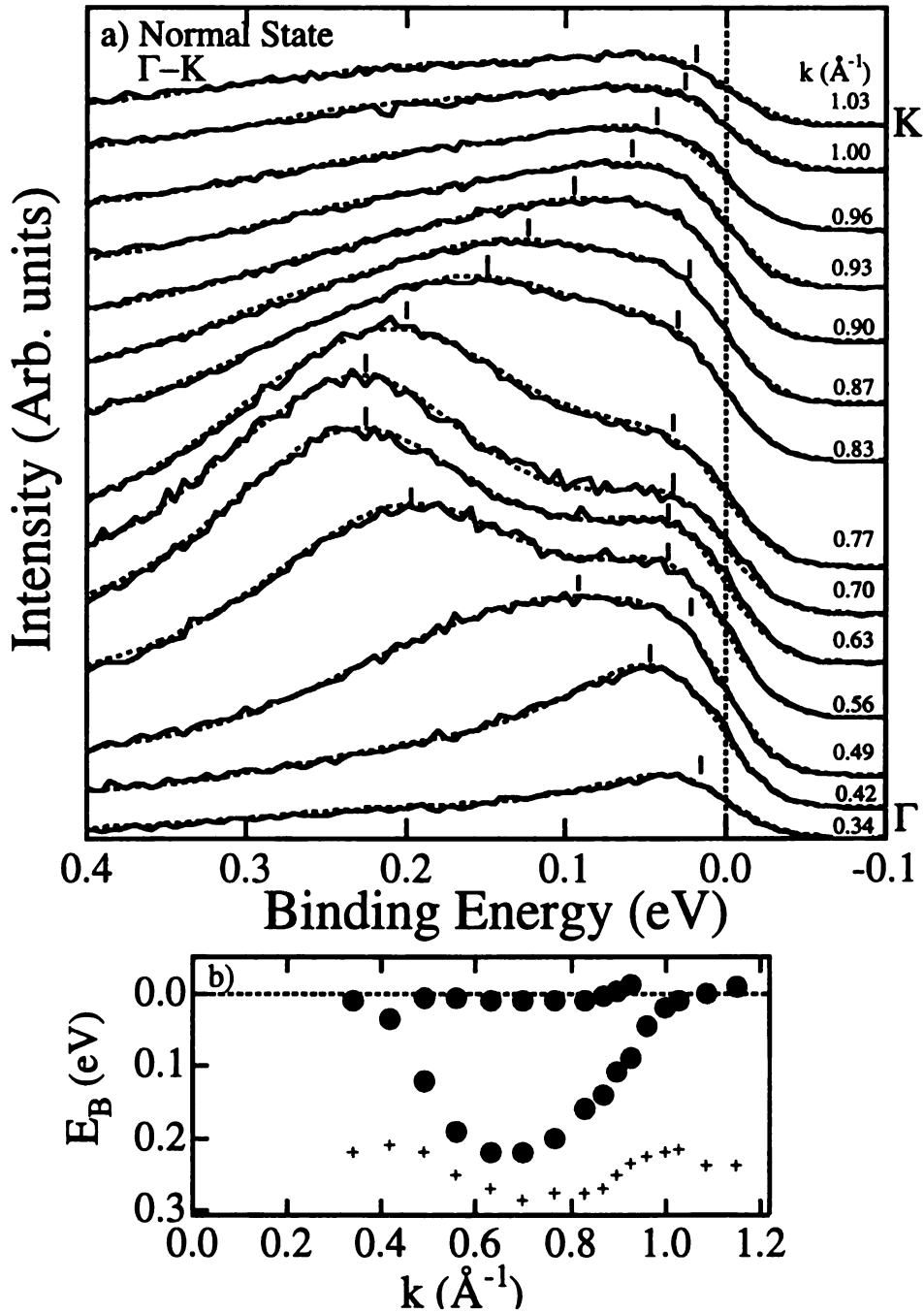


Figure 6-1: a) Normal state EDCs (solid lines) for the  $\Gamma$ -K line of 2H-TaSe<sub>2</sub> with modeled fits (dashed curve). The tick marks indicate the peak positions. b) The extracted band dispersions from a).

Figure 6-2 shows the EDCs of 2H-TaSe<sub>2</sub> in the normal state for  $k$ -points along two additional lines parallel to but slightly below  $\Gamma$ -K as shown in the inset. The  $k_x$ - and  $k_y$ -values marked along each curve in  $\text{\AA}^{-1}$ , are selected to be the momentum components parallel and perpendicular to  $\Gamma$ -K, respectively. The band dispersions of these lines have

a general trend similar to those along  $\Gamma$ -K. Well defined Fermi crossings can be observed at  $(k_x, k_y) = (0.36, -0.07)$  and  $(0.33, -0.15)$  in Figure 6-2 a) and b), respectively. These Fermi crossings, along with the one at  $(k_x, k_y) = (0.44, 0)$ , form a Fermi surface locus disperses significantly below  $E_F$  in the mid-range, as indicated by the vertical dashes. As

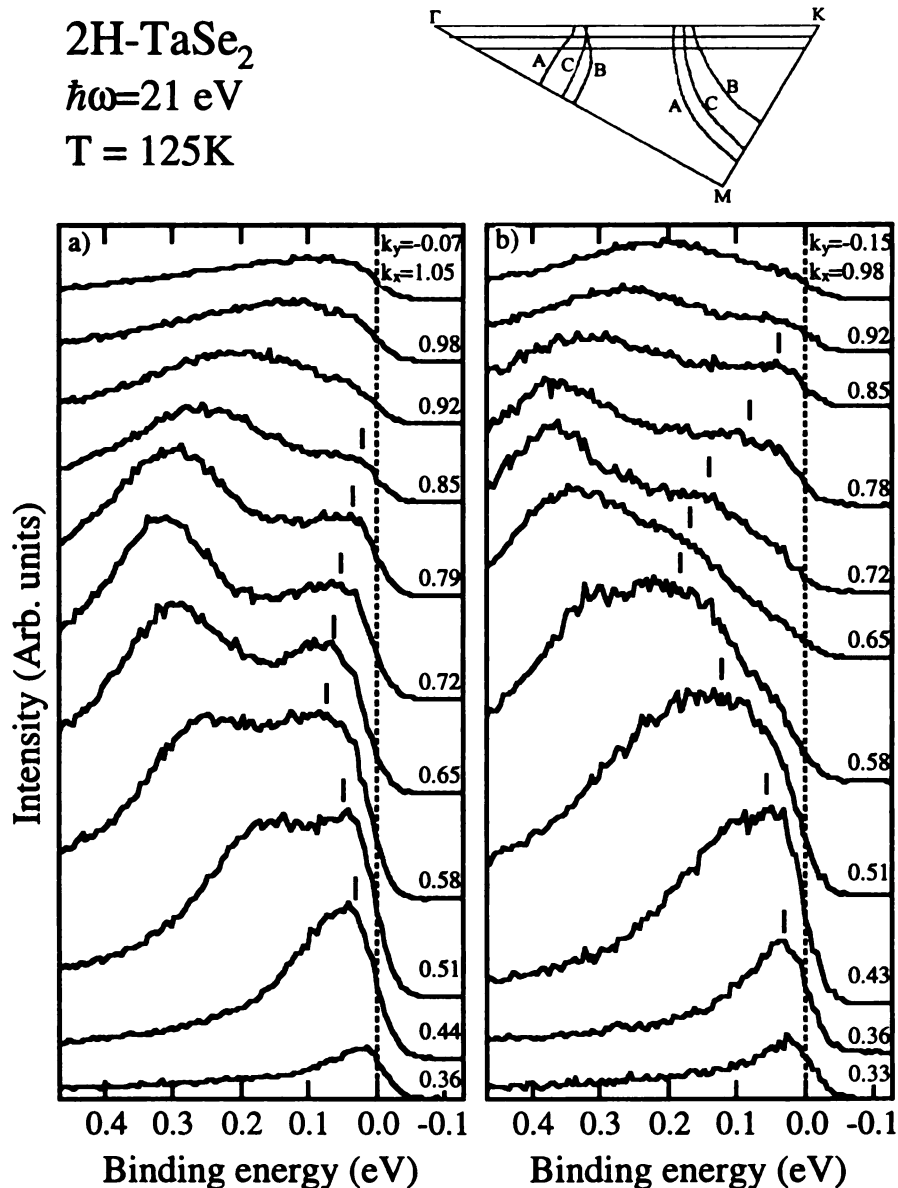


Figure 6-2: Energy distribution curves (EDCs) in the normal state ( $T=125$  K), for  $k$ -points along two lines parallel to  $\Gamma$ -K at a)  $k_y = -0.07$  and b)  $-0.15 \text{ \AA}^{-1}$ . The inset of the Brillouin zone's irreducible wedge (top) shows the amount of  $k_z$ -dispersion of the Fermi surfaces predicted by band calculations<sup>14</sup> (A:  $k_z = 0$ ; B:  $k_z = 2\pi/c$ ; C:  $k_z = \pi/c$ ) and the lines of a) and b).

the band disperses back toward  $E_F$ , it appears to cross  $E_F$  at  $(k_x, k_y) = (0.85, -0.07)$ . In Figure 6-2 b) where  $k$ -points are along a line further away from  $\Gamma$ -K, the band disperses even further below  $E_F$  in the mid-range, and appears to cross  $E_F$  at  $(k_x, k_y) = (0.85, -0.15)$ . The second Fermi crossings in Figure 6-2 a) and b) are more obvious than the one in Figure 6-1 because the band has a finite dispersion. The fact that this band stays close to  $E_F$  for an extended region along  $\Gamma$ -K and disperses below  $E_F$  in the direction perpendicular to  $\Gamma$ -K in the mid-range suggests that it is an *extended saddle band*. As will be discussed, this extended saddle band places an important role in the CDW formation of this material.

### 6.1.2 2H-TaS<sub>2</sub>

The 2H-TaS<sub>2</sub> samples produced ring or arc Laue diffraction patterns, indicating some distribution of crystal orientations. As a result, the samples were mounted with unknown orientations. The ARPES spectra taken from those samples show distinct angular dependence and clear band dispersions, but the directions were not clear enough to probe the  $\Gamma$ -K line for saddle band behavior. The clear band dispersions suggest that there is a stacking disorder, which gives misaligned layers, but that the depth probed by the ARPES has a unique orientation. Further experiments using *in-situ* low energy electron diffraction (LEED) to determine the surface crystal orientation were attempted to rectify this situation, but the resulting signal was too low to help.

### 6.1.3 2H-NbSe<sub>2</sub>

Shown in Figure 6-3 are the EDCs for 2H-NbSe<sub>2</sub> taken in the normal state ( $T=40$  K) for  $k$ -points a) along  $\Gamma$ -K and b) along a line perpendicular to  $\Gamma$ -K, on a line intersecting it at approximately the midpoint, as shown in the insets. Along  $\Gamma$ -K, two

bands are observed dispersing below  $E_F$ . They both reach maximum binding energies at approximately the midpoint of  $\Gamma$ -K. As can be seen in Figure 6-3 b), both bands disperse

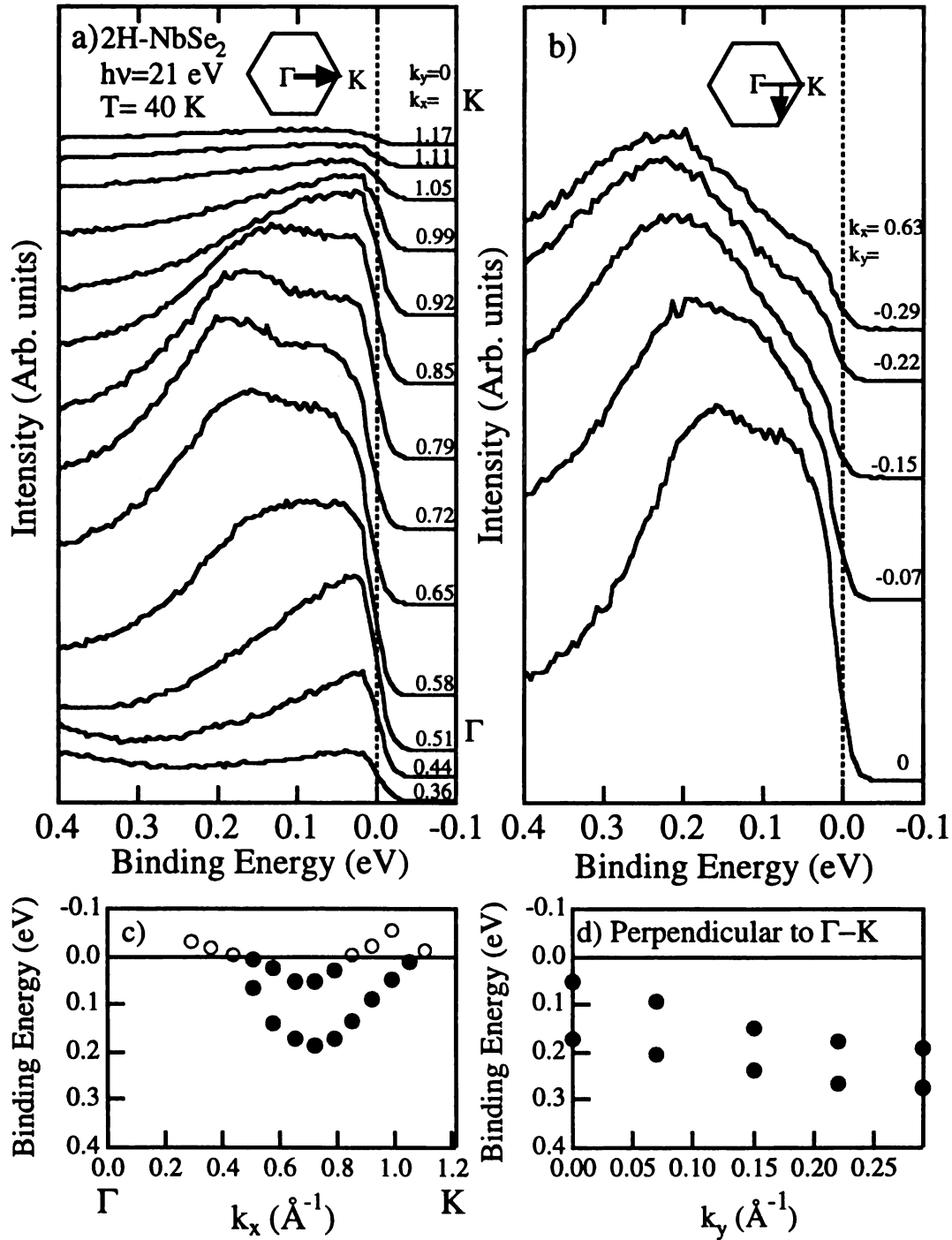


Figure 6-3: EDCs for 2H-NbSe<sub>2</sub> for  $k$ -points a) along  $\Gamma$ -K and b) along a line perpendicular to  $\Gamma$ -K intersecting it at approximately the midpoint, as shown in the insets. c) and d) Band dispersions (symbols) determined by modeling the spectra in a) and b), respectively.

toward higher binding energies in the orthogonal direction away from the  $\Gamma$ -K line, indicating their saddle band nature.

To determine the energy versus momentum relations for 2H-NbSe<sub>2</sub>, modeling was used. The results are shown as symbols in Figure 6-3 c) and d). Along  $\Gamma$ -K, the lower and higher binding energy bands have maximum binding energies of 0.055 eV and 0.187 eV respectively. Two things are of note. While the dispersion trend is similar to that in 2H-TaSe<sub>2</sub>, the lower binding energy band has a greater maximum binding energy than that of the corresponding band in 2H-TaSe<sub>2</sub>. Similarly, the higher binding energy band has a smaller maximum binding energy than that of the corresponding band in 2H-TaSe<sub>2</sub> (0.22 eV maximum binding energy).

## 6.2 Fermi Surfaces

### 6.2.1 2H-TaSe<sub>2</sub>

EDCs were measured for  $k$ -points in the entire Brillouin zone for 2H-TaSe<sub>2</sub>. By observing where bands cross  $E_F$ , the Fermi surface is determined, as summarized in Figure 6-4 as shaded and open circles. The open triangle along  $\Gamma$ -K indicates the second Fermi crossing determined from the modeling as shown in Figure 6-1 b) which corresponds to the inner wall of the FS around the K point. Because the two walls of the double walled FS are very close to each other, it is difficult to determine both walls accurately by just visually inspecting the EDCs. Only one set of the doubled walled FS was determined and shown for the other parts of the Brillouin zone. The size of the circles corresponds approximately to the experimental  $k$ -resolution. The data in the wedge bounded by the two dashed lines are original; the rest are obtained by a six-fold rotational symmetry operation. Note that the data join smoothly at the borders between

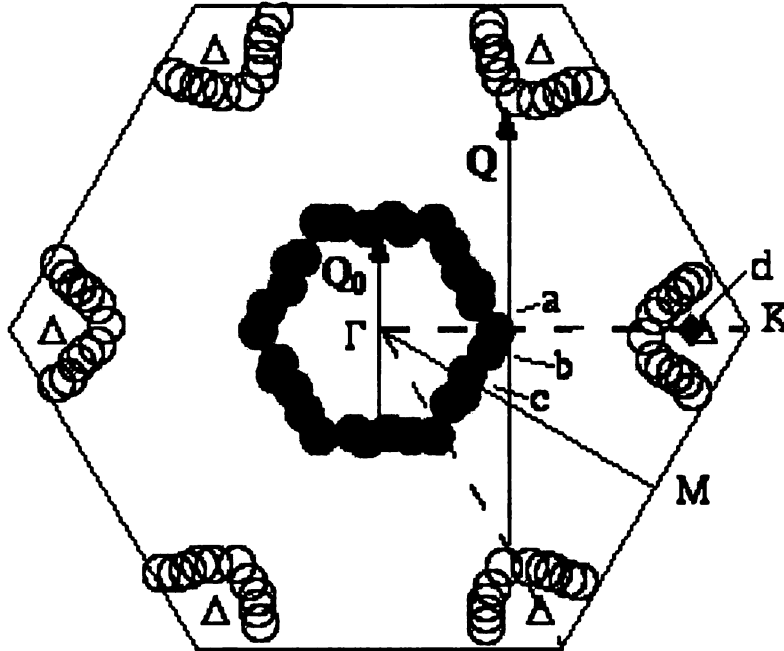


Figure 6-4: The Fermi surface cylinders (shaded and open circles) of 2H-TaSe<sub>2</sub> determined from the EDCs. The open triangle is the second wall seen along  $\Gamma$ -K. Points *a*, *b*, and *c* are shown in Figure 6-10. Point *d* (diamond) was used for the temperature dependence of the gap shown in Figure 6-11.

the rotated segments, which reassures the validity of the symmetry operation. As can be seen, the shaded circles form a near hexagon centered at the  $\Gamma$  point; the open circles form a pocket centered at the K point. The FS topology was also investigated by measuring the intensity map at  $E_F$ , which can be considered as a two-dimensional cut of the FS. The resulting  $E_F$  intensity map for the normal state of 2H-TaSe<sub>2</sub> is shown in Figure 6-5, presented in a linear gray scale (bright for high intensity). The intensities were measured with 21eV photons and were normalized to the photon flux. One sixth of the map was measured in each case as shown by the dashed wedge in Figure 6-5; the rest were obtained by a mirror operation about  $\Gamma$ -K, then a three-fold rotational symmetry operation. Note that there is a lack of symmetry between the  $\Gamma$ -K line and  $\Gamma$ -K' line at 60° with respect to it. This is partially caused by the unequal matrix elements of the two lines resulting from the horizontal photon polarization and plane of incidence which

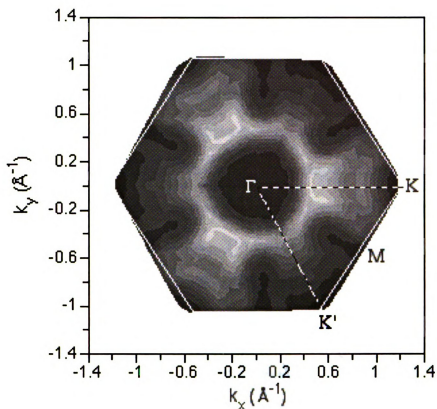


Figure 6-5: Fermi level intensity map of 2H-TaSe<sub>2</sub>. Bright regions indicate greater intensity. The data between the dashed wedge were actually measured and symmetrized to give the rest of the Brillouin zone.

contains  $\Gamma$ -K, and partially caused by the finite escaping depth of the photoemission process<sup>51</sup>.

The 2H-TaSe<sub>2</sub> intensity map shows a bright ring around the  $\Gamma$  point, indicating a FS locus. There is also a somewhat faint bright arc surrounding the K point, indicating another FS locus. The extended bright regions along  $\Gamma$ -K are caused by the extended saddle band near  $E_F$  as discussed previously. The FS locus around the  $\Gamma$  point has a rounded, three fold symmetry which is not aligned with the Brillouin zone. This is in contrast to the near hexagon shape in the FS determined from the EDCs. This difference may be due the overlap of the two walls of the FS distorting the apparent shape of the cylinder.

### 6.2.2 2H-TaS<sub>2</sub>

The  $E_F$  intensity map of 2H-TaS<sub>2</sub> shown in Figure 6-6 has the same qualitative features as 2H-TaSe<sub>2</sub>. Here, the contour around K appears to have the double-wall structure, and the contour around  $\Gamma$  does have an apparent, but distorted hexagon shape. In this case, the raw data were rotated to correct for the sample misalignment prior to the symmetry orientation. This generated the wide swath of intensity along the  $\Gamma$ -K line for better comparison with the other materials. The breadth of the saddle band and the distortion of the hexagonal shape of the FS cylinder around  $\Gamma$  may well be from a misadjustment of the data set's orientation.

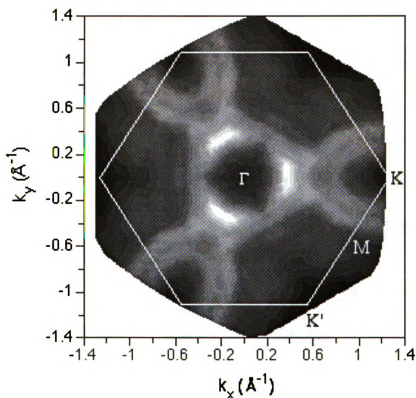


Figure 6-6: Fermi level intensity map of 2H-TaS<sub>2</sub>. The data were measured on one sixth of the Brillouin zone, rotated to give a comparable orientation to the other materials, and then symmetrized.

### 6.2.3 2H-NbSe<sub>2</sub>

For 2H-NbSe<sub>2</sub>, the  $E_F$  intensity map in Figure 6-7 shows a bright ring around  $\Gamma$

and another one around K. This FS pattern is qualitatively consistent with the band structure calculation results<sup>14</sup>. The double walls of the FS were not resolved here, although Straub et al.<sup>52</sup> used a two-dimensional gradient to distinguish them. The bright strip along  $\Gamma$ -K between the two FS pockets arises from the saddle band. The FS pocket around  $\Gamma$  is nearly hexagonal with a three-fold degenerate self-nesting wavevector along the  $\Gamma$ -M direction indicated by the arrow. The magnitude of the nesting wavevector is estimated from the middle of the bright contour on one side of the hexagon to that of the opposite side. An estimation of error is based upon the blurred appearance of the contour. The direction and the magnitude ( $0.68 \pm 0.27 \text{ \AA}^{-1}$ ) of the nesting wavevector are consistent with those of the observed CDW wavevector<sup>53</sup>.

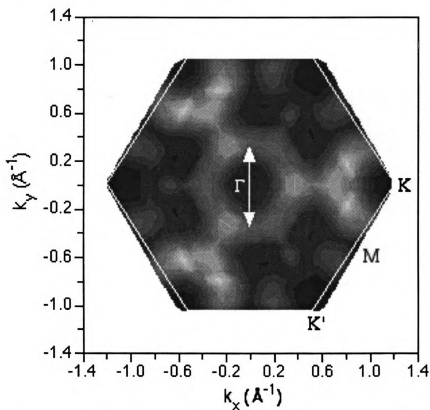


Figure 6-7: Fermi level intensity map of 2H-NbSe<sub>2</sub>. The arrow indicates a nesting vector of the same direction and magnitude as the CDW wavevector.

## 6.3 Energy Gap in the CDW State

### 6.3.1 2H-TaSe<sub>2</sub>

The formation of a CDW usually opens an energy gap at the Fermi energy and truncates parts of the FS that are connected by the CDW modulation's wavevector. In both 2H-TaSe<sub>2</sub> and 2H-NbSe<sub>2</sub>, there appears to be a nesting vector  $\mathbf{Q}_0$  that spans the FS cylinder around  $\Gamma$ . The nesting vectors for each material are shown in Figure 6-4 and Figure 6-7 respectively. Straub et al. suggest that the nesting of this FS is the cause of the CDW formation in 2H-NbSe<sub>2</sub><sup>52</sup>. However, this mechanism should result in a very strong resistivity increase instead of the decrease measured in experiments<sup>9,27</sup>. To make a thorough investigation of the CDW mechanism in these materials, the energy gap dependence on  $k$ -point was studied by measuring EDCs in the normal and CDW states at specific  $k$ -points.

Figure 6-8 shows the EDCs along  $\Gamma$ -K for 2H-TaSe<sub>2</sub> in the commensurate CDW state at 20 K with solid lines and the normal state at 250 K with dashed lines. Both sets of EDCs were measured in terms of the unreconstructed  $1 \times 1$  Brillouin zone. It can be seen that the CDW-induced spectral changes are highly  $k$ -dependent. At  $(k_x, k_y) = (0.44, 0) \text{ \AA}^{-1}$ , which is a Fermi surface crossing point, the change near  $E_F$  is relatively small. The leading edge is slightly sharper at low temperature, which can be accounted for by the reduced thermal broadening. The Fermi level remains above the mid-point of the leading edge, indicating that the CDW-induced energy gap is very small or near zero. For  $(k_x, k_y)$  beyond  $(0.44, 0)$ , the spectral changes are much more dramatic. Note that the leading edges shift significantly toward higher binding energies at low temperature, indicating the removal of electronic states from the Fermi level. At some  $k$ -points, such

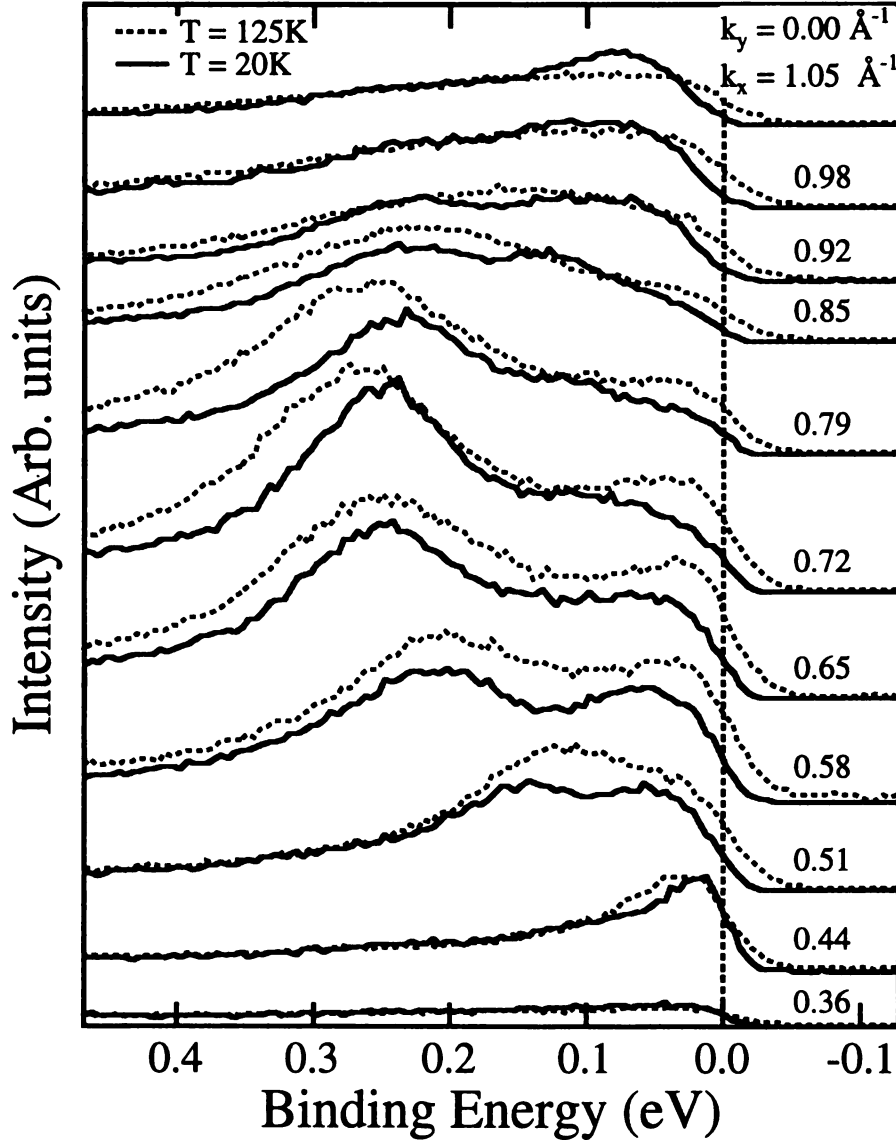


Figure 6-8: EDCs in the commensurate CDW state ( $T=20$  K, solid curves) of  $2H\text{-TaSe}_2$ , for  $k$ -points along  $\Gamma$ -K. The EDCs in the normal state are superimposed as dashed curves for comparison.

as  $(k_x, k_y) = (0.85, 0)$ ,  $(0.92, 0)$ ,  $(0.98, 0)$ , and  $(1.05, 0) \text{ \AA}^{-1}$ , weak additional spectral features appear at higher binding energies, indicating band splitting. Doran and Woolley<sup>54</sup> performed band calculations on the  $3 \times 3$  CDW superlattice and predicted similar band splitting. During this experiment, measurements were repeated several times as the sample went through temperature cycles between 20 K and 125 K. The spectra were reproducible and no surface degradation was detected. The spectra were

qualitatively similar but did show some small intensity difference, part of which may be due to sample inhomogeneity and part of which may be due to slightly different surface alignment.

To quantify the momentum dependence of the energy gap, the energy shift between the leading edge midpoints in the normal and CDW state was measured. Different methods of determining the gap might change the numbers slightly, but will not change the curve shape. The energy shift as a function of  $k_x$  along  $\Gamma$ -K is plotted in Figure 6-9. Strictly speaking, a gap can be defined only on the Fermi surface. Here, the term “gap” is also used for the extended saddle band region, since there are states near  $E_F$  at those  $k$ -points which are affected by the CDW formation. As can be seen, the energy shift is near zero at  $k_x = 0.44 \text{ \AA}^{-1}$ , which is a Fermi crossing point. It increases to finite along  $\Gamma$ -K, the energy shift remains large comparable to the gap at  $k_x = 1.05 \text{ \AA}^{-1}$ , but the spectral intensity at  $E_F$  diminishes. A finite energy gap of up to 25 meV wide is observed

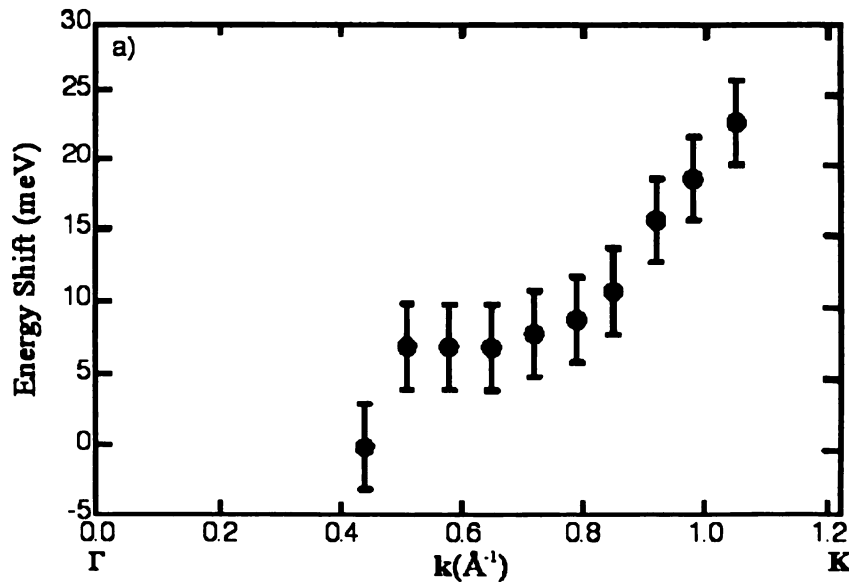


Figure 6-9: The energy shift vs.  $k_x$  along  $\Gamma$ -K of 2H-TaSe<sub>2</sub>. The energy shift is taken as the binding energy difference of the leading edge midpoints in the normal and CDW state spectra.

in the extended saddle band region and on the FS around K.

To confirm the effects of the CDW on the FS around the  $\Gamma$  point, this comparison of the normal and CDW state EDCs was made for several points on the cylinder. Figure 6-10 shows the EDCs for three FS crossing points, labeled as *a*, *b*, and *c* in Figure 6-4.

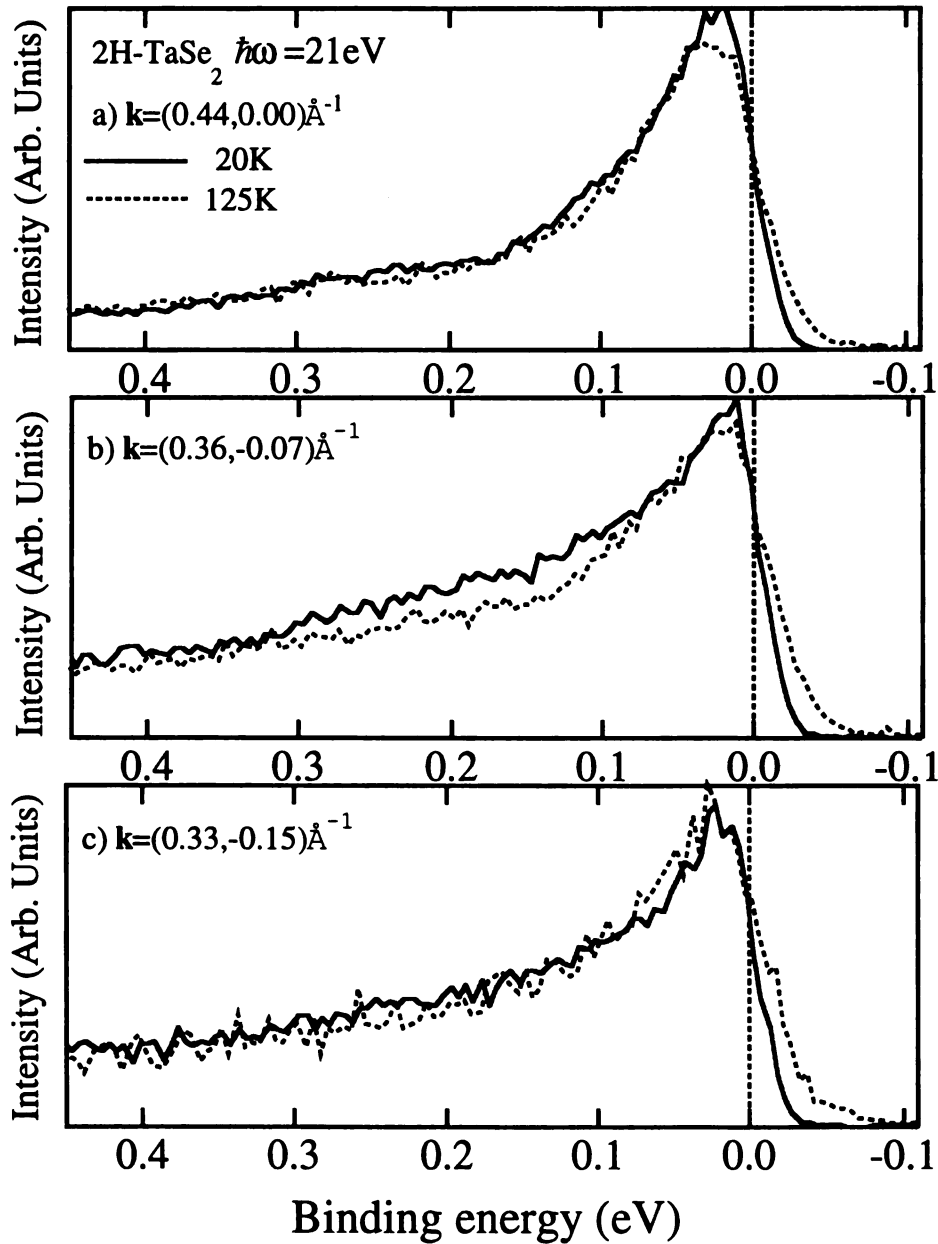


Figure 6-10: EDCs for three FS crossing points of 2H-TaSe<sub>2</sub>, labeled as *a*, *b*, and *c* in Figure 6-4. The solid and dashed lines are spectra measured in the CDW ( $T=20$  K) and normal ( $T=125$  K) states respectively.

Point  $c$  is on  $\Gamma$ -M, the direction of the CDW wavevector. The solid and dashed lines are spectra measured in the CDW ( $T=20$  K) and normal ( $T=125$  K) states respectively. As can be seen, the spectral changes are very small at these  $k$ -points. The leading edges are slightly sharper at low temperature due to reduced thermal broadening. The Fermi level, indicated by the vertical dashed lines, remains at the upper portion of the leading edges, indicating a sharply peaked density of states at  $E_F$  and hence nearly zero energy gaps. Thus, the FS centered at the  $\Gamma$  point is not gapped, despite the apparent nesting vector  $Q_0$ .

The temperature dependence of the gap in the extended saddle band region along  $\Gamma$ -K is of some interest as it can give information on the nature of the CDW mechanism. Figure 6-11 a) shows the spectral dependence on temperature for  $(k_x, k_y)=(1.05, 0.00)\text{\AA}^{-1}$  labeled as  $d$  in Figure 6-4. At this  $k$ -point, the shallow band has just crossed  $E_F$  and the deeper band is about to cross  $E_F$ . The normal state spectrum taken at  $T=125$  K is superimposed on each curve as the dashed lines for comparison. As can be seen, there is significant spectral weight at  $E_F$  in the normal state. As the temperature is lowered below the incommensurate CDW transition temperature ( $T_0=122$  K), the spectral weight at  $E_F$  is suppressed and the leading edge midpoint shifts toward higher binding energies, indicating the opening of an energy gap. The temperature dependence clearly shows that the spectral changes are related to the CDW transition.

Figure 6-11 b) shows the midpoint energy shifts as a function of temperature. The energy shift decreases for increasing temperature and approaches zero near  $T_0=122$  K. The decreasing rate appears to be faster than the Bardeen-Cooper-Schrieffer (BCS) relation (solid line) of the weak coupling limit of the superconducting gap to temperature

is. There is no apparent anomaly near the commensurate transition at  $T_1=90$  K. Further theoretical work would help clarify what basis there is for this deviation from the weak coupling limit.

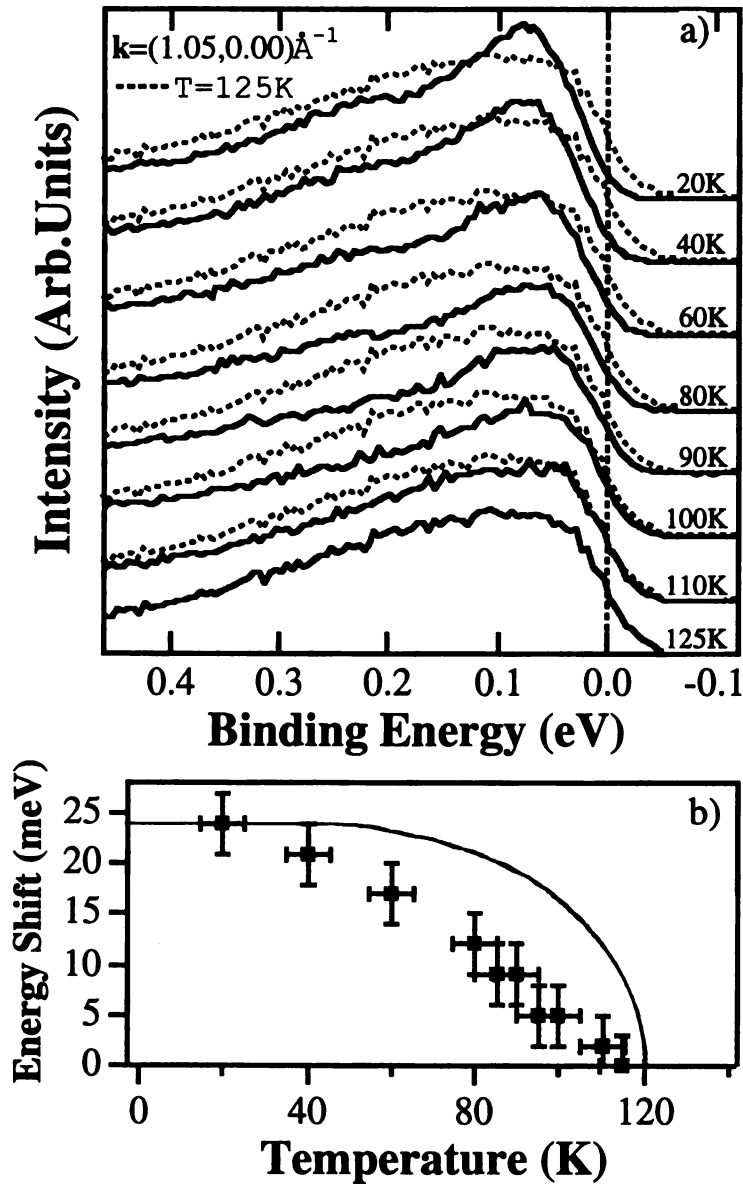


Figure 6-11: a) EDCs for point *d* in Figure 6-4 in the vicinity of the extended saddle band of 2H-TaSe<sub>2</sub>, measured at various temperatures. The normal state spectrum is superimposed on each curve as dashed lines for comparison. b) The energy shifts of the leading edge midpoint (solid squares) as a function of temperature. The solid line is the BCS relation.

### 6.3.2 2H-TaS<sub>2</sub>

Shown in Figure 6-12 a) are the EDCs measured on a 2H-TaS<sub>2</sub> sample in the normal (T=80 K, dashed lines) and CDW (T=20 K, solid lines) states. The spectra were normalized to photon flux. The corresponding *k*-points are along a line at approximately

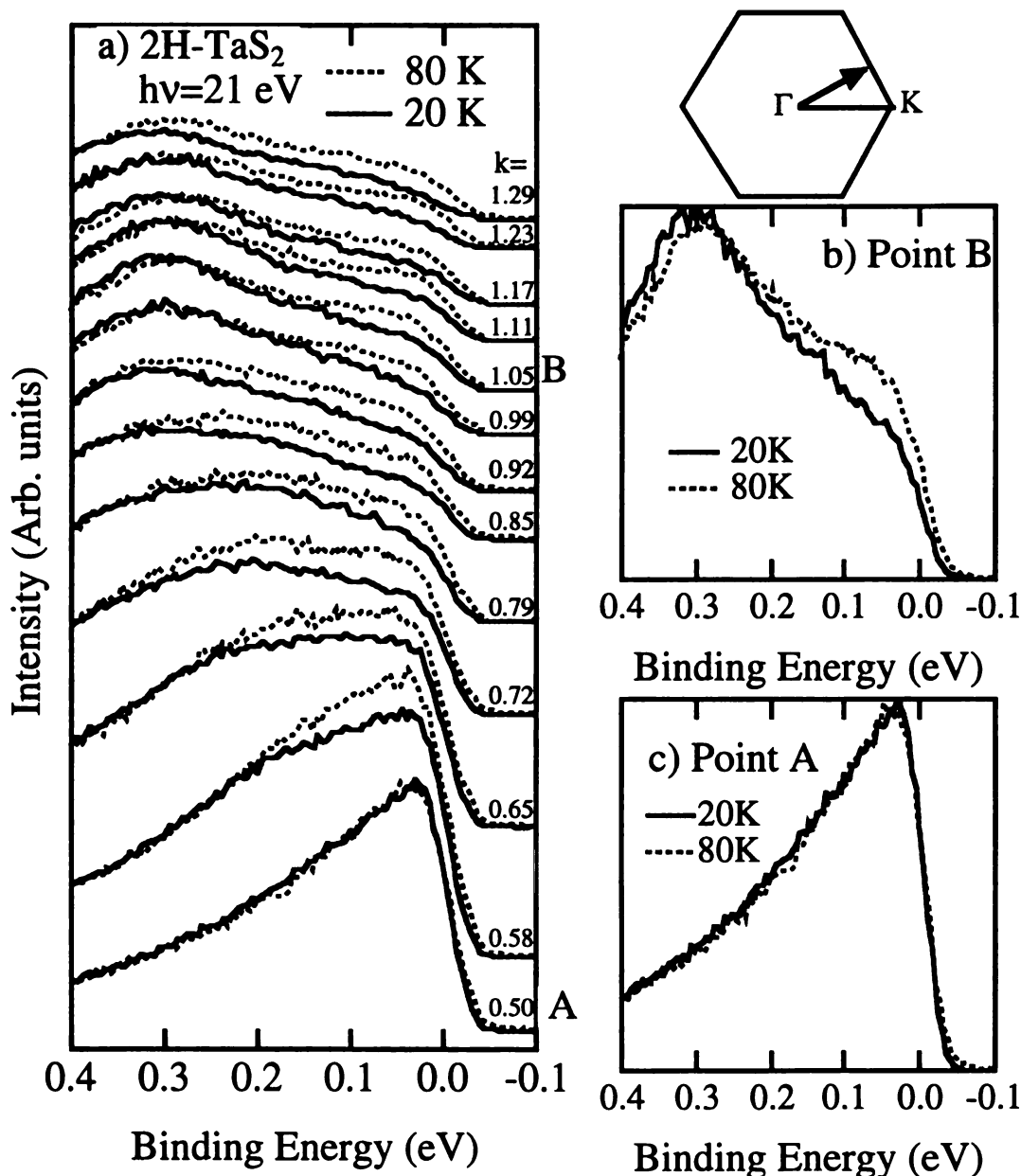


Figure 6-12: a) EDCs for 2H-TaS<sub>2</sub> measured in the normal (T=80 K, dashed lines) and CDW (T=20 K, solid lines) states, along a line at approximately 36° with respect to  $\Gamma$ -K, as shown (inset). Enlarged spectra at point A and B are reproduced in c) and b) respectively.

36° with respect to  $\Gamma$ -K, as shown in the inset. At point A, the enlarged spectra Figure 6-12 c), which is a point on the FS around  $\Gamma$ , there is no apparent energy shift between the leading edges at the two temperatures, indicating a nearly zero energy gap. For  $k$ -points beyond A such as point B in Figure 6-12 b), the midpoint of the leading edge shifts toward higher binding energies (up to 20 meV) at the lower temperature, indicating a finite energy gap. Note that, in addition to the leading edge shift, the spectral intensity also decreases in the energy range between zero and 0.3 eV binding energies at the lower temperature. This might be due to the electronic structure change in addition to the opening of a gap.

### 6.3.3 2H-NbSe<sub>2</sub>

Figure 6-13 shows the EDCs for 2H-NbSe<sub>2</sub> measured at temperatures above (dashed lines) and below (solid lines) the CDW transition for some  $k$ -points along  $\Gamma$ -K. These spectra were taken at the Undulator-NIM beam line using a Scienta SES200 hemispherical analyzer for better resolution. The energy resolution was 24 meV; and the angular resolution was 0.7° corresponding to a momentum resolution of 0.026 Å<sup>-1</sup> for 21-eV photons. There is no apparent indication of a gap at any  $k$ -point, including the Fermi crossing around  $\Gamma$  and the saddle band region. Since the CDW transition temperature is relatively low in this material, the energy gap is expected to be small. ARPES studies with higher energy resolution are needed in order to study the gap properties.

## 6.4 Summary and Discussion

In summary, the normal and CDW state electronic structures of 2H-TaSe<sub>2</sub>, 2H-NbSe<sub>2</sub> and 2H-TaS<sub>2</sub> were studied using high resolution ARPES. The essential electronic structure properties are similar within this family of materials. The Fermi surfaces

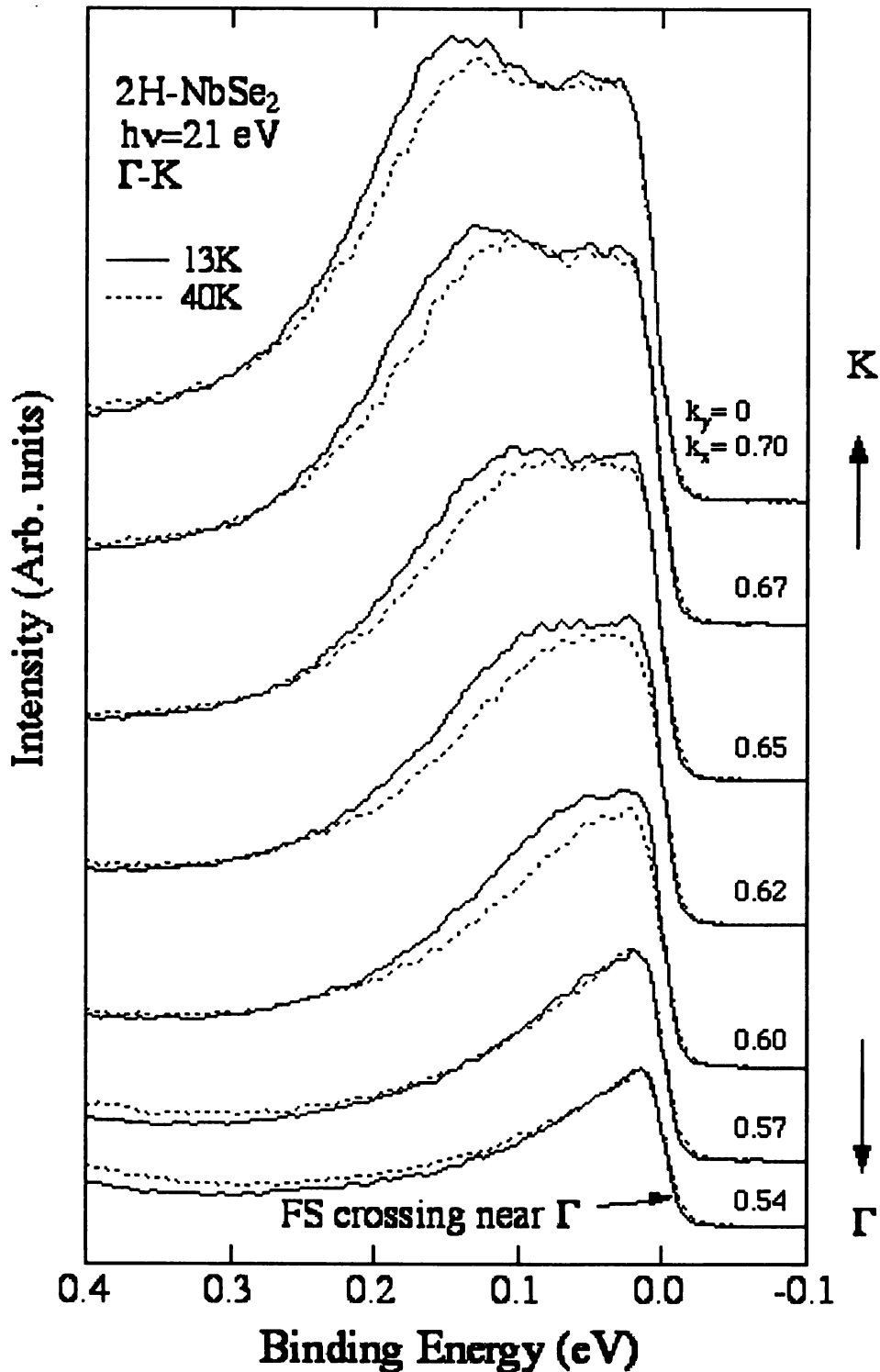


Figure 6-13: EDCs for 2H-NbSe<sub>2</sub> along  $\Gamma$ -K measured in the normal ( $T=40$  K, dashed lines) and CDW ( $T=13$  K, solid lines) states. The bottom curve is for a  $k$ -point on the Fermi surface around  $\Gamma$  while the other spectra are in the saddle band region.

consist of a pocket around  $\Gamma$  and another one around K which are in excellent agreement with the band calculation results by Wexler and Woolley<sup>14</sup>. In 2H-TaSe<sub>2</sub>, the Fermi surface pocket around  $\Gamma$  has an apparent hexagon shape. For 2H-NbSe<sub>2</sub> and 2H-TaSe<sub>2</sub>, the FS pocket around  $\Gamma$  is nearly hexagonal with a three-fold degenerate nesting wavevector along the  $\Gamma$ -M direction whose magnitude corresponds well with that of the observed CDW wavevectors. The nesting conditions are not as apparent in 2H-TaS<sub>2</sub>, due to the orientation problem of the samples available.

A saddle band was clearly observed in 2H-TaSe<sub>2</sub> and 2H-NbSe<sub>2</sub> near  $E_F$  along  $\Gamma$ -K with a saddle point at approximately the midpoint of  $\Gamma$ -K. This band is closer to  $E_F$  than predicted by band structure calculation<sup>14</sup>, indicating possible band renormalization by electron-electron or electron-phonon interactions. While the saddle band in 2H-NbSe<sub>2</sub> has a finite dispersion, the saddle band in 2H-TaSe<sub>2</sub> stays very close to  $E_F$ . It shows minimal dispersion for an extended region of  $k$ -points along  $\Gamma$ -K, forming an *extended* saddle band. In the CDW phase of 2H-TaSe<sub>2</sub> and 2H-TaS<sub>2</sub>, the energy gap is nearly zero on the FS around  $\Gamma$ . In 2H-TaSe<sub>2</sub>, the energy gap is finite in the saddle band region and on the FS around K. No spectral indication of a gap was observed in 2H-NbSe<sub>2</sub> at any  $k$  points within our energy resolution ( $\Delta E=24$  meV). Since the CDW transition temperature in this material is relatively low (33 K), its gap is very small (e. g.,  $\sim 2$ -3 meV). ARPES studies with higher energy resolution are needed in order to study the gap properties.

The favorable nesting condition of the FS pocket around  $\Gamma$  observed in 2H-TaSe<sub>2</sub> and 2H-NbSe<sub>2</sub> might lead to the conclusion that the CDWs in the 2H-polytypes are driven by FS nesting of this cylinder<sup>52</sup>. However, this nesting mechanism is not

consistent with the absence of a finite energy gap on that FS in 2H-TaSe<sub>2</sub> and 2H-TaS<sub>2</sub>. In addition, a CDW driven by such a nesting should be fairly strong, since  $\sim 1/3$  of the FS would be affected. Instead, only a 10-20% decrease in the susceptibility was observed in this family of materials at the CDW onset<sup>13</sup>. Furthermore, this nesting mechanism cannot explain the observed resistivity decrease at the CDW transition. Alternatively, the resistivity decrease can be explained by the “saddle point” mechanism proposed by Rice and Scott<sup>28</sup>. This model is also consistent with the observed saddle band near  $E_F$  and the finite energy gap in the saddle band region. However, the location of the saddle point in  $k$ -space ( $\sim 1/2$ ) is not consistent with the observed CDW wavevector.

The CDWs in these materials are caused by a combination of the partial nesting of the FS pocket around K and the saddle band. As illustrated by Wilson<sup>13</sup>, parts of the FS around K can be brought into a nesting relationship by a displacement of roughly  $1/3 \overline{\Gamma M}$ , giving rise to a broad maximum in the electronic susceptibility,  $\chi(\mathbf{q})$ <sup>47</sup>. Significant contributions to  $\chi(\mathbf{q})$  are associated with points close to  $2/3 \overline{\Gamma K}$ , where the band is just coming out of the saddle point region and is still fairly flat. The removal of the high density of states at  $E_F$  associated with these  $k$  points in the CDW phase can enhance the conductivity. Our observation of a finite gap at both the saddle band region and the FS around K in 2H-TaSe<sub>2</sub> and 2H-TaS<sub>2</sub> is consistent with this scenario. The failure to observe the gap in 2H-NbSe<sub>2</sub> is most likely a simple function of its low transition temperature and may be resolved with further improvement of energy resolution.

## Chapter 7 1T-TaS<sub>2</sub>

Among the transition metal dichalcogenides, the 1T polytype of TaS<sub>2</sub> has been of particular interest due to its complex CDW phase diagram<sup>35</sup>. Angle resolved photoemission (ARPES) has been extensively used to study the CDW transitions in 1T-TaS<sub>2</sub><sup>43,55,56,57,58,59,60,61</sup>, especially the QC to C phase transition. In most experiments<sup>55-59</sup>, a metallic Fermi edge was observed in the QC phase. As the material undergoes the QC to C phase transition, the spectral weight at the Fermi level ( $E_F$ ) abruptly decreases and an intense peak appears at approximately 180 meV binding energy<sup>57-60</sup>. This spectral behavior was interpreted as the opening of a pseudogap in the C phase<sup>59</sup> due to a Mott transition concurrent with the CDW transition. As emphasized by Fazekas and Tosatti<sup>55</sup>, it is not the Mott transition which drives the reconstruction; rather, it is the reconstruction which brings about favorable conditions for the Mott transition to take place. Despite numerous ARPES studies, the electronic structure of 1T-TaS<sub>2</sub> in the QC and C phases is still a matter of controversy<sup>61</sup>. Contributing to this long standing issue, the band dispersions and Fermi surfaces of 1T-TaS<sub>2</sub> in both the QC and C phases were studied with high resolution ARPES.

### 7.1 Band Dispersions

Figure 7-1 shows the EDCs for  $k$ -points along a)  $\Gamma$ -M and a)  $\Gamma$ -K in the QC-CDW state at a temperature of 250 K for 1T-TaS<sub>2</sub>. The  $k$ -points, labeled in  $\text{\AA}^{-1}$ , are the momentum components  $k_x$  for  $\Gamma$ -K and  $k_y$  for  $\Gamma$ -M which are parallel to the respective symmetry lines. In these units, the  $\Gamma$ , M, and K points are at  $(k_x, k_y) = (0, 0)$ ,  $(0, 1.08)$  and  $(1.25, 0) \text{\AA}^{-1}$ , respectively. Note that the thermal broadening is on the order of 100 meV in this phase, which is larger than the 30 meV instrument resolution. As can be seen, at

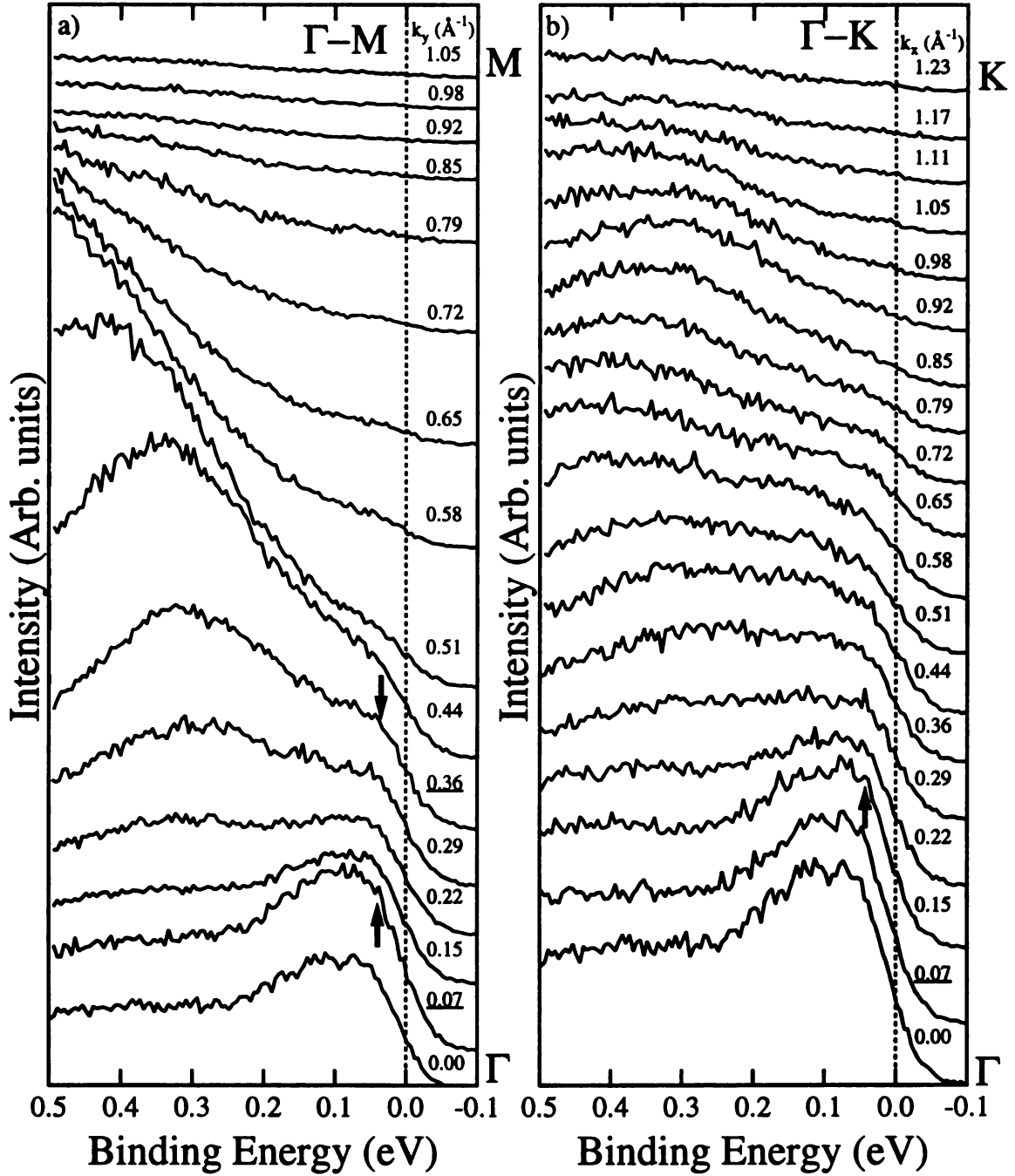


Figure 7-1: EDCs of the QC-CDW ( $T= 250$  K) state for the a)  $\Gamma$ -M and b)  $\Gamma$ -K lines of 1T-TaS<sub>2</sub>. The arrows indicate Fermi crossings.

the  $\Gamma$  point, there is an intense spectral feature just below  $E_F$ . Along the M and K lines, this feature crosses the Fermi level within  $k_y=0.07 \text{\AA}^{-1}$  and  $k_x=0.15 \text{\AA}^{-1}$  respectively as indicated by the upward arrows. This creates a very small electron pocket around the  $\Gamma$  point. As  $k_y$  is scanned toward M, the feature above  $E_F$  disperses back below it at

$k_y=0.36$ , as indicated by the downward arrow. The crossings are estimated at the  $k$ -values where the leading edge midpoint is closest to the Fermi level. These estimates are also confirmed by checking the slope of the spectral leading edge. At Fermi crossings, this slope has a local maximum. This feature continues to disperse well below  $E_F$  along the  $\Gamma$ -M line. There is another broad spectral feature whose centroid is at about 300 meV binding energy at the  $\Gamma$  point. This feature shows very little dispersion along  $\Gamma$ -K, whereas it disperses toward higher binding energies along  $\Gamma$ -M.

To determine the band dispersions accurately, the second derivative of the EDC intensity was determined as a function of energy. At peaks, the second derivative goes to a negative extremum. The resulting band dispersions are shown in Figure 7-2 as the gray scale map where bright indicates positive values and dark negative values. As can be seen, there are dark regions just below  $E_F$  at the  $\Gamma$  point along both lines. The regions

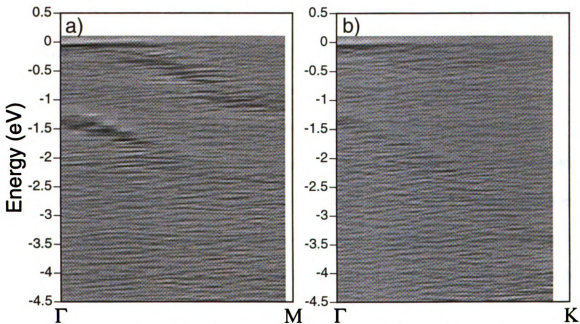


Figure 7-2: Second derivative of the spectral intensity plotted versus energy and wavevector along a)  $\Gamma$ -M and b)  $\Gamma$ -K of 1T-TaS<sub>2</sub>. Darker regions indicate peak positions.

disperse away from  $E_F$  along both lines. Along  $\Gamma$ -M, the band disperses below  $E_F$  in a continuous arc down to 1 eV binding energy. Along  $\Gamma$ -K, the band disperses above  $E_F$  where it no longer contributes to the spectral intensity. There are some other darker regions from a band starting between 1 eV and 1.5 eV at  $\Gamma$  that disperse to deeper binding energies along both lines. These are more prominent along the  $\Gamma$ -M line. Overall, these dispersions are consistent with the qualitative descriptions from the EDCs.

Larson and Mahanti<sup>19</sup> recently performed new band structure calculations using the self-consistent FLAPW method<sup>20</sup> within density functional theory<sup>21</sup>. The calculations were made both without and with spin-orbit corrections. The generalized gradient approximation (GGA) of Perdew, Burke, and Ernzerhof<sup>22</sup> was used for the exchange and correlation potential. The calculations were performed using the WIEN97 package<sup>62</sup>. The atomic radii were chosen identically at 2.29 a.u. for each atom in such a manner so as to minimize the regions between the atomic spheres. Adjustments of these radii within a reasonable range showed little dependence of the final band structure on this variation. The lattice parameters used in the calculation were taken from experiment<sup>15</sup>. Convergence of the self-consistent iterations was performed with 20  $k$ -points in the reduced BZ with a cutoff between valence and core states of -6.0 Ry. Scalar relativistic effects such as mass-velocity and Darwin corrections<sup>63</sup> were included in the calculation. The spin-orbit interactions were included using a second variational procedure of the self-consistent potential<sup>64</sup>. The calculated band dispersions are shown in Figure 7-3 a) with and b) without spin orbit corrections respectively. In Figure 7-3 a), the band which crosses  $E_F$  is primarily a Ta  $5d$ -band. Without spin-orbit correction, this band is slightly above  $E_F$  at the  $\Gamma$  point. Spin-orbit correction splits the bands and places one of the Ta

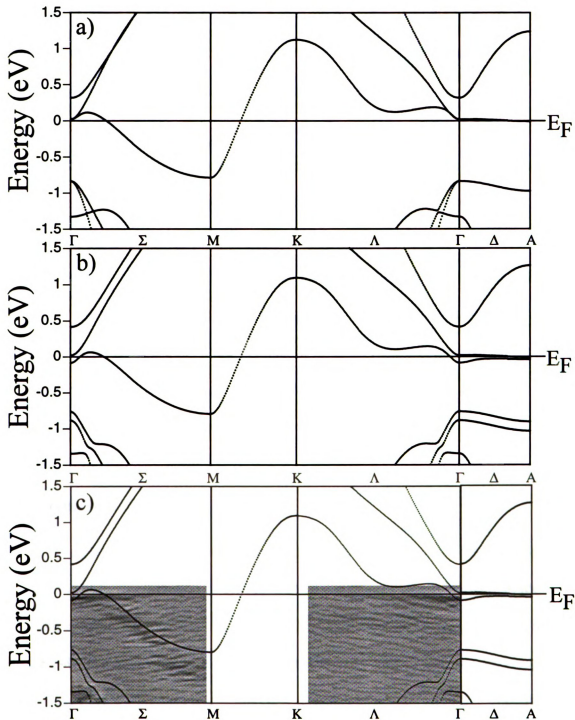


Figure 7-3: Band dispersions in the normal state from new band structure calculation, a) without, and b) and c) both with spin-orbit corrections included. Second derivatives of EDCs along  $\Gamma$ -M and  $\Gamma$ -K in the QC-CDW phase (see text for details) are also shown in c).

$5d$ -bands slightly below  $E_F$  at the  $\Gamma$  point. As a result, the FS has a small electron pocket

around the  $\Gamma$  point in addition to the large electron pocket around the M point. Since the energy bands around the  $\Gamma$  point are sensitive to the interstitial potential<sup>17</sup>, the convergence was carefully checked. Three methods were used: 1) increasing the number of  $k$ -points from 20 to 100, 2) increasing the cutoff energy from 1.5 to 5.5 Ry, and 3) changing the relative sizes of the atomic sphere radii of Ta and S. The convergence was better than 1% indicating that the results give the correct band structures within LDA and GGA. Also, the S  $4p$ -band from the calculation is much closer to the Ta  $5d$ -band than previous calculations show<sup>15-17</sup>, resulting in a much better agreement with ARPES data<sup>51</sup>.

As can be seen in Figure 7-3 c), the agreement between the observed and calculated dispersions is quite good. The features of the measurements match the dispersions of the Ta  $5d$ -band nearest the Fermi level. The calculated gap between the valence band and the top most core level state is also well matched by the observed features.

## 7.2 Fermi Surfaces

The FS topology was investigated by measuring the photoelectron intensity distribution at  $E_F$  as a function of the momentum component parallel to the surface. The resulting  $E_F$  emission intensity maps for the QC-CDW state of 1T-TaS<sub>2</sub> is shown in Figure 7-4. The intensities were normalized to the 21eV photon flux and are presented in a linear gray scale with high intensities corresponding to white. The solid lines mark the unreconstructed Brillouin zone (BZ). One sixth of the data were measured in each map as shown by the dashed wedge in Figure 7-4; the rest were obtained by a mirror operation about  $\Gamma$ -K, then a three-fold rotational symmetry operation. Note that there is a lack of symmetry between the  $\Gamma$ -K line and  $\Gamma$ -K' line at 60° with respect to it. This is partially

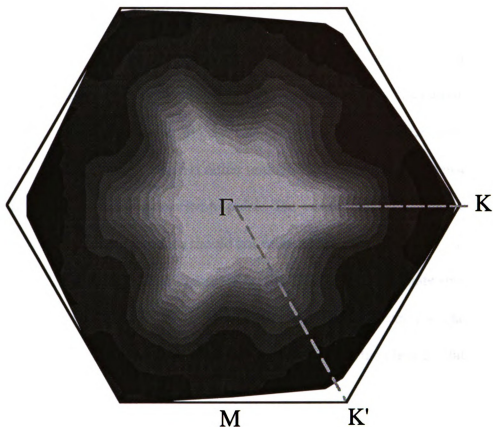


Figure 7-4: Fermi level intensity maps of 1T-TaS<sub>2</sub>. The data between the dashed wedge were actually measured and symmetrized to give the rest of the Brillouin zone. Bright regions correspond to high intensity.

caused by the unequal matrix elements for the two lines since the photon polarization and plane of incidence were both in the horizontal plane which contains  $\Gamma$ -K, and partially caused by the finite escaping depth of the photoemission process<sup>51</sup>.

As can be seen, there is an extended high intensity region around the  $\Gamma$  point, which forms a clear border with the low intensity region in the rest of the BZ. The strength of intensity throughout the  $\Gamma$  area suggests there is some sort of band structure near the Fermi level. The contour of bright region also hints at the shape of an elliptical FS around the M points. This is consistent with predictions by the earlier band structure calculations for the normal state<sup>15-17</sup>. However, the intensity does not extend to the outer

edge of the Brillouin zone as one would expect for a FS around M. Pillo et. al.<sup>61</sup> cited a complete 'remnant' FS around the M point. In order to determine this structure, they divided the intensities on each azimuthal scan, i.e., on concentric circles around  $\Gamma$ , by its mean intensity to remove the overall polar intensity variation, which they considered an artifact of ARPES. This procedure is rather unphysical, since there are intense features seen at deep binding energies near the M point. The overall polar intensity variation is real and is not an artifact, therefore should not be removed in this fashion. Alternatively, the expected FS intensity could be removed by the QC-CDW or that state specific matrix elements could be damping the intensity within a few eV of the Fermi level around M. A detailed calculation of the element effects of the QC-CDW or the photoexcitation matrix would clarify this discrepancy.

### 7.3 Energy Gap in the Commensurate CDW State

Figure 7-5 shows the EDCs measured along  $\Gamma$ -M in the unreconstructed BZ for the C phase ( $T=20$  K, solid lines). For comparison, the corresponding EDCs for the QC phase ( $T=250$  K) are shown as dashed lines. During the experiment, measurements were repeated several times as the sample went through temperature cycles between 20 K and 250 K. The spectra were reproducible and no surface degradation was detected.

Measurements with small temperature increments between 20 K and 250 K showed that the spectral change is correlated with the QC-CDW to C-CDW transition.

Two major spectral changes occur when the material undergoes the QC to C phase transition. First, the spectral intensity at  $E_F$  is nearly completely suppressed at all  $k$ -points. This occurs in the entire BZ, as evidenced from EDC measurements taken on a fine grid of points over the zone. This indicates that the entire FS is truncated and a  $k$ -

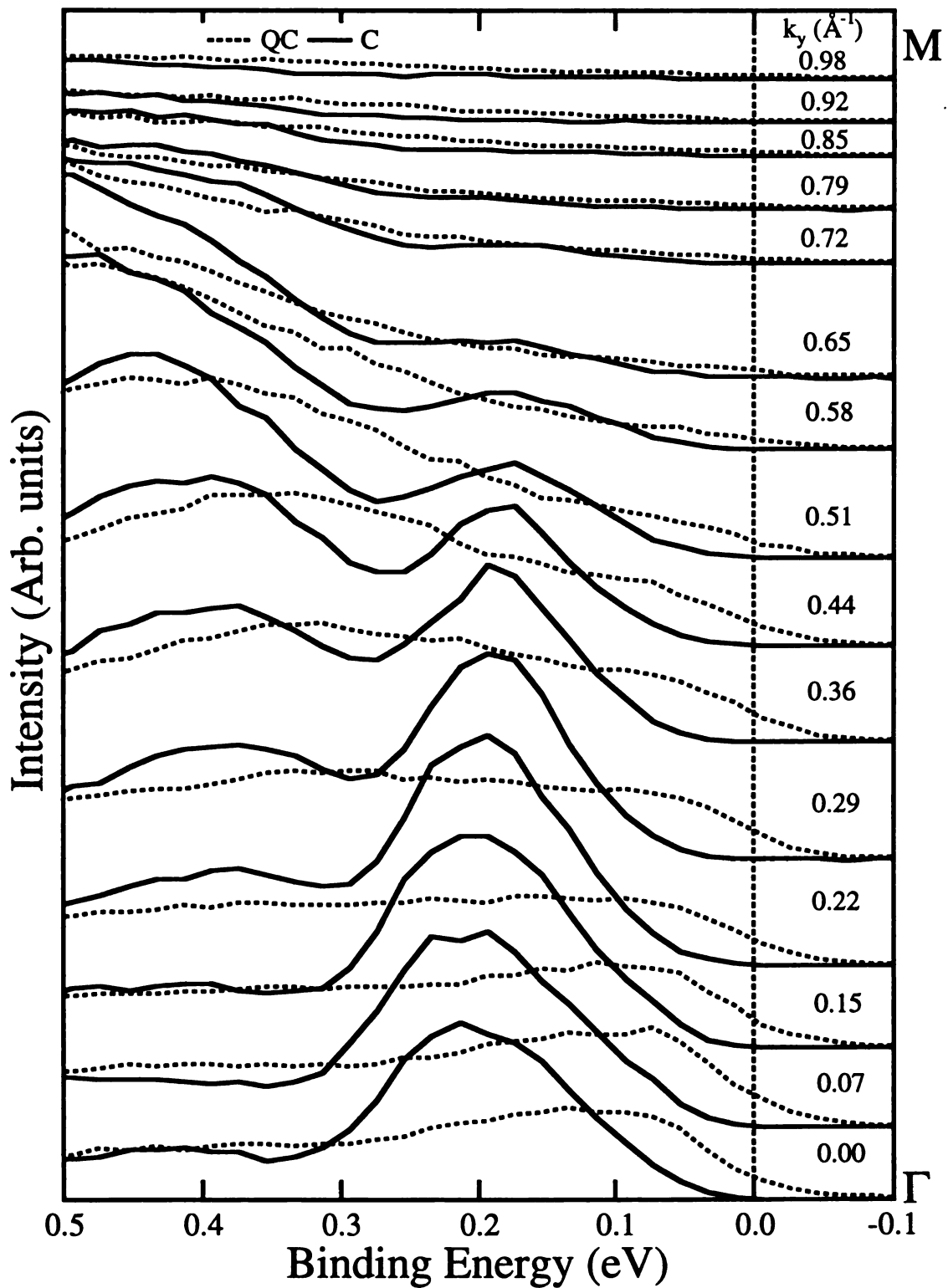


Figure 7-5: EDCs in the C-CDW state ( $T=20$  K, solid curves), for the same set of  $k$ -points along  $\Gamma$ -M as in Figure 7-1 a). The EDCs in the QC-CDW state are superimposed as the dashed curves for comparison.

independent energy gap (or pseudogap) opens at  $E_F$  in the C phase. To quantify the size of the energy gap, the energy shift between the leading edge midpoints in the normal and CDW state is used. From this, it is clear that the gap is on the magnitude of 120 meV. Different methods of determining the gap might change the numbers slightly, but have little other effect. Second, an intense peak develops at about 180 meV binding energy. However, this band is flatter than the one seen in the QC-CDW phase. It does not disperse in energy towards the Fermi level but simply loses intensity until it is indistinguishable from background. This is very similar to the loss of intensity in the FS seen around the M point in the QC-CDW phase.

#### **7.4 Summary and Discussion**

Previous ARPES experiments found some disagreement between the QC-CDW phase and the calculated normal state band structures. For example, recently Pillo et. al.<sup>61</sup> reported that there is a pseudogapped, remnant FS around the M point. Instead of resolving clear Fermi crossings, they found peaks which only had thermal tails that just reached  $E_F$ . In contrast, the data in Figure 7-1, Figure 7-2, and Figure 7-4 show that there exists a FS in the QC phase. There are two clear crossings distinguished along the  $\Gamma$ -M line and another crossing along the  $\Gamma$ -K line. The second crossing along the  $\Gamma$ -M line is part of the normal state FS predicted by previous, non-relativistic band structure calculations<sup>15-17</sup> that still exists in the QC-phase. This Fermi surface is harder to distinguish at higher  $k$ -values, as seen in Figure 7-3, possibly due to some effects of the QC-CDW or band dependent matrix element effects.

The FS determined from these measurements is slightly different from the previous band calculations, since there is an apparent small electron pocket near the  $\Gamma$

point. This result is consistent with those of many other ARPES studies<sup>43,55-60</sup>, though. Several groups<sup>43,56,57</sup> previously saw in the QC-CDW state a set of bands just below the Fermi level near  $\Gamma$ . To understand this feature, new band calculations were performed by Larson and Mahanti<sup>19</sup> including relativistic and spin orbit corrections. The inclusion of the spin orbit corrections makes one small, but crucial change as can be seen by comparing Figure 7-3 a) and b). The spin orbit corrections pull a Ta  $5d$ -band just below  $E_F$  in a region near the  $\Gamma$  point. This matches the additional crossing seen in these measurements and implied by the other ARPES experiments.

In the C phase, the entire FS is truncated and the top most band is pushed down to approximately 180 meV below  $E_F$ . This suppresses the intensity within 120 meV of the Fermi level and it occurs across the entire Brillouin zone, indicating a  $k$ -independent energy gap. These spectral changes have been seen previously at normal emission<sup>58-60</sup> and it was shown that they occur within a few degrees at the transition<sup>59</sup>. The dramatic spectral changes occurring at the QC to C phase transition are the results of a CDW-induced Mott transition as suggested by Fazekas and Tosatti<sup>55</sup>. As they pointed out, the resistivity in the C phase is higher than the two-dimensional metallic limit, indicating that the material has become a Mott insulator. There are two arguments that this gap in the C-CDW phase indicates a Mott insulator. First, the gap is entirely  $k$ -independent. A purely CDW nesting gap should only affect states near the Fermi surface regions that are nested. Second, the size of the gap is 120 meV, which is larger than the expected gap size of 75 meV estimated using the BCS formula.

In summary, using high energy and high angular resolution ARPES, a FS in the QC-CDW phase of 1T-TaS<sub>2</sub> was observed. Its shape was quite comparable with that of

the normal state FS predicted by previous band structure calculations<sup>15-17</sup> and is consistent with previous ARPES measurements. A small electron pocket was found around the  $\Gamma$  point, though, that was not previously determined. The observed Fermi crossing near the  $\Gamma$  point is consistent with new band structure calculations that include spin orbit corrections. Under the QC to C-CDW transition, a large,  $k$ -independent gap resulting from a Mott insulator transition is resolved.

## Chapter 8 1T-TiSe<sub>2</sub>

The electrical and CDW properties of 1T-TiSe<sub>2</sub> have been subjects of interest for years. There has been an outstanding question of whether 1T-TiSe<sub>2</sub> is a semimetal or semiconductor. ARPES experiments<sup>39,65,66,67,68,69,70,71,72,73</sup> have been performed to address this issue but the results are inconsistent. The CDW properties have also been studied by ARPES. However, all but one recent experiment<sup>74</sup> had rather poor energy and momentum resolutions. In this study, high resolution ARPES studies of 1T-TiSe<sub>2</sub> were performed in both the normal and CDW states.

### 8.1 Band Dispersions

As shown in Chapter 4, unlike the other TMDs studied here, 1T-TiSe<sub>2</sub> has a rather three-dimensional like electronic structure in spite of its quasi-two-dimensional layered morphology. Therefore, a three-dimensional band mapping is necessary. In these experiments, the free-electron approximation for the states was used to estimate the  $k_z$ -components of the initial electron state. The three-dimensional band dispersions were mapped by varying the photon energy and the analyzer angle simultaneously, as described in Chapter 2.

Figure 8-1 shows the EDCs for  $k$ -points with parallel components along the directions of a)  $\Gamma$ -M and b)  $\Gamma$ -K at 21 eV photon energy. They were taken in the normal state for 1T-TiSe<sub>2</sub> at room temperature. Spectra along both lines show a double peak feature at the Fermi level right next to the  $\Gamma$  point. These bands disperse quickly away from  $E_F$  to deeper binding energies. This indicates that the Fermi surface around  $\Gamma$  is a hole pocket, since it surrounds a region of unoccupied bands. Along the  $\Gamma$ -M direction, there is a second feature that appears at  $E_F$  near the M point. Since no band disperses to

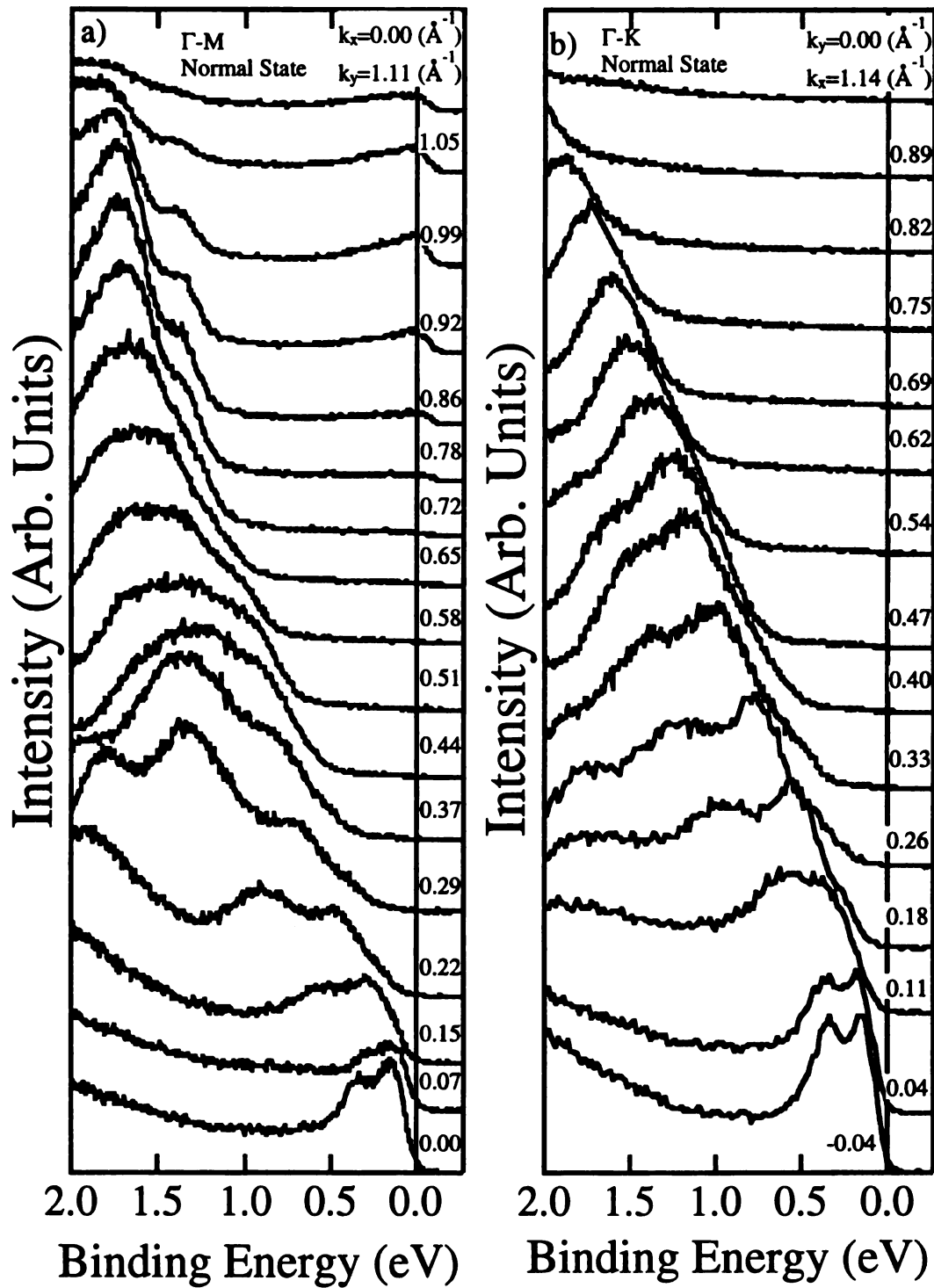


**Figure 8-1: Normal state EDCs for the projections along a)  $\Gamma$ -M and b)  $\Gamma$ -K lines of 1T-TiSe<sub>2</sub>.**

deeper binding energy from this feature, it must disperse down from the unoccupied states instead. This makes the Fermi surface pocket out near the M point an electron pocket, since it encloses occupied electron bands.

100

101

102

103

104

105

106

107

108

109

110

111

112

113

114

115

116

117

118

119

120

121

122

123

124

125

EDCs taken along the normal emission direction which correspond to  $k$ -points along  $\Gamma$ -A are shown in Figure 8-2 a). For the normal emission spectra, the electrons have no parallel  $k$ -component so that by varying the photon energy, one directly probes

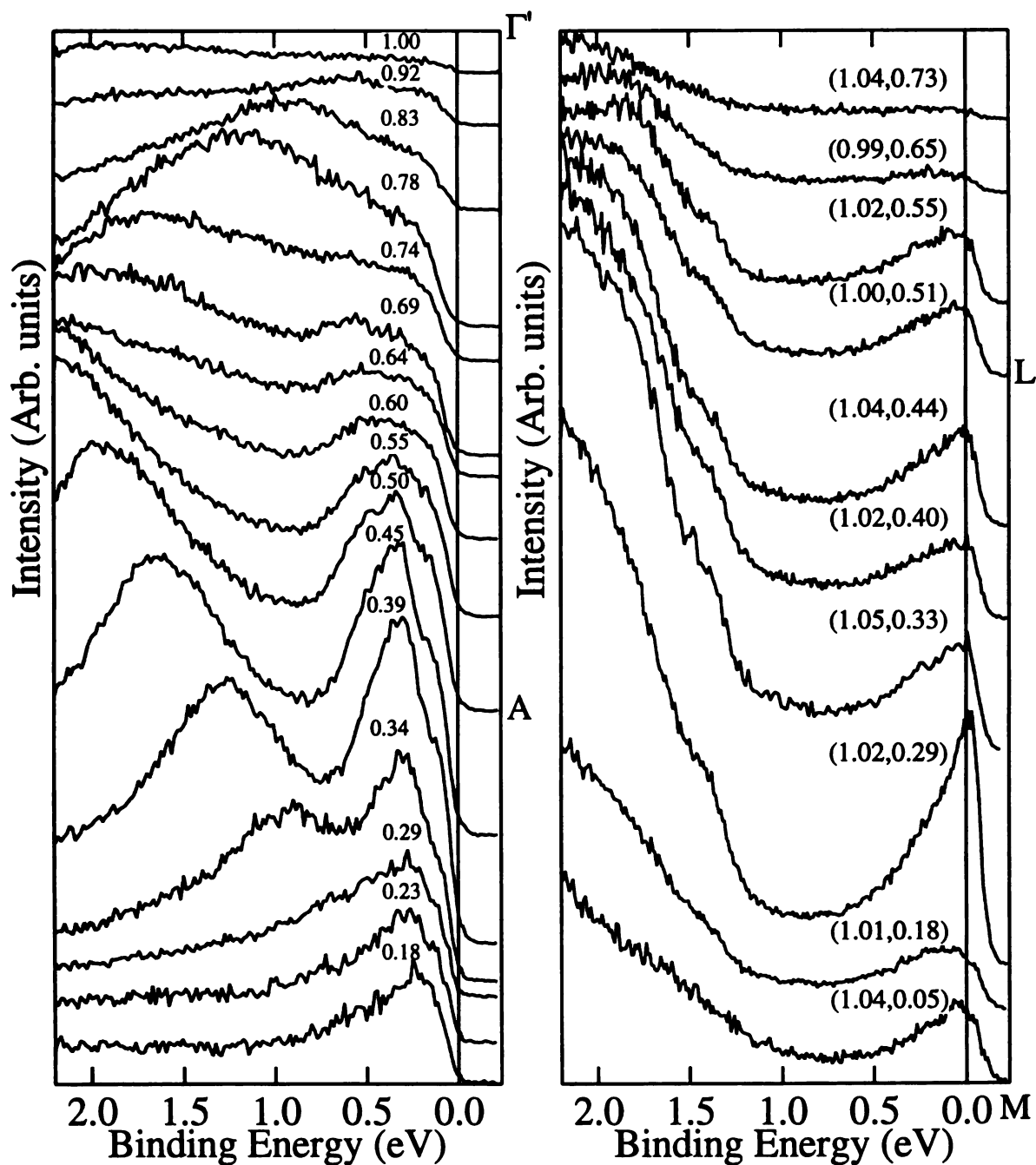


Figure 8-2: EDCs along the normal emission directions of a)  $\Gamma$ -A and b) M-L of 1T-TiSe<sub>2</sub>. The EDCs of a) are labeled with the  $k_z$  ( $\text{\AA}^{-1}$ ) distance from  $\Gamma$ . The EDCs of b) are labeled with their  $(k_x, k_z)$   $\text{\AA}^{-1}$  values.

the  $k_z$ -dispersion. As can be seen, there are three bands below the Fermi level within 2 eV. The first band disperses from above  $E_F$  to below  $E_F$  at  $k_z = 0.18 \text{ \AA}^{-1}$ . It disperses to about 2eV below  $E_F$  and then disperses back to  $E_F$  at higher  $k_z$ -points. The large amount of dispersion demonstrates that the electronic structure of 1T-TiSe<sub>2</sub> is quite three-dimensional. The second band appears around  $k_z = 0.23 \text{ \AA}^{-1}$  and disperses down to a binding energy of  $\sim 0.5$  eV. The third feature appears as a shoulder between the second band and the Fermi level. It becomes evident near  $k_z = 0.29\text{-}0.34 \text{ \AA}^{-1}$  and remains within 0.1 eV of  $E_F$  at all times. By careful consideration of the symmetry of the dispersion along the  $\Gamma$ -A line, an estimation of the inner potential can be made. The  $k_z$ -values labeled in Figure 8-2 were determined from this estimation. The A point is estimated at  $k_z = 0.50 \text{ \AA}^{-1}$ .

Figure 8-2 b) shows EDCs approximately along M-L. The  $k$ -values were selected by varying the analyzer angle and the photon energy simultaneously. There is a feature at deep binding energy. It disperses from well below 2 eV binding energy to a minimum around 1.8 eV binding energy at the L point and then disperses to deeper binding energies again. This further demonstrates the three dimensional nature of the band dispersion. There is a second feature that appears as a small shoulder on this first band that seems to move with it. Finally, there is a feature near the Fermi level that only shows small dispersions. This feature is a very intense and sharp at (1.02, 0.29) and several other crossings as well without any bands dispersing much below the Fermi level. This suggests that this is a small electron pocket from some band above the Fermi level.

## 8.2 Fermi Surfaces

The FS topology was investigated by measuring the photoelectron intensity

distribution at  $E_F$  at a constant photon energy of 21 eV. The resulting  $E_F$  emission intensity map for the normal state of 1T-TiSe<sub>2</sub> is shown in Figure 8-3, labeled with the parallel  $k$ -components of the momentum. Because of the three-dimensional characteristic of 1T-TiSe<sub>2</sub>, the change in the  $k_z$ -component must also be considered. The intensity map is effectively over a parabolic surface with a foci at (0, 0) upon the A point and the edges of the hexagon roughly halfway between L and M.

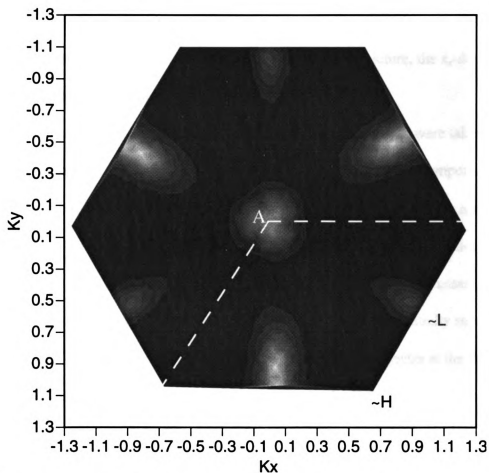


Figure 8-3: Fermi level intensity maps of 1T-TiSe<sub>2</sub> taken with 21eV photons. The data between the dashed lines were actually measured and rotated to give the rest of the Brillouin zone.

One third of the data were measured as shown by the dashed wedge in Figure 8-3; the rest were obtained by a three-fold rotational symmetry operation. Note that there is a lack of symmetry between the A-L line and A-L' line at 60° with respect to it. There are

two causes of this distinction. First, there are unequal matrix elements for the two lines since the photon polarization and plane of incidence were both in the horizontal plane of AHK $\Gamma$ . Second, the finite escaping depth of the photoemission process<sup>51</sup> may not include the effective sources of the two lines equally. This intensity map shows that there is some spectral intensity near the zone center around the  $\Gamma$ -A and near the zone edge around M-L within the energy window of the analyzer. According to band calculations, the FS of 1T-TiSe<sub>2</sub> consists of two small ellipsoids, one around  $\Gamma$  and one around L. Although the intensity map is qualitatively consistent with this picture, the  $k_z$ -dependence of the FS needs to be determined more closely by EDCs.

To determine the Fermi crossings along the  $k_z$ -direction, EDCs were taken on a grid of points around the  $\Gamma$ -A and L-M lines in the normal state at room temperature. Figure 8-4 a) shows some EDCs near the L-M line. As can be seen, there are actually peaks above the Fermi level. It is not clear that the band actually disperses below the Fermi level at all, because the leading edge is significantly above  $E_F$  in all cases. In contrast, the bands near the  $\Gamma$ -A line, shown in Figure 8-4 b), do not actually seem to reach the Fermi level, because the Fermi level only intersects the spectra at the thermal tails of the peaks. It appears as if there is a pseudogap in the  $\Gamma$ -A region, with the spectral intensity leading edge midpoint at a binding energy of 80 meV. The results were repeatedly found on different samples. Unfortunately, the locations of Fermi crossings are not apparent in these EDCs. Therefore, the exact FS shape along the  $k_z$ -direction is still not resolved.

In principle, ARPES is not able to probe the unoccupied states above the Fermi level. In this material, there is a combination of unique factors that allow the unoccupied

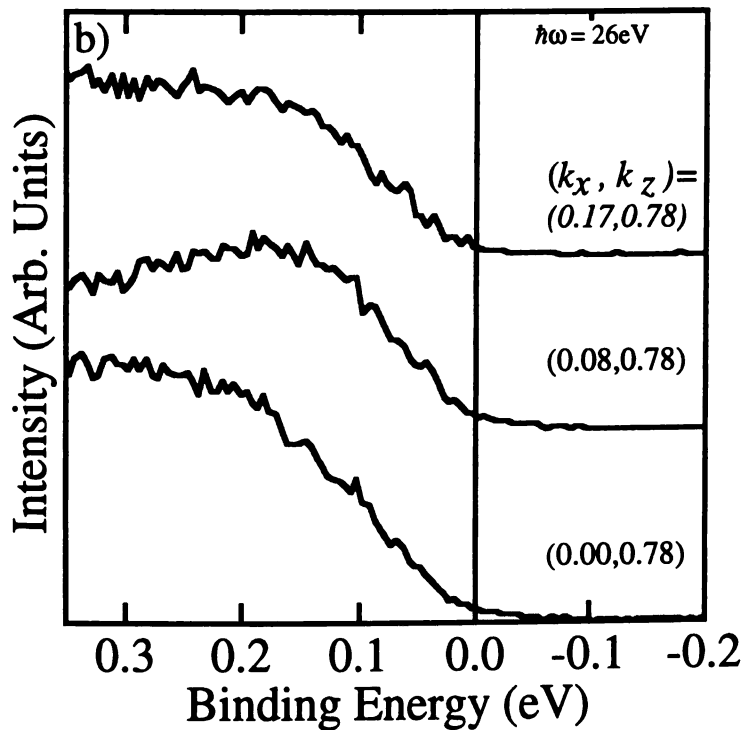
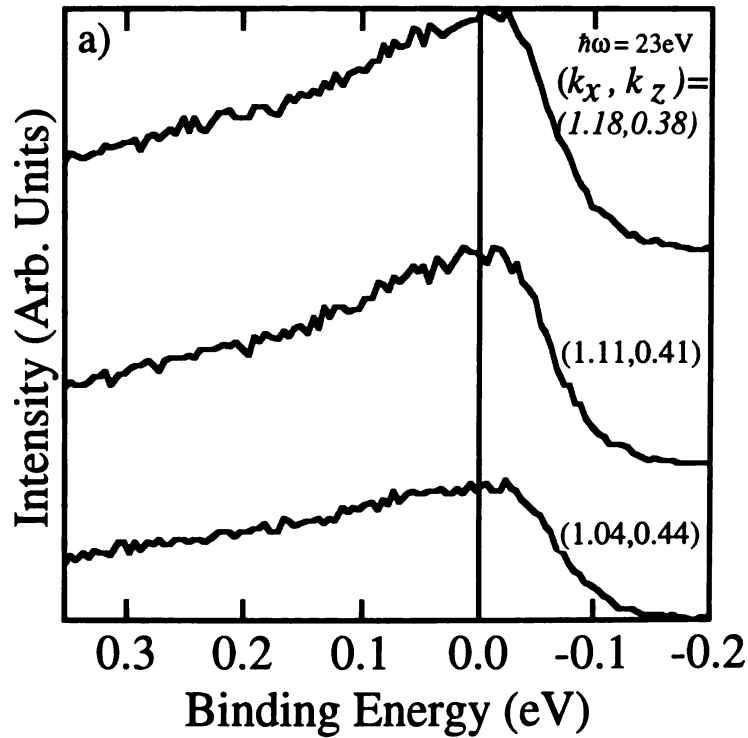


Figure 8-4: EDCs taken near apparent Fermi crossing in the normal state of 1T-TiSe<sub>2</sub> near a) the L point and b) midway between A and  $\Gamma'$ . The  $(k_x, k_z)$  points are in  $\text{\AA}^{-1}$ .

states to be probed. The spectral leading edge along the L-M line has a midpoint 65 meV

above  $E_F$ . This location indicates that the band is above the Fermi level and is detected only because of thermally excited electrons. These features never cross the Fermi level, but simply come within a minimal distance of the Fermi level near the L point. The actual peak position may not be directly indicative of the band location, since the spectral shape is distorted by the Fermi function.

In order for ARPES to yield this sort of information, there are three requirements which must be met. First, the peak that is above the Fermi level has to be narrow and strong. The peak has to be intrinsically less than one half the width of its nearest approach. Otherwise, the observed peak will have enough intensity on the occupied side of the Fermi level that it will dominate and the peak position will appear below the Fermi level as normally seen. Titanium *3d*-bands fulfill these requirements. Second, there has to be limited momentum resolution. If the peak disperses much and there is poor momentum resolution, the apparent position will be smeared out by the peak's own dispersion. Third, the Fermi function has to be rather broad. This condition is easily met by high temperatures, since the system temperature broadens the Fermi function. At room temperature, this thermal broadening gives an effective  $4.2k_B T$  width of 110 meV. The observation of photoemission intensity above  $E_F$  in this material was also reported by Pillo et. al.<sup>74</sup> at the time these data were taken and has been seen in other Ti compounds as well<sup>75</sup>.

### **8.3 Energy Gap in the CDW State**

The formation of a CDW usually opens an energy gap at the Fermi energy and truncates parts of the FS that are connected by the CDW modulation's wavevector. In 1T-TiSe<sub>2</sub>, there is only limited evidence of there being a Fermi surface, though. Instead,

there are a set of Se bands just below  $E_F$  around  $\Gamma$  and a set of Ti bands above  $E_F$  around the L points. There is a vector  $\mathbf{Q}_0$  which is consistent with the observed CDW wavevector that would connect these respective electron and hole states into an exciton. This suggests that 1T-TiSe<sub>2</sub> has an excitonic insulator transition driving the CDW formation, as suggested by Wilson and Mahajan<sup>76,24</sup>.

The property of the energy gap was investigated by measuring spectra near the L and  $\Gamma$  points above and below the CDW transition temperature. During the experiment, measurements were repeated on several different samples and through temperature cycles between 20 K and 240 K. The spectra were reproducible and no surface degradation was detected. The EDCs are plotted in Figure 8-5. Strictly speaking, a gap can be defined only on a Fermi surface. Here, we also use the term “gap” for the pseudogap region around the  $\Gamma$  point and the near crossings of the L point. This is justified since there are states near  $E_F$  at those  $k$ -points and they are affected by the CDW formation.

The spectra in Figure 8-5 a) show a dramatic change as a function of temperature. The single broad peak in the normal state is split into two peaks in the CDW state. At 20K, the spectral leading edge is pushed toward higher binding energy by 55 meV by the formation of the CDW. However, there is still significant spectral intensity at the Fermi level. It appears as if the band is lowered and now crosses  $E_F$ . In addition, another intense peak appears at approximately a binding energy of 180 meV. This dramatic restructuring of bands might be due to the superlattice of the CDW state, which can cause band folding.

As can be seen in Figure 8-5 b), the spectral change near the  $\Gamma$ -point is also significant, although not as dramatic. There, the spectral intensity near  $E_F$  is suppressed

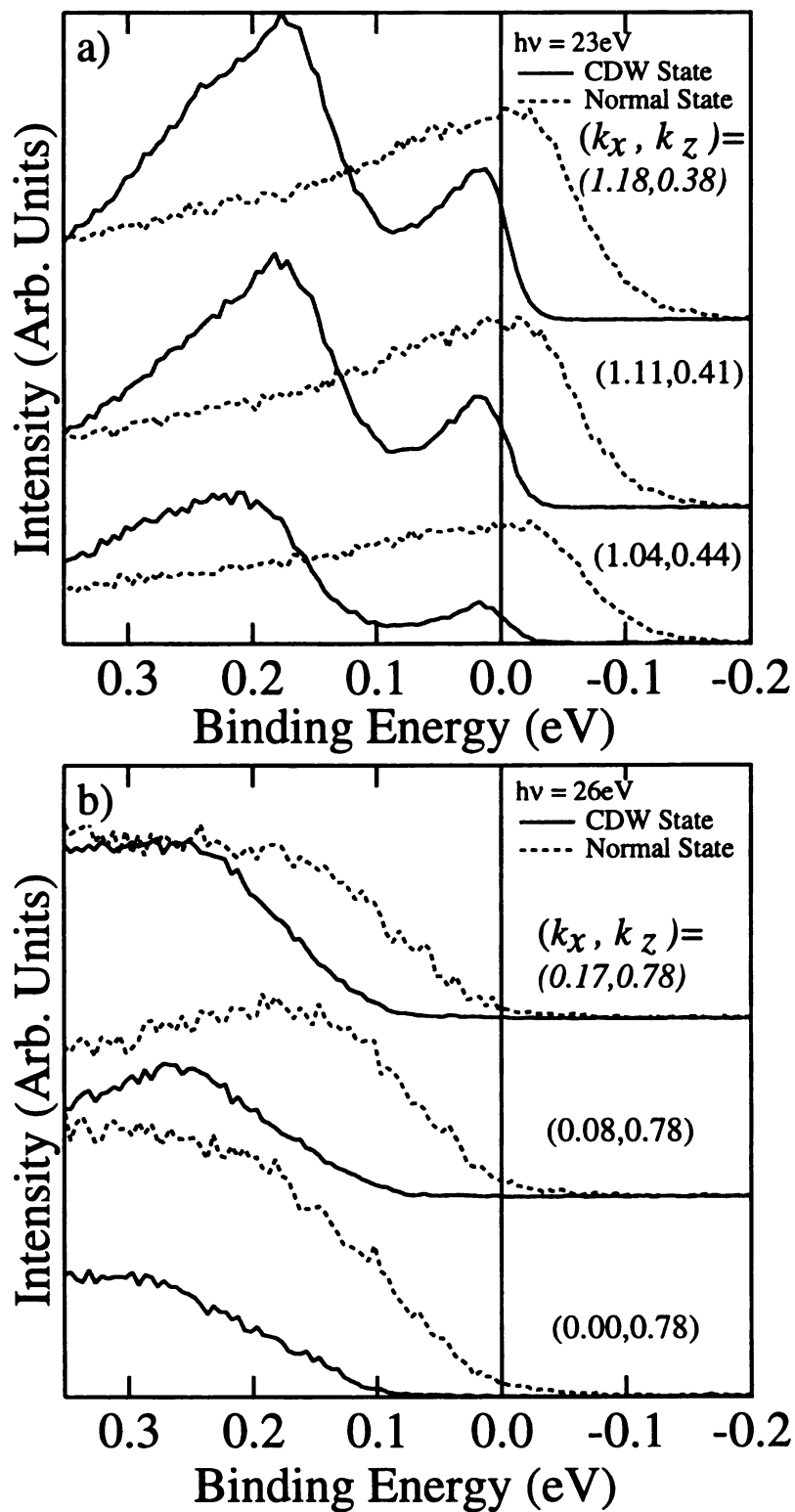


Figure 8-5: The temperature dependence in 1T-TiSe<sub>2</sub> of bands close in energy to the Fermi level near a) the L-M line and b) the A point. The normal state EDCs are shown in dashed lines and the CDW state in solid lines.

and the leading edge is shifted toward higher binding energy by 85 meV. It appears that the pseudogap is significantly widened by the CDW. There is no peak splitting evident in these bands.

## 8.4 Summary

In summary, the normal state band dispersions of 1T-TiSe<sub>2</sub> was investigated. It was seen that the electronic structure of this material is quite three-dimensional, showing significant dispersions in the direction perpendicular to the layers. Both the EDCs and the  $E_F$  intensity map show emission intensities near  $E_F$  in the regions around the  $\Gamma$ -A and M-L, qualitatively consistent with the FS predicted by the band structure calculations. However, the high resolution EDC spectra show that, the band is actually located approximately 65 meV above  $E_F$  at the L point. At the  $\Gamma$  point, the band is located approximately 80 meV below  $E_F$ . Therefore, 1T-TiSe<sub>2</sub> is actually a semiconductor with an indirect gap of  $\sim$ 145 meV. In the CDW state, bands in both regions are dramatically affected. There is still intensity at  $E_F$  as the band near the L point is pulled down to cross  $E_F$ . This provides carriers for the CDW state to remain in a semimetallic phase with a resistivity comparable to its semiconducting normal phase.

The normal state band structure and the CDW's dramatic effects upon it support the excitonic-insulator model<sup>76,24</sup> of the CDW mechanism for this material. The band near  $\Gamma$  is the top of the valence band and provides electron carriers. In contrast, the band near L is the bottom of the conduction band and consists of hole carriers. The two regions also directly connect with the CDW wavevector.

## Chapter 9 Summary

In summary, high resolution ARPES was used to study the electronic structure of the transition metal dichalcogenides 2H-TaSe<sub>2</sub>, 2H-TaS<sub>2</sub>, 2H-NbSe<sub>2</sub>, 1T-TaS<sub>2</sub>, and 1T-TiSe<sub>2</sub>. Their normal state band dispersions and Fermi surfaces, and the CDW energy gap properties were investigated in detail. A number of new spectral properties in these materials were discovered.

Although 2H-TaSe<sub>2</sub> is one of the first materials to be studied by ARPES, a detailed study of the Fermi surface and CDW gap property was lacking until the present study. Early studies focussed on band dispersions below  $E_F$ <sup>51</sup>. Some of the more recent studies addressed spectral changes in the CDW state<sup>43,44</sup>. However, they suffered either from insufficient energy resolution or from insufficient momentum resolution. The new findings in this study include: 1) An extended saddle band very close to the Fermi level was observed along  $\Gamma$ K. 2) The Fermi surface was determined for the first time. It consists of a pocket around  $\Gamma$  and another pocket around K, qualitatively consistent with band structure calculations. 3) It was found that there is no gapping on the Fermi cylinder around  $\Gamma$  in the CDW state, indicating that this Fermi cylinder does not contribute to the CDW mechanism. A gap of 18 meV was observed in the saddle band region and on the Fermi surface around K. These results suggest that the CDW in the material originates from both the partial nesting of the Fermi surfaces around K and the saddle band along  $\Gamma$ -K as proposed by Rice and Scott<sup>28</sup>. 4) The temperature dependence of the CDW gap indicates a deviation from the BCS relation, suggesting that the weak coupling theory is not sufficient to describe the CDW in this material. Two other closely related compounds of 2H-TaS<sub>2</sub> and 2H-NbSe<sub>2</sub> were also studied. Although the results are

not as complete as those for 2H-TaSe<sub>2</sub> due to experimental or material limitations, they are consistent with the conclusions made for the 2H-TaSe<sub>2</sub> data.

For 1T-TaS<sub>2</sub>, its electronic properties near the Fermi energy in both the QC-CDW and C-CDW phases have been studied by ARPES very extensively<sup>43,55-61</sup>. It was observed that the spectral shape near  $E_F$  undergoes dramatic changes at the QC- to C-CDW transition. The emission intensity at  $E_F$  is nearly completely suppressed and a strong peak appears at approximately 180 meV binding energy in the C-CDW phase. These changes occur within a few degrees of the transition<sup>59</sup>. These measurements were made at normal emission with poor angular resolution of  $\pm 5^\circ$ . The  $k$ -dependence of the spectral changes was not investigated. It was also observed that the bands collapse into three subbands separated by gaps in the C-CDW<sup>43</sup>. The new findings in the present study include: 1) In the QC-CDW phase, the EDCs and Fermi intensity map indicate significant emission intensity near the  $\Gamma$  point and there is a Fermi pocket near  $\Gamma$  in addition to the large one around M. This result is inconsistent with the early non-self-consistent non-relativistic band structure calculations<sup>15-17</sup> which predict only the Fermi surface pocket around M. Although this discrepancy was noted in previous ARPES experiments<sup>51</sup>, it was not investigated in detail. From recent self-consistent band structure calculations by Larson and Mahanti<sup>19</sup>, it was determined that the emission intensity and the Fermi crossing near G was caused by spin-orbit interactions which were not included in previous calculations. 2) By measuring EDCs in both the QC-CDW and C-CDW phases over a large portion of the Brillouin zone, it was determined that a  $k$ -independent gap of 120 meV opened. This gap opens at the QC- to C-CDW transition throughout the

Brillouin zone. This supports the argument for a Mott localization occurring at the QC-CDW to C-CDW transition<sup>55</sup>.

For 1T-TiSe<sub>2</sub>, previous ARPES studies with moderate energy and moderate angular resolutions found that the band structure near  $E_F$  near the L point is significantly affected by the CDW transition<sup>69</sup>. There also existed a controversy on whether this material is a semimetal or small gap semiconductor<sup>66,73</sup>. The new findings in the present study include: 1) Significant band dispersions in the direction perpendicular to the layers were observed, indicating a strong three-dimensional characteristic despite its layered structure. 2) It was observed that in the normal state a band stays slightly below  $E_F$  near the  $\Gamma$  point and another band stays slightly above  $E_F$  near the L point. The latter was observed only because of thermal population of the band. This suggests that 1T-TiSe<sub>2</sub> is a narrow gap semiconductor in the normal phase. 3) In the CDW state, the band near  $\Gamma$  is pushed to deeper binding energy and the band near L is lowered below  $E_F$  with an additional band appearing at higher binding energy. The lowering of the band near L to the Fermi level indicates that the material becomes a semimetal in the CDW state. The fact that both bands are affected by the CDW supports the excitonic insulator CDW mechanism<sup>37</sup>. Similar results were reported in a paper by Pillo et. al.<sup>74</sup> at the time these measurements were made.

In conclusion, the present high resolution ARPES studies of these materials have provided more details about the electronic structures relevant to the CDW formation. Some spectral phenomena are still not well understood and require further theoretical and experimental investigation.

## References

- 
1. M. K. Wu, J. R. Ashburn, C. J. Torng, P. H. Hor, R. L. Meng, L. Gao, Z. J. Hwang, Y. Q. Wang, and C. W. Chu, *Phys. Rev. Lett.* **58** (1987) 908.
  2. H. Maeda, Y. Tanaka, M. Fukutomi, and T. Asano, *Jpn. J. Appl. Phys.* **27** (1988) L209; C. W. Chu, J. Bechtold, L. Gao, P. H. Hor, Z. J. Huang, R. L. Meng, Y. Y. Sun, Y. Q. Wang, and Y. Y. Xue, *Phys. Rev. Lett.* **60** (1988) 941.
  3. J. G. Bednorz and K. A. Müller, *Z. Phys. B* **64** (1986) 189.
  4. A. Einstein, *Ann. d. Phys. (Leipzig)* **17** (1905) 932.
  5. C. N. Berglund and W. E. Spicer, *Phys. Rev. A* **136** (1964) 1030.
  6. M. P. Seah and W. A. Dench, *Surf. And Interface Anal.* **1** (1979) 2.
  7. S. Tougaard, *Surface and Interface Analysis* **11** (1988) 453.
  8. D. A. Shirley, "Many-Electron and Final-State Effects: Beyond the One-Electron Picture", *Photoemission in Solids I*, Ed. M. Cardona and L. Ley, Topics Appl. Phys., **26**, Berlin (1979) Chap. 4.
  9. F. J. Di Salvo, Jr. and T. M. Rice, *Phys. Today* **22** April (1979) 32.
  10. G. Grüner, *Density Waves in Solids*, Addison-Wesley, Reading Massachusetts (1994).
  11. R. E. Peierls, *Quantum Theory of Solids*, Oxford Press, New York (1955) 108.
  12. H. Fröhlich, *Proc. Roy. Soc.* **A223** (1954) 296.
  13. J. A. Wilson, *Phys. Rev. B* **15** (1977) 5748.
  14. G. Wexler and A. M. Woolley, *J. Phys. C: Solid State Phys.* **9** (1976) 1185.

- 
15. L. F. Mattheiss, *Phys. Rev. B* **8** (1973) 3719.
  16. M. W. Myron and A. J. Freeman, *Phys. Rev. B* **11** (1975) 2735.
  17. A.M. Woolley and G. Wexler, *J. Phys. C: Solid State Phys.* **10** (1977) 2601.
  18. R. B. Murray and A. D. Yoffe, *J. Phys. C* **5** (1972) 3038.
  19. P. Larson and S. D. Mahanti, unpublished
  20. D. Singh, *Plane Waves, Pseudopotentials, and the LAPW Method*, Kluwer Academic, Boston (1994).
  21. P. Hohenberg and W. Kohn, *Phys Rev. B* **136**, (1964) 864; W. Kohn and L. Sham, *ibid. A* **140** (1965) 1133.
  22. J. P. Perdew, K. Burke, and M. Ernserhof, *Phys. Lett.* **77** (1996) 3865.
  23. G. A. Benesh, A. M. Woolley, and C. Umrigar, *J. Phys. C* **18** (1985) 1595.
  24. J. A. Wilson, *Phys. Stat. Sol. B* **86** (1978) 11.
  25. H. Nishihara, G. A. Scholz, and R. F. Frindt, *J. Phys. Soc. Japan* **43** (1977) 1509.
  26. R. F. Frindt and D. J. Huntley, "Experimental Aspects of Superconductivity in Layered Structures", *Optical and Electrical Properties*, Ed. P. A. Lee, Reidel Publishing Company, Dordrecht, Holland (1976) 403.
  27. J. Edwards and R. F. Frindt, *J. Phys. Chem Solids* **32** (1971) 2217.
  28. T. M. Rice and G. K. Scott, *Phys. Rev. Lett.* **35** (1975) 120.
  29. C. Ayache, R. Currat, B. Hennion, and P. Molinie, *J. de Phys. IV* **C2** (1993) 125.
  30. H. N. S. Lee, M. Garcia, H. McKinzie and A. Wold, *J. Solid State Chem.* **1** (1970) 190.
  31. A. H. Thompson, F. R. Gamble and R. F. Koehler, *Phys. Rev. B* **5** (1972) 2811.
  32. D. A. Whitney, R. M. Fleming and R. V. Coleman, *Phys Rev B* **15** (1977) 3405.

- 
33. D. J. Huntley and R. F. Frindt, *Can. J. of Phys.* **52** (1974) 861.
34. R. Manzke, T. Buslaps, B. Pfalzgraf, and M. Skibowski, and O. Anderson, *Europhys. Lett.* **8** (1989) 195.
35. J. A. Wilson, F. J. Di Salvo and S. Mahajan, *Adv. Phys.* **24** (1975) 117.
36. H. Mutka, L. Zuppiroli, P. Molinié, and J. C. Bourgoin, *Phys Rev. B* **23** (1981) 5030.
37. J. A. Wilson and S. Mahajan, *Commun. Phys.* **2** (1977) 23.
38. R. V. Coleman, B. Giambattista, P. K. Hansma, A. Johnson, W. W. McNairy, and C. G. Slough, *Adv. Phys.* **37** (1988) 559.
39. F. J. Di Salvo, D. E. Moncton, and J. V. Waszczak, *Phys. Rev. B* **14** (1976) 4321.
40. D. Jérôme, C. Berthier, P. Molinié and J. Rouxel, *J. Phys.* **37** (1976) C4.
41. C. G. Olson, *Nucl. Instrum. Methods A* **266** (1988) 205.
42. For a review, see D. W. Lynch and C. G. Olson, *Photoemission Studies of High Temperature Superconductors*, Cambridge University Press, Cambridge, UK, (1999).
43. N. V. Smith, S. D. Kevan, and F. J. Di Salvo, *J. Phys. C: Solid State Phys* **18** (1985) 3175.
44. B. Dardel, M. Grioni, D. Malterre, P. Weibel, Y. Baer, and F. Lévy, *J. Phys. Condens. Matter* **5** (1993) 6111.
45. K. Motizuki and N. Suzuki, *Structural Phase Transition in Layered Transition-metal Compounds*, Ed. K. Motizuki, Reidel Publishing Company, Dordrecht, Holland (1986) 1.
46. K. Motizuki, K. Kimura, E. Andō, and N. Suzuki, *J. Phys. Soc. Japan* **53** (1984) 1078; K. Motizuki, and E. Andō, *ibid.* **52** (1983) 2849.

- 
47. N. J. Doran, B. Ricco, M. Schreiber, D. Titterington, and G. Wexler, *J. Phys. C: Solid State Phys.* **11** (1978) 699.
48. R. Liu, C. G. Olson, W. C. Tonjes, and R. F. Frindt, *Phys. Rev. Lett.* **80** (1998) 5762.
49. R. Liu, W. C. Tonjes, V. A. Greanya, C. G. Olson, and R. F. Frindt, *Phys. Rev. B* **61** (2000) 5212.
50. W. C. Tonjes, V. A. Greanya, R. Liu, C. G. Olson, and P. Molinié, *Phys. Rev. B* **63** (2001) P.
51. N. V. Smith and M. M. Traum, *Phys. Rev. B* **11** (1975) 2087.
52. Th. Straub, Th. Finteis, R. Claessen, P. Steiner, S. Hüfner, P. Blaha, C. S. Oglesby, and E. Bucher, *Phys. Rev. Lett.* **82** (1999) 4504.
53. D. E. Moncton, J. D. Axe, and F. J. Di Salvo, *Phys. Rev. Lett.* **34** (1975) 734.
54. N. J. Doran and A. M. Woolley, *J. Phys. C: Solid State Phys.* **14** (1981) 4257.
55. P. Fazekas and E. Tosatti, *Phil. Mag. B* **39** (1979) 229.
56. R. Manzke, O. Anderson, and M. Skibowski, *J. Phys. C: Solid State Phys.* **21** (1988) 2399.
57. R. Manzke, T. Buslaps, B. Pfalzgraf, M. Skibowski, and O. Anderson, *Europhys. Lett.* **8** (1989) 195.
58. B. Dardel, M. Grioni, D. Malterre, P. Weibel, Y. Baer, and F. Lévy, *Phys. Rev. B* **46** (1992) 7407.
59. B. Dardel, M. Grioni, D. Malterre, P. Weibel, Y. Baer, and F. Lévy, *Phys. Rev. B* **45** (1992) 1462.
60. B. Dardel, M. Grioni, D. Malterre, P. Weibel, Y. Baer, and F. Lévy, *Helv. Phys. Acta* **65** (1992) 486.

- 
61. Th. Pillo, J. Hayoz, H. Berger, M. Grioni, L. Schlapbach, and P. Aebi, *Phys. Rev. Lett.* **83** (1999) 3494.
  62. P. Blaha, K. Schwarz, and J. Luitz, *WIEN97*, Vienna University of Technology, Vienna (1996).
  63. M. E. Rose, *Relativistic Electron Theory*, John Wiley & Sons, New York (1961) 129.
  64. D. D. Koelling and B. Harmon, *J. Phys. C* **10** (1977) 3107.
  65. R. Z. Bachrach, M. Skibowski, and F. C. Brown, *Phys. Rev. Lett.* **37** (1976) 40.
  66. M. M. Traum, G. Margaritondo, N. V. Smith, J. E. Rowe, and F. J. Di Salvo, *Phys. Rev. B* **17** (1978) 1836.
  67. C. H. Chen, W. Fabian, F. C. Brown, K. C. Woo, B. Davies, B. DeLong, and A. H. Thompson, *Phys. Rev. B* **21** (1980) 615.
  68. G. Margaritondo, C. M. Bertoni, J. H. Weaver, F. Lévy, N. G. Stoffel, and A. D. Katnani, *Phys. Rev. B* **23** (1981) 3765.
  69. N. G. Stoffel, F. Lévy, C. M. Bertoni, and G. Margaritondo, *Solid State Commun.* **41** (1982) 53.
  70. O. Anderson, W. Drube, G. Karschnick, and M. Skibowski, *Ann. Isr. Phys. Soc.* **6** (1983) 315.
  71. O. Anderson, R. Manzke, and M. Skibowski, *Phys. Rev Lett.* **55** (1985) 2188.
  72. O. Anderson, G. Karschnick, R. Manzke, and M. Skibowski, *Solid State Commun.* **53** (1985) 339.
  73. N. G. Stoffel, S. D. Kevan, and N. V. Smith, *Phys. Rev. B* **31** (1985) 8049.
  74. Th. Pillo, J. Hayoz, H. Berger, F. Lévy, L. Schlapbach, and P. Aebi, *Phys. Rev. B* **61** (2000) 16,213.

---

75. G. H. Gweon, J. D. Denlinger, J. W. Allen, R. Claessen and C. G. Olson, *J. of Elec.*

*Spec. and Rel. Phen.* In press.

76. J. A. Wilson and A. D. Yoffe, *Adv. Phys.* **18** (1969) 193.